TISSUE-ENGINEERED MICROVESSEL MODELS OF
THE HUMAN BLOOD-BRAIN BARRIER

by

Raleigh Linville

A dissertation submitted to Johns Hopkins University in conformity with the requirements for the

degree of Doctor of Philosophy

Baltimore, Maryland

February 2021

Abstract

The vasculature in the brain is formed by brain microvascular endothelial cells (BMECs) surrounded by pericytes and astrocytic endfeet. Together these cellular components constitute the blood-brain barrier (BBB) and regulate transport into and out of the brain. BMECs possess intrinsic barrier properties to regulate transport, including enriched expression of tight junctions (TJs) which block paracellular transport, efflux pumps which limit transcellular transport, and nutrient transporter systems which increase substrate transcellular transport. In healthy individuals, these properties limit the passage of ~98% of small molecules into the brain, representing a major hurdle for brain disease treatment. However, during some brain diseases the BBB displays structural and functional alterations which can directly contribute to disease progression. In this work, tissue-engineered three-dimensional (3D) brain microvessels are developed to enable studies of the BBB during health and disease. Key advantages of 3D microvessels compared to two-dimensional assays (i.e., transwells) are established, including recapitulation of critical microenvironmental cues present within the native BBB (i.e., cylindrical geometry, cell-matrix interactions, and shear flow), physiological permeability, and high spatiotemporal resolution. Chapter 1 provides an overview of brain microvascular plasticity; this overview highlights processes that are later studied within our 3D microvessel models. Chapter 2 describes the tissue-engineering approach to form 3D microvessels by seeding induced pluripotent stem cell (iPSC)-derived BMECs into ~150 μm diameter channels patterned within type I collagen. This model is used to study: (1) brain specificity of barrier function, (2) efflux inhibition, (3) cytokine response, and (4) the influence of neurodegenerative mutations. Chapter 3 describes a study on the mechanisms of enhanced drug delivery using hyperosmotic BBB opening. The hyperosmotic agent mannitol results in dose-dependent and spatially heterogeneous increases in paracellular permeability through the formation

Abstract

of transient focal leaks; additionally, the susceptibility to opening and subsequent repair is modulated by growth factor treatment. Chapter 4 describes a bead assay and tissue-engineered microvessel model of brain angiogenesis used to study the influence of chemical and physical factors on angiogenic phenotype. Together these works show that tissue-engineered BBB microvessels can provide insight into the mechanisms of drug delivery and various brain disease states.

Advisor: Prof. Peter Searson

Readers: Prof. Peter Searson, Prof. Warren Grayson

Preface and Acknowledgments

I am thankful to my PhD advisor Prof. Peter Searson for being a continual source of support. Prof. Searson provided the perfect balance of mentorship and independence, allowing me to dive deep into interesting biological and engineering questions related to the blood-brain barrier. I would also like to thank Prof. Searson for supporting me in seeking out teaching opportunities during my PhD, and for establishing exciting collaborations with scientists at Hopkins and beyond.

I am grateful to my thesis committee members Prof. Warren Grayson, Prof. Luo Gu, and Prof. Piotr Walczak for their helpful advice and support.

I would like to thank staff members in the Department of Biomedical Engineering and the Institute for NanoBioTechnology (INBT), including Hong Lan, Ada Simari, Camille Mathis, Carla Dodd, Sky Tharp, Jon French, Gina Wadas, among many others.

I would like to thank my colleagues in the Searson Group who have played an instrumental role in motivating and supporting my research. Specifically, Jackson DeStefano, John Jamieson, Tracy Chung, Nan Zhao, Zhaobin Guo, Erin Gallagher, Luisa Russell, Max Bogorad, Moriah Katt, Zinnia Xu, Grant Kitchen, Dong-Hoon Choi, Nicole Zharadka, Christian Jorgensen, Andrew Wong, among many others.

I would like to thank collaborators including Prof. Piotr Walczak, Prof. Kalina Hristova, Prof. Myriam Heiman, Francisco Garcia, Chengyan Chu, among many others.

I have also had the privilege to work with extraordinarily talented undergraduate students including Matt Sklar, Alanna Farrell, Gabrielle Grifno, Diego Arevalo, Joanna Maressa, Renée Nerenberg, Ria Jha, Justin Zhou and Robert Ye. They have all made invaluable contributions to my research. It has been my absolute pleasure mentoring these students and I am so excited to see their future successes in academia, medicine, and industry.

I would also like to thank my previous research mentors including Dr. Leyan Xu, Dr. Ibolja Cernak, Dr. Michele Schaefer, Prof. Filip Lim, and Prof. Joe Tien. Specifically, I would like to thank Prof. Tien for being my biggest supporter and helping mature my research skills as an undergraduate student.

Finally, my family has been an amazing source of love and support. Thanks to my father Randy, who as the engineer of the family has motivated me to build "things" to answer questions. Thanks to my mother Dr. Pam Miller who devoted her career to special education, and who has motivated my passion for teaching and mentoring. Thanks to my twin brother Owen who is a continual source of inspiration. Thanks to my aunt and uncle Jana and Jim Callan, my aunt Peggy Florio, and my mother-in-law and father-in-law Judi Herman and Brad Herman. Thanks to my grandparents, most who did not live to see the completion of my PhD journey. I love and miss you all. And the largest thanks to my partner Jeff Herman who has supported me through my entire PhD journey. I am so excited to see what the future holds for us.

Table of Contents

List of Tables

List of Figures

Chapter 1. Cerebrovascular plasticity: processes that lead to changes in the architecture of brain microvessels

Max I. Bogorad,[1,2,†] Jackson G. DeStefano,[1,2,†] Raleigh M. Linville,[1,3,†] Andrew D. Wong,[1,2,4,†]

Peter C. Searson[1,2]

[1] Institute for Nanobiotechnology, Johns Hopkins University, Baltimore, MD

[2] Department of Materials Science and Engineering, Johns Hopkins University, Baltimore, MD

[3] Department of Biomedical Engineering, Johns Hopkins University, Baltimore, MD

[†] These authors contributed equally to this work

1.1. Introduction

The brain has no moving parts and yet it is one of the most energy expensive organs in the body, consuming 15 - 20 watts [2, 3]. To power the adult human brain, nutrients are supplied to the 100 billion neurons via a 600 km network of capillaries and microvessels [4]. Since the brain does not have significant capacity to store metabolic nutrients, cerebral blood flow (CBF) is generally proportional to cerebral metabolic rate [5], and the cell bodies of neurons are typically 10 - 20 μm from the nearest capillary [3]. Therefore, the cerebrovasculature is crucial to maintenance of normal brain function.

The cerebrovasculature, in addition to supplying nutrients and other essential molecules, is a key component of the blood-brain barrier (BBB) which maintains tight control of the brain microenvironment by regulating fluctuations in chemistry, transport of immune cells, and the entry of toxins and pathogens [3, 6]. Under homeostatic conditions, the turnover of brain microvascular endothelial cells (BMECs) is very low and the cerebrovascular architecture is considered to be static. However, due to the precise neurovascular coupling between energy supply and demand,

perturbations to the cerebrovasculature and the neuronal architecture are closely related. The cerebrovascular architecture displays profound plasticity during development, aging, injury, and disease (Figure 1-1).

Transient changes in neural activity can be accommodated by local dilation or contraction of arterioles and capillaries. However, sustained changes in the global brain microenvironment, for example due to sensory deprivation or hypoxia, can lead to robust remodeling of the cerebrovascular architecture. At the cellular level, changes in the cerebrovascular architecture involve changes in the rates of proliferation and loss of BMECs that are associated with addition or subtraction of capillary segments. As a result of neurovascular coupling, these changes are usually closely associated with local gain or loss of neurons and may ultimately be associated with changes in cognitive function. Although cerebrovascular plasticity is observed at all hierarchical levels, here we focus on the microvasculature (arterioles, capillaries and venules).

The time scales of these process span a wide range. For example, changes in CBF in response to increases in neural activity occur with a time constant on the order of seconds. Changes in cerebrovascular architecture due to sustained sensory deprivation or hypoxia, occur with time constants of several weeks. The cerebrovasculature displays elevated plasticity during development, while during aging plasticity declines. The time scale of changes during development and aging is on the order of months to years, where the rate often depends on mitigating factors such as exercise (in the case of aging). Injury can result in rapid damage to cerebrovascular and neuronal architecture, followed by partial or complete repair over weeks to months. In contrast, neurodegenerative disease is characterized by highly heterogenous changes that occur over months to years. Here, we review processes that lead to changes in cerebrovascular architecture.
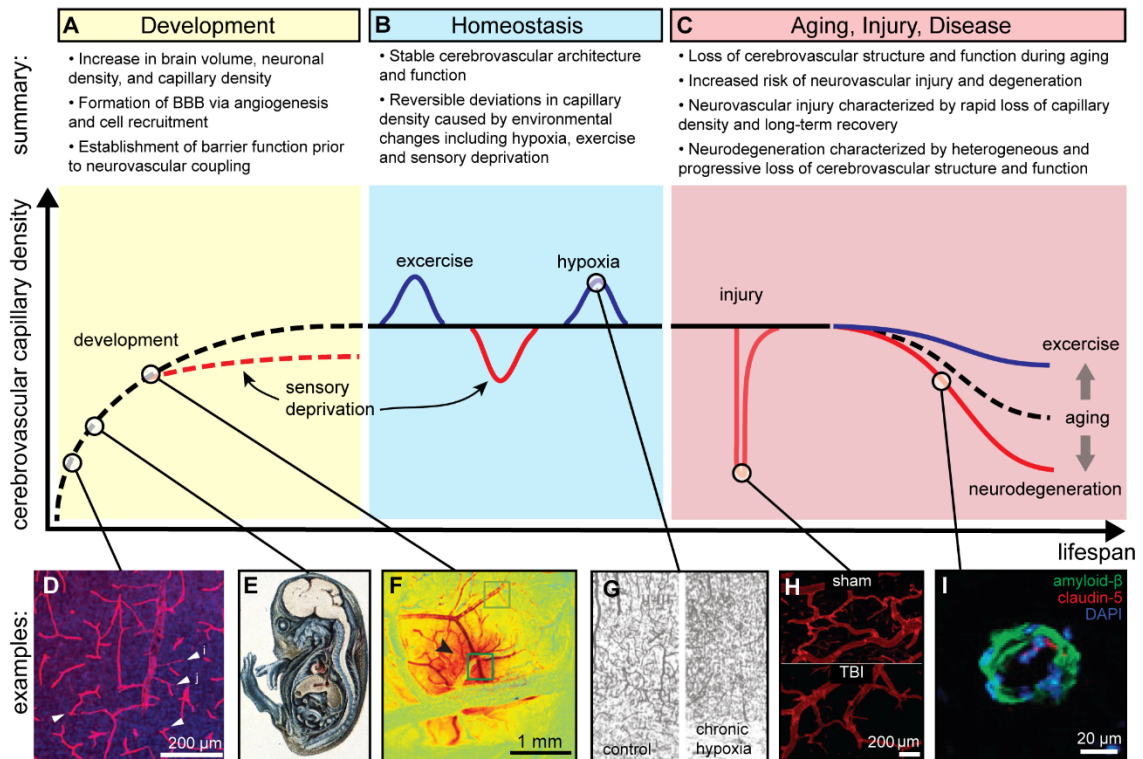
Figure 1-1. Cerebrovascular architecture displays profound plasticity during the human lifespan. A summary of changes during: (A) development, (B) homeostasis, and (C) aging, injury, and disease. (D) Microvascular density increases via angiogenesis in the brain. Shown is the mouse postnatal cortex, arrowheads denote endothelial sprouts [7]. (E) The blood-brain barrier (BBB) displays functionally low permeability during early stages of brain development; here, a guinea pig embryo injected with trypan blue demonstrates restriction of dye entry into CNS [8]. (F) Neurovascular coupling is the process by which increases in neural activity create changes in local cerebral blood flow and cerebral consumption of oxygen; here, we display a change in local total hemoglobin concentration (dark red) in response to electrical stimulation in the somatosensory cortical surface of a rat [9]. (G) Chronic hypoxia results in increased microvascular density in the mouse motor cortex [10]. (H) TBI results in a rapid decrease in microvascular density in rats [11]. (I) During Alzheimer's disease, the most common neurodegenerative disease, amyloid-beta accumulates around human microvessels and BBB integrity is compromised (downregulation of the tight junction protein claudin-5) among other cerebrovascular changes [12].

1.2. Cerebral Blood Supply and Metabolism

1.2.1. Cerebral blood supply

The brain receives blood supply from the cerebral branches of the internal carotid (which then branch into the anterior and middle cerebral arteries) and the vertebral arteries (that later merge to form the basilar artery) (Figure 1-2, A) [13]. The internal carotid arteries and the vertebral arteries

are interconnected in the cranial cavity to produce the Circle of Willis, which creates collateral circulation. If any parts of the Circle of Willis or supplying arteries become blocked or narrowed, blood flow remains at least partially preserved by the other supplying vessels, reducing the likelihood of ischemia. Anastomoses also occur between the branches of the three cerebral arteries on the surface of the brain. In adults, if one of the four arteries delivering blood to the brain is blocked, the remaining three are not usually capable of providing adequate circulation, resulting in ischemic stroke [14]. Additionally, cerebral blood supply reflects the metabolic demands of specific brain regions and defines their susceptibility to vascular damage. For example, regions that are supplied by a single major artery and have a continuous capillary network with weak collateral flow are at higher risk for hypoxic injury and stroke [15].

1.2.2. Cerebral blood flow (CBF)

The average CBF is determined by the Poiseuille equation for laminar flow:

$$CBF = \frac{\pi \Delta P r^4}{8 \mu \ell} = \frac{CPP}{CVR}$$

where ΔP is the pressure gradient per unit length of vessel (l), r is the vessel radius, and μ is the dynamic viscosity. The Poiseuille equation can be simplified in terms of the cerebral perfusion pressure ($CPP = \Delta P$) and the cerebrovascular resistance (CVR). The cerebral perfusion pressure is the difference between the mean arterial pressure (MAP) and the intracranial pressure (ICP). In adults, the ICP is normally 5 - 15 mm Hg when supine. Sustained ICP values in excess of 20 - 25 mm Hg are considered to indicate risk for focal ischemia. The average CBF is about 50 mL per 100 g of brain tissue per minute (750 mL min^{-1} for an adult) [13]. Blood flow is about twice as high in grey matter due to the higher density of neuronal cell bodies. In contrast, blood flow in white matter which is composed primarily of axons, is about twice as low [16].
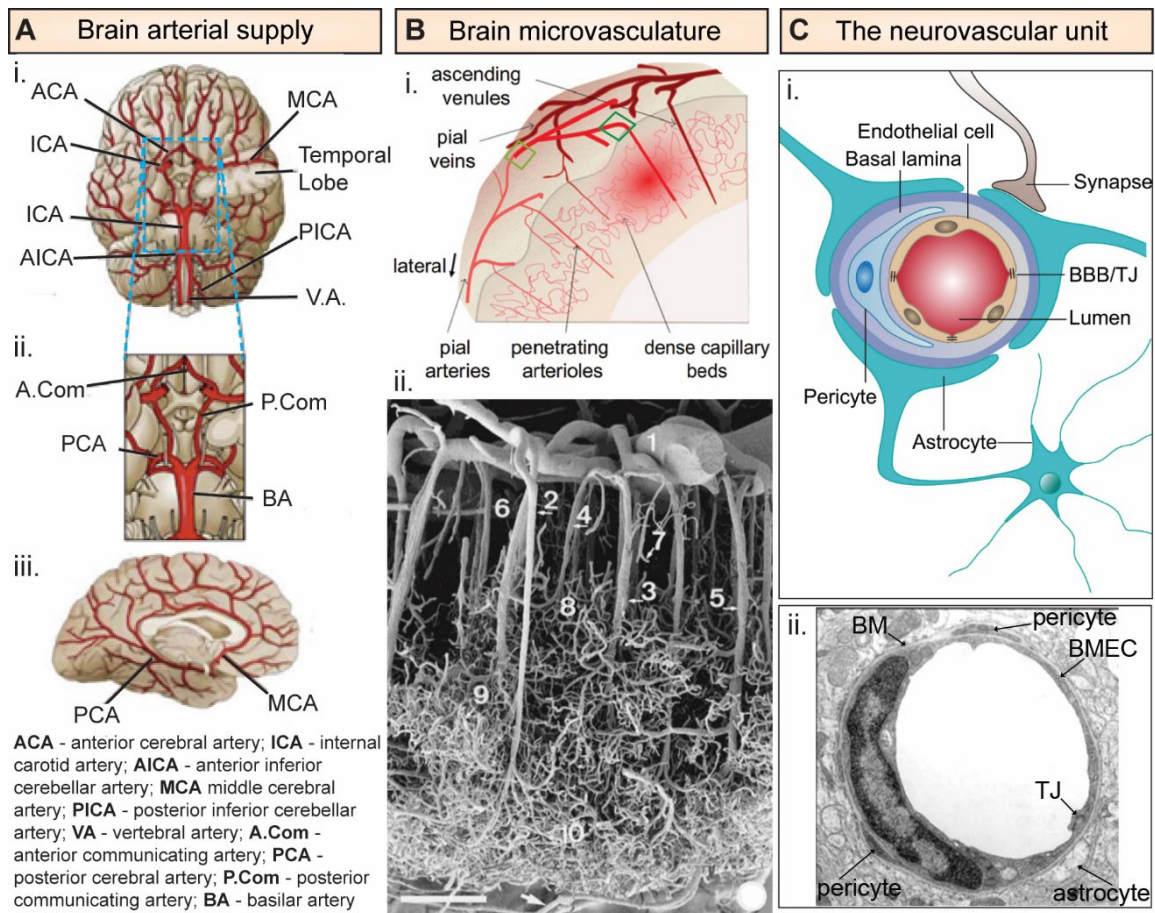
Figure 1-2. Cerebrovascular architecture. (A) Arterial architecture. (i) Inferior view of the base of the brain with cerebral arterial Circle of Willis. (ii) Magnified view of the Circle of Willis. (iii) Right lateral view of the right hemisphere. (B) Microvasculature ultrastructure in the cerebral cortex. (i) Schematic illustration of the vasculature in the cerebral cortex showing both arterial and venous systems. Pial arteries located on the surface penetrate deep into the cerebral cortex as penetrating arterioles, which branch into capillary beds that then reemerge from the cortex as ascending venules [9]. (ii) Scanning electron micrograph of a corrosion cast showing the vasculature of the temporal lobe of the human cerebral cortex [17]. (Scale bar = 375 μm) (1) Pial artery, (2) long cortical artery, (3) middle cortical artery, (4) short cortical artery, (5) cortical vein, (6) subpial zone, (7) precapillary vessel with blind ending, (8) superficial capillary zone, (9) middle capillary zone, and (10) deep capillary zone. (C) Neurovascular unit. (i) Schematic illustration of the neurovascular unit comprised of brain microvascular endothelial cells surrounded by pericytes and astrocytes [7]. (ii) Electron microscope cross section of a capillary from the rat frontoparietal cortex [18]. BM – basement membrane. BMECs – brain microvascular endothelial cells. TJ – tight junction.

CBF is maintained at a relatively constant value over a range of cerebral perfusion pressures (50 - 150 mm Hg) by autoregulation: changes in *CPP* are compensated by changes in artery diameter (vasodilation or vasoconstriction) [13, 19]. The lower limit corresponds to the point of maximum dilation and at lower pressures the CBF decreases with decreasing pressure due to vessel collapse. The upper limit corresponds to maximum constriction and higher pressures result in disruption of the BBB [16]. Autoregulation is maintained through multiple mechanisms including metabolic (e.g. CO_2 levels), myogenic (e.g. nitric oxide) and neurogenic (e.g. sympathetic innervation) regulation [19].

The average cerebral blood volume (CBV) is 3.5 - 4.5 mL per 100 g tissue (about 50 mL for an adult brain) [20]. A large fraction of this volume is contained in the venous sinuses and pial veins. Although the CBV is a small fraction of the brain vol (around 4%), it plays an important role in regulating intracranial pressure since it can be modulated very quickly by changing the blood flow. Since $CBV \propto r^2$ and $CBF \propto r^4$ (see above) it is predicted that $CBV \propto CBF^n$ where n = 0.5 [21]. Studies in humans and animals have reported exponents of 0.3 - 0.4 [21].

1.2.3. Cerebral metabolism

The brain is one of the most energy expensive organs in the human body. Overall the brain accounts for 15 - 20% of the base metabolic rate, consuming 15 - 20% of oxygen leaving the heart and 15 - 20% of the glucose consumed daily [2, 3]. Since the brain does not have significant capacity to store metabolic nutrients, fuel to power the brain is provided on-demand by the lungs and GI system which transfer oxygen and glucose, respectively, to the vascular system. Glucose is transported into the brain by glucose transporter 1 (GLUT1) localized to BMECs, while oxygen passively diffuses across endothelial cells [3].

1.3.Microvascular Architecture

1.3.1.Microvascular ultrastructure

Neuronal architecture, and thus cerebrovascular architecture, is spatially heterogeneous [13, 22]. In the cerebral cortex, pial arteries on the brain surface descend to become parenchymal arterioles to supply microvascular beds of cortical grey matter (Figure 1-2, B) [9]. At the interface between gray and white matter, the microvascular density decreases substantially along with the density of neurons and other supporting cells. In white matter, capillaries are generally arranged in parallel with axons and microvascular density is roughly 10% of that in the grey matter (consistent with the lower blood flow) [13, 22]. Pathological and physiological stresses can promote increases or decreases in microvascular density via angiogenesis or apoptosis, as addressed in subsequent sections.

In mammals, capillaries have a diameter that is slightly larger than red blood cells [23], which in humans corresponds to 8 - 10 µm in diameter. In the human brain, capillaries have branch points approximately every 30 µm, and an inter-capillary spacing of ~50 µm [17]. Venular capillaries in the mouse cortex are up to 20 branches away from penetrating arterioles [24], and the average path length of RBCs through a single capillary network in the cortex (where flow can be visualized in real time by two-photon microscopy) is 150 - 500 µm [25]. Wall shear stress in the capillaries ranges from 20 - 40 dyne cm^{-2} and is regulated by capillary tone via neurovascular coupling [26]. Downstream from capillaries, post-capillary venules (PCVs) have a perivascular space that serves as a preferential site for extravasation of leukocytes, tumor cells, and parasites [27-29]. PCVs have an average wall shear stress from 1 - 4 dyne cm^{-2}, and smaller cardiac cycle-based fluctuations compared to arterioles [26].

1.3.2. The neurovascular unit

The neurovascular unit, which comprises the blood-brain barrier (BBB), embodies the system that regulates neurovascular coupling. The cellular components of the BBB are brain microvascular endothelial cells (BMECs), pericytes, and astrocytes, and implicitly include neurons in the context of coupling (Figure 1-2, C) [6, 26]. Highly specialized BMECs provide the physical barrier between the vasculature and brain parenchyma. Pericytes are mural cells with a round nucleus and long processes that extend along the abluminal endothelial wall. A basement membrane (BM), composed of collagen IV, laminin, nidogen and heparan sulfate proteoglycans surrounds BMECs and pericytes [3]. Astrocytes are star-shaped glial cells with small cell bodies and long radial processes that contact both synapses and the BM. In capillaries, endothelial cells, pericytes, and BM are completely surrounded by astrocytic end-feet [30]. Astrocytes serve multiple functions in the brain, including spatiotemporal modulation of local blood flow by relaying signals from neurons to BMECs via their end-feet to induce dilation and contraction [30, 31].

1.4. Cerebrovascular and Neuronal Plasticity

Under homeostasis, the cerebrovascular architecture is assumed to be fixed, with very low cell turnover. Direct evidence for cerebrovascular plasticity comes from two-photon microscopy studies in animal models [32-35]. In the somatosensory and motor cortex of mice, increases in capillary length and the number of branch points have been observed up to post-natal day 25. However, in adult mice there was negligible change in capillary segment diameter, capillary segment length, or the position of branch points over about 30 days [32, 33]. These results imply that there was no turnover in BMECs during the imaging period. The subtraction or pruning of redundant capillary sections in short vascular loops occurred once every 6.25 days per mm^3 in the motor cortex [32]. Subtraction events may occur in response to disturbances in shear flow and

could contribute to pathological processes such as vascular atrophy, rarefaction, wall degeneration, and the neurodegeneration observed in aged animals [32, 36].

Increases in microvascular density occur by formation of capillaries from existing blood vessels (angiogenesis), or organization of proliferating precursor cells into new blood vessels (vasculogenesis). Angiogenesis involves endothelial cell activation, proteolytic degradation of BM and matrix, migration, alignment, proliferation, tube formation, and anastomosis with other vessels. During maturation, capillaries develop tight intracellular junctions, produce BM, and recruit pericytes and astrocytic end-feet. Arterioles recruit a layer of smooth muscle cells (SMCs), which allows control of vessel tone. Vascular endothelial growth factors (VEGF) and their respective receptor tyrosine kinases (VEGFR) are key regulators of angiogenesis and are inducible in many cell types, including astrocytes, pericytes, and endothelial cells [30]. VEGF-A also supports neurogenesis, nerve migration, axonal guidance, and neuronal survival [37]. During adulthood, brain angiogenesis is observed in response to stimuli such as hypoxia, injury, or neurodegenerative disease, as discussed in subsequent sections. Additionally, vasculogenesis can occur in response to stimuli such as trauma or tissue hypoxia as endothelial progenitor cells (EPCs) are mobilized from bone marrow to participate in endothelial cell repair/regeneration and tissue neovascularization processes [38]. For example, a higher concentration of circulating EPCs during the first week after stroke onset is associated with improved patient outcomes [39]. Cerebral arteries also display profound plasticity; for example, during hypertension (elevated blood pressure) extensive remodeling of arterial walls occurs to reduce lumen diameter [40]. In subsequent sections, we consider the cerebrovascular plasticity of microvessels (arterioles, capillaries and venules).

Neuronal plasticity is distinct from cerebrovascular plasticity in terms of location. In adulthood, neurogenesis occurs in only two regions of the brain: the subgranular zone of the dentate gyrus in

the hippocampus, and the subventricular zone [41]. These specialized regions are often referred to as neurovascular niches since the vasculature has been identified as a crucial component of the stem cell environment [42]. In the subventricular zone, neural stem cells directly contact blood vessels in homeostasis as well as regeneration [43], a feature unique to this region of the brain. It has also been shown that new neurons are born in close proximity to blood vessels in the hippocampus [44].

1.5. Factors that Influence Cerebrovascular Plasticity

1.5.1. Neural Activity

A key feature of brain metabolism is the tight coupling between energy supply and demand, commonly known as neurovascular coupling or functional hyperemia [31]. Local increases in neural activity are followed by dilation of local capillaries and upstream arterioles, increasing CBF, and increasing cerebral metabolic rate of oxygen consumption ($CMRO_2$) [9, 16]. This response is modulated by secretion of vasodilators, such as nitric oxide (NO), vasoactive intestinal polypeptide, and prostaglandin by endothelial cells, neurons, and other glial cells [31, 45]. Recently, extracellular K^+, a byproduct of neural activity, has been shown to induce a retrograde hyperpolarization signal from capillaries to arterioles, resulting in dilation [46]. These chemical factors typically act by promoting relaxation of SMCs surrounding upstream arterioles. There have been contradictory reports on the role of pericytes in dilation and contraction of capillaries [47-50]. Increased metabolism, which follows an increase in neural activity, is quantifiable though the measured increase in $CMRO_2$ [51, 52]. The response to increased neuronal activity is relatively fast with changes in CBF occurring within a few seconds [53].

Neuronal activity results in increases in CBF and $CMRO_2$, with CBF increasing 2- to 4-fold more than $CMRO_2$ [52, 54]. Local changes in oxygen consumption result in downstream changes in the concentration of deoxygenated hemoglobin, which is the basis for blood oxygenation level

dependent (BOLD) contrast functional MRI (fMRI) [55-57]. Changes in the concentration of deoxygenated hemoglobin are most prevalent in the venous tree following consumption of oxygenated hemoglobin in capillaries [58].

Cerebrovascular architecture is maintained during neurovascular coupling. However, persistent changes in neural activity or nutrient supply can lead to adaptions that include remodeling of cerebrovascular architecture. Examples of such changes are sensory deprivation and hypoxia.

1.5.2. Sensory Deprivation

Evidence for coupling between neural activity and cerebrovascular architecture comes from sensory deprivation studies in rats and studies of the effect of single eye vision depravation in cats [59-62]. Juvenile rats raised in stimulating, complex environments for 30 days were found to have increased density of capillary branch points, increased capillary surface area per unit tissue volume, and increased number of branch points per unit of capillary surface area within the striate cortex when compared to rats in non-complex environments [59, 60]. Similar studies have shown further increases in microvascular density in the cerebellar cortex of adult rats, while learning tasks increased the number of synapses per unit area [61]. Adult rats raised in complex environments showed increased microvascular density and number of branch points. New microvessels were observed after 10 days with full capillary neovascularization occurring between 30 and 60 days compared to animals housed in individual cages. Juvenile rats raised in the dark for up to 60 days showed a lower density of neurons, significantly lower cortical thickness, and lower vessel density in the striatum [63, 64].

Increases in neural activity are associated with increased growth rate in the somatosensory cortex in rat models [65]. Increased neural activity induced by whisker stimulation for one week, from post-natal day 14-21, resulted in increased microvascular density and the number of branch points in the somatosensory cortex [66]. A reduction in sensory neural activity induced by whisker

11

plucking from post-natal day zero to five resulted in decreased microvascular density and the density of branch points at post-natal day 14 [66]. These results indicate relatively fast changes in cerebrovascular architecture in juvenile mice.

1.5.3. Hypoxia

Since oxygen is essential for normal brain function, transient or sustained decreases in oxygen supply can lead to hypoxia and result in changes in the cerebrovascular architecture. In adulthood, local hypoxia is usually associated with injury or disease. For example, ischemic stroke or circulating tumor microemboli can cause local hypoxic regions downstream from occlusion. In contrast, changes in the oxygen partial pressure of the environment can lead to global hypoxia in the brain. At sea level where oxygen comprises 21% of the atmosphere, the arterial oxygen partial pressure (P_{aO2}) is 75 - 100 mm Hg. Mild hypoxia usually refers to arterial oxygen partial pressures down to 50 mm Hg, corresponding to an atmospheric oxygen concentration of about 10% or equivalent to an altitude of about 5,000 m [67]. While mild hypoxia results in numerous adaptations including angiogenesis, moderate hypoxia (P_{aO2} = 35 - 50 mm Hg) can result in cognitive deficits, and severe hypoxia (P_{aO2} < 35 mm Hg) can result in loss of consciousness.

Acute exposure to mild hypoxia results in an increase in CBV due to vasodilation and an increase (up to 2-fold) in CBF which returns to baseline after a few days [67]. The renormalization in CBF is associated with an increase in red blood cell volume and hemoglobin concentration, a well-known response to high altitude training in the field of human performance [68]. Rats subjected to chronic mild hypoxia display regional specifies increases in microvascular density; a 3-fold increase in density in the hippocampus and striatum was observed over 3 - 4 weeks while other brain regions display more modest changes [10, 69]. Increases in microvascular density are driven by angiogenesis through expression of hypoxia-inducible factor-1α (HIF-1α) and subsequent

upregulation of VEGF, while declines are achieved via BMEC apoptosis following return to normoxia [67].

1.6. Development and Aging

1.6.1. Development

During development the cerebrovasculature is dynamic in structure and function. Many signaling pathways converge to facilitate cerebrovascular plasticity [6, 7]. VEGF-A released by the developing neural tube initiates formation of the perineural vascular plexus (PNVP) via vasculogenesis. Next, BMECs invade the brain parenchyma from the PNVP via sprouting angiogenesis. Non-CNS specific signaling pathways (e.g. VEGF-A/VEGFR2) and CNS-specific signaling pathways (e.g. Wnt7a/b) guide angiogenesis as well as formation of the BBB (barriogenesis) [6, 7]. Cues in the microenvironment that guide angiogenesis and barriogenesis display unique temporal and spatial expression profiles. For example, VEGF-A expression by neurons guides early angiogenesis, whereas postnatally, astrocytes surrounding the microvasculature are the predominate source of VEGF-A; chronic developmental hypoxia disrupts this expression pattern and results in hypervascularization [70]. Wnt/β-catenin signaling is uniquely required for CNS angiogenesis and barriogenesis; neural progenitor cells release Wnt ligands (Wnt7a and Wnt7b) that guide sprouting of BMECs and induce BBB formation via expression of GLUT1[71].

The timing of angiogenesis and barriogenesis during brain development is controversial. However, accumulating physiological and molecular evidence indicates that the developing brain displays barrier properties appropriate for each developmental stage [72]. Studies in zebrafish suggest that angiogenesis and barriogenesis are temporally indistinguishable [73], while histological studies in human embryos show that during brain angiogenesis capillaries are positive for the tight junction protein claudin-5 and already restrict transport of plasma proteins [74]. Postnatally, vascular

remodeling continues but is not well understood; however, VEGF-A and axonal growth inhibitor NOGO-A have been implicated [7].

As BMECs invade the CNS they interact with neurons, neural stem cells, glial precursors, and pericytes. Sprouting BMECs release PDGF-β to recruit pericytes and initiate BBB formation during embryogenesis [75]. Astrocytes are not present in the developing brain when it is initially vascularized, however, astrocytic-derived sonic hedgehog ligands are critical in promoting BBB integrity and immune quiescence postnatally [76]. Glial-endothelial interactions also guide spatial patterning during brain development; radial glia cells provide a scaffold for BMEC migration, whereas BMECs later provide a scaffold for oligodendrocytes precursor migration [7, 77].

1.6.2. Aging

Aging is associated with heterogeneous decreases in both microvascular and neuronal density in the brain. Although these decreases can be linked, evidence suggests that cerebrovascular plasticity and neurovascular coupling are also impaired during aging [36, 78]. Histological analysis of post-mortem tissue in humans frequently shows a decrease in microvascular density (typically $10-30\%$) during normal aging, particularly in the prefrontal cortex and hippocampus [36, 78, 79]. Aging is also associated with thickening of the BM, pericyte degeneration/loss, and swelling of astrocytic end-feet [78, 80]. Age-associated functional changes include increased tight junction defects and increased permeability [81, 82]. Similar age-associated changes have been observed in brain arterioles in the cerebral cortex, including decreased density (~40%), loss of SMCs and elastin, and gain of BM and collagen [78].

Evidence from two-photon microscopy of the cerebral cortex in mouse models showed BMEC senescence, reduced turnover, and diminished hypoxia-induced angiogenesis compared to younger mice [33]. Similar to other vascular beds, impaired angiogenesis is thought to be related to HIF1-α hyporesponsiveness, growth factor downregulation, matrix metalloproteinase inhibition, eNOS

inactivity, reduced bioavailability of nitric oxide, impairment of endothelial proliferation, reduced recruitment of EPCs, and pericyte dysfunction [83]. Enriched environments or administration of VEGF viral vectors, which elicit increases in brain microvascular density in juvenile and adult rodents, result in reduced changes in aged rodent brains [84, 85]. Age-associated failure of angiogenic signaling is implicated as VEGFR-2 is not properly unregulated upon stimulation [85] and brain-region specific changes in angiogenesis-related genes are found in aged mice [79].

Numerous brain-imaging studies have shown age-associated decreases in CBF and $CMRO_2$ in many regions of the cerebral cortex, in particular, in regions vulnerable to neurodegeneration [86]. In the cortex, decreases of 0.38 to 0.76% per year have been reported [20, 86-88]. Studies of healthy brains indicate that decreases in CBF are largely distinct from grey-matter atrophy, suggesting that age-associated changes in ultrastructure and hemodynamics are independent [87]. CBF reductions may result from a loss of arterial supply to the brain (mediated by decreased IGF-1 [89]), a hypercontractile arteriole phenotype, and impaired neurovascular coupling.

Neurovascular coupling is impaired during aging in humans and animal models [90-93]. Dysfunctional neurovascular coupling causes a mismatch between supply and demand of oxygen/metabolites for neurons, likely contributing to cognitive decline. Interestingly, pharmacologically induced cerebrovascular uncoupling in mice mimics the aging phenotype (e.g. impaired spatial working memory, recognition memory, and motor coordination) without changing basal CBF [94]. The contributions of IGF-1 deficiency, oxidative stress, endothelial dysfunction, and astrocyte dysfunction to cerebrovascular uncoupling during normal aging have been reviewed elsewhere [93]. Pericyte degeneration has also been implicated in cerebrovascular uncoupling via reductions in oxygen delivery and increased metabolic stress [48]. BOLD fMRI studies of neural activity during aging are complicated by cerebrovascular changes including the loss of neurovascular coupling [95]. Contrary to other reports, a recent study utilizing a deconvolution

technique found no significant change in BOLD neurovascular coupling during visual and auditory task with normal aging [96]. Thus it remains unclear if age-associated declines in neural activity precede cerebrovascular changes or result from impaired cerebral hemodynamics.

1.7. Response to Injury and Disease

Injury and disease result in profound changes in cerebrovascular structure, plasticity, and coupling. However, the time scale of these changes are unique. Stroke and traumatic brain injury (TBI), the most common causes of cerebrovascular injury [97], result in immediate loss of cerebrovascular architecture, followed by repair responses mediated by the neurovascular unit over weeks to months. Cerebrovascular repair is coordinated by many converging processes that depend on injury type and severity [98, 99]. The signaling molecules and transcription factors that regulate these processes are often mediators of early vascular injury but may also result in long term repair and restoration of normal cerebrovascular function. During neurodegenerative disease, changes in the cerebrovasculature are more gradual and highly dynamic in that disease progression may include both increases and decreases in cerebrovascular density (Table 1-1). Injury and disease display interesting epidemiological links; for example, TBI is a risk factor for both stroke [100] and neurodegenerative disease [101]

1.7.1. Ischemic Stroke

Stroke is the most common form of cerebrovascular injury and second leading cause of death worldwide [102]. Each year, roughly 15 million individuals experience stroke worldwide. Of these, one third do not survive while another third become permanently disabled. The most common site of ischemic stroke in humans is the middle cerebral artery, which affects the posterior frontal, lateral, and parietal lobes [103]. During a typical ischemic stroke (80% of all stroke cases), the human brain ages 3.6 years for each hour without treatment; this translates to loss of about 120 million neurons and 830 billion synapses per hour [104]. Cerebrovascular plasticity is equally

dynamic; middle cerebral artery occlusion in mice results in rarefication (75% loss) of brain capillaries within the microinfarction core, while larger microvessels are unaffected [105].

The induced occlusion of a single cortical penetrating arteriole in rats results in a cylindrical microinfarction core about 500 μm in diameter and extending about 1 mm into the cortex. Neuronal activity is completely diminished within 2 hours and conditions become severely hypoxic (P_{aO2} < 10 mm Hg) in 6 hours [106]. However, occlusion of microvessels two or more branch points away from cortical penetrating arterioles (i.e. capillaries) does not lead to detectable microinfarctions, as flow in interconnected microvascular networks can reverse to compensate for the occlusion [106]. Thus, the severity of ischemic stroke is heavily dependent on the location of the occlusion and presence of collateral circulation.

The normal progression of ischemic stroke involves three phases. In the acute phase (up to 48 hours after onset), hypoxia leads to release of neurotransmitter glutamate which results in widespread excitotoxicity and subsequent neuronal injury [107]. When blood flow is restored to the infarction site either naturally or by intervention, reperfusion leads to further damage known as reperfusion injury. Activated glial cells, damaged neurons, and other cells of the neurovascular unit release growth factors [108], matrix metalloproteinases [109], reactive oxygen species [110], glutamate [111], nitric oxide [112], and cytokines [113]. These compounds are implicated in diverse roles post-injury including angiogenesis, BBB breakdown, BM degradation, glial activation, and neurotoxicity [98, 114, 115]. Additionally, peripheral immune cells enter the brain with unique temporal dynamics, which in tandem with innate glial activation, generates a proinflammatory environment [116].

The sub-acute phase of ischemic stroke, occurring between two days and six weeks, is associated with the initiation of repair. In this phase, cerebrovascular plasticity is at its highest and many of the mediators of vascular injury begin to take on neuroprotective and regenerative roles. VEGF

plays a critical role in post-ischemic neurovascular remodeling. However, the route and timing of VEGF administration following ischemic stroke modulate its therapeutic effects; for example, systemic VEGF delivery during the acute phase promotes BBB disruption and worsens brain injury, while local modulation of VEGF or systemic delivery during the sub-acute phase may reduce ischemic damage [117, 118]. Following occlusion, BMECs begin proliferating and generating sprouts within 12 - 24 hours, leading to formation of new capillaries within three days after ischemic injury [119]. Additionally, brain pericytes play various roles in promoting microvessel stabilization and neuroprotection following stroke [120]. An important characteristic of the sub-acute phase is the regenerative neurovascular niche, in which angiogenic blood vessels signal to neural progenitor cells to mediate neurogenesis. This model is supported by the presence of newly formed neurons near remodeled vessels in the rodent striatum and cerebral cortex following stroke [121], most likely due to recruitment by BMECs that form a niche for neural stem cells [42]. During the chronic phase (after approximately 3 months following stroke), endogenous plasticity declines while vascular repair, angiogenesis, and behavioral improvement continue (although at a slower rate) [122].

1.7.2. Traumatic Brain Injury (TBI)

TBI has diverse causes including blast-waves (i.e. improvised explosive devices), blunt trauma (i.e. contact sports) and penetration trauma (i.e. firearms). Cerebrovascular changes during TBI occur in two distinct phases: primary and secondary. During primary injury, direct biomechanical damage to cerebral tissue results in loss of cerebrovasculature architecture, CBF abnormalities, BBB disruption, and often fatal hemorrhaging and edema, while during secondary injury, cellular and molecular responses promote repair via angiogenesis, vasculogenesis, and neurogenesis [123, 124]. The timescale and severity of responses in these phases is dependent on the injury modality, severity, and location, among other factors.

Traumatic brain injury results in rapid and significant decreases in microvascular density [11, 125]. In an animal model of fluid percussion trauma, the cerebrovascular density of the ipsilateral cerebral hemisphere decreased by approximately 50% within 24 hours, while recovery was dependent on the severity of the injury and associated with establishment of a proangiogenic environment [125]. Other ultrastructural changes following TBI include BMEC swelling, vessel thinning, BM thickening, and pericyte degeneration [99]. In TBI patients, reduced CBF is observed within 12 hours after injury, while neurovascular uncoupling is thought to occur during the secondary phase [126]. Additionally, BBB disruption is widely observed following TBI and is associated with worse long-term outcomes, and may persist for years after injury contributing to risk of neurodegenerative disease [127, 128]. Angiogenesis and vasculogenesis are initiated during the secondary injury phase, resulting in increases in microvascular density over several weeks [99, 125, 129]. Local hypoxia is thought to be the driver of neovascularization with HIF-1α and VEGF acting as critical molecular regulators [129].

1.7.3. Neurodegeneration

Cerebrovascular structure, plasticity, and coupling are altered during neurodegenerative disease, beyond the impairments observed during normal aging [130, 131]. Whether cerebrovascular changes precede, follow, or occur concurrently with neurodegeneration is not yet fully understood, however, accumulating evidence suggests that cerebrovascular changes can occur prior to the presentation of symptoms and promote neurodegeneration [132-141].

Neurodegenerative disease is characterized by progressive loss of functional neurons and compromised human brain function. Age is the greatest risk factor for neurodegenerative disease [142]. Neurodegeneration and normal brain aging share common pathologic origins including oxidative stress, mitochondrial dysfunction, and proteotoxicity [142, 143]. However, neurodegenerative diseases are also highly heterogeneous with distinct risk factors (environmental

and genetic), histopathological hallmarks (neuronal loss in specific brain regions and formation of protein aggregates), and clinical manifestations. Despite the pathogenic differences, several themes connect cerebrovascular changes during neurodegeneration: (1) BBB dysfunction [6, 80, 130], (2) cerebral hypoperfusion and glucose hypometabolism [144], and (3) overexpression (AD, PD, HD) or underexpression (ALS) of VEGF (Table 1-1) [37].

1.7.3.1. Alzheimer's disease (AD)

Cerebrovascular changes associated with Alzheimer's disease include vascular degeneration, altered angiogenesis, reduced CBF, increased BBB permeability, and neurovascular uncoupling [130, 133]. The amyloid hypothesis states that the formation of amyloid-β (predominantly the Aβ-42 isoform) within the brain parenchyma induces gain of toxic function and neurodegeneration. However, AD is also closely associated with cerebral amyloid angiopathy (CAA) which is characterized by perivascular accumulation of predominantly the Aβ-40 isoform in the BM of leptomeningeal and cortical vessels of the cerebrum and cerebellum [145]. The epidemiological link between cerebrovascular risk factors and AD pathogenesis is well established and has been reviewed elsewhere [146].

Postmortem analysis of AD brain reveals capillary loss, as well as atrophied BMECs and pericytes, swollen astrocytic end-feet, hypercontractile SMCs, BM thickening, and BM deposits [18, 147]. In severe CAA, additional pathologies include SMC loss, duplicated lumens, fibrinoid necrosis, and hyaline degeneration [145]. Despite capillary loss, AD is associated with increased concentrations of VEGF [148, 149]. In post-mortem human AD tissue, an increase in the number of angiogenic vessels (integrin αvβ3 expression) was correlated with several AD pathologies including neurofibrillary tangles and Aβ load [150]. Transgenic AD animal models corroborate these findings; in aged Tg2576 mice, disruption of tight junctions was linked to increased microvascular density, suggesting that amyloid-β initiates hypervascularization and BBB

disruption in early-stage AD, while microvascular degeneration occurs in last-stage AD [151]. However, the effects of amyloid-β on brain angiogenesis remain convoluted as amyloid-β has been reported to both promote and suppress angiogenesis both *in vitro* and *in vivo* [152, 153].

Reduced CBF, increased BBB permeability, and reduced glucose metabolism are found to precede AD neurodegeneration in animal models and human studies.[50] Reduced CBF is found in patients at high risk of developing AD (APOE ε4 allele) and patients with mild cognitive impairment [154, 155]. These reductions persist during AD progression and appear to correlate with the degree of cognitive decline and AD pathology [18]. Recently, neutrophil adhesion in brain capillaries has been shown to reduce cortical blood flow in AD mouse models [156]. Additionally, BBB permeability increases before plaque formation in an AD mouse model, while MRI studies indicate that increased BBB permeability of mild cognitive impairment patients correlates with AD cognitive decline [132, 134]. PET imaging studies find reduced glucose metabolism in patients at high risk of AD, which precedes brain atrophy [130, 157]. CBF, metabolic rate, and BBB permeability changes contribute to ischemic/hypoxic damage of the neurovascular unit and initiate and/or exacerbate AD pathology [50, 130].

AD patients, APOE ε4 allele carriers, and transgenic AD mice exhibit impaired neurovascular coupling responses, while therapies that rescue neurovascular coupling are associated with cognitive improvements [93, 135, 158]. AD-associated changes in vascular reactivity factors (i.e. eNOS and endothelin-1) may underlie neurovascular uncoupling and chronic hypoperfusion [159]. Interestingly, partial eNOS deficiency in mice results in CAA-like pathologies and stroke in brain regions associated with hypoperfusion in preclinical AD patients [160].

1.7.3.2.Parkinson's disease (PD)

Cerebrovascular changes associated with Parkinson's disease include both vascular degeneration and angiogenesis. PD is histopathologically characterized by dopaminergic neuronal loss within

the substantia nigra in the brainstem [161]. Additionally, Lewy bodies, aggregates of predominately α-synuclein, form in the cytoplasm of specific neurons in widespread brain regions. Impairment of α-synuclein degradation during aging may contribute to dopaminergic neuronal loss and downstream motor deficient (bradykinesia) observed in PD patients [143].

PD-associated vascular degeneration resembles that of AD; morphological changes include BMEC degeneration and decreases in microvascular density [147, 162]. However, other studies find increased angiogenic vessels (integrin αvβ3 expression) in PD-associated brain regions, without overt changes in microvascular density [163]. Thus, it is possible that a proangiogenic environment is established in PD patients, as evidenced by heighted angiogenic biomarkers [164]. Integrin αvβ3 expression is co-localized with BBB leakage in animal models of PD (6-hydroxydopamine mouse model) while the striatum in postmortem PD sections demonstrates signs of BBB disruption, suggesting that angiogenesis disrupts the BBB, thereby contributing to vascular degradation in late-stage disease [165, 166]. Additionally, hypoperfusion of specific brain regions of PD patients is correlated with motor dysfunction [167].

Elevated microvascular plasticity in PD patients treated with deep brain stimulation (DBS) has recently been reported [168]. Reductions in microvascular density, endothelial tight junction protein expression, and endothelial VEGF expression were found in PD patients compared to age-matched controls. However, in PD patients treated with subthalamic nucleus DBS, these cerebrovascular changes were reversed. Increased neural activity promoted by DBS rapidly modulates production of neurotrophic and angiogenic factor such as VEGF and BDNF [169].

1.7.3.3. Huntington's disease (HD)

Huntington's disease is associated with cerebrovascular alterations including increased microvascular density, BBB disruption, and altered cerebral hemodynamics. HD is caused by expansion of cytosine–adenine–guanine (CAG) repeats in the huntingtin gene [170]. Mutant

Table 1-1. Changes in cerebrovascular structure, plasticity, and coupling occur in AD, PD, HD, and ALS.

Neurodegenerative disease	Neuropathological hallmarks	Microvascular ultrastructure	Angiogenesis	Hemodynamics	NVU dysfunction
Alzheimer's disease (AD)	Extracellular amyloid-β plaques, intracellular tau tangles, loss of synapses and neurons (predominately cerebral cortex)	Cerebral amyloid angiopathy [145] vascular degeneration [18, 147] ↓ microvascular density [36]	↑ angiogenic vessels [150, 151] ↑ VEGF [148, 149]	↓ CBF [154] Neurovascular and neurometabolic uncoupling [93] [157]	↑ BBB permeability [132, 134, 151]
Parkinson's disease (PD)	Intracellular ∝-synuclein aggregates and loss of dopaminergic neurons (substantia nigra, other regions)	vascular degeneration, ↓ microvascular density [147, 162]	↑ angiogenic vessels and biomarkers [163, 164]	↓ CBF [167]	↑ BBB permeability [165, 166]
Huntington's disease (HD)	Intracellular mutant huntingtin (mHTT) aggregates and loss of neurons (striatum, cortex, hippocampus, others)	↑ microvascular density [171, 172]	↑ angiogenic potential of HD hiPSC-derived BMECs [137] ↑ astrocytic VEGF [173]	↓ CBF [138] Neurovascular and neurometabolic uncoupling [139, 173]	BBB dysfunction of HD hiPSC-derived BMECs [137] ↑ BBB permeability [136, 171]
Amyotrophic Lateral Sclerosis (ALS)	SOD-1 or TDP-43 aggregates and loss of motor neurons (cortex, brainstem, spinal cord)	vascular degeneration [174]	↓ VEGF [175, 176]	↓ CBF [177]	↑ BBB permeability [140, 174]

For each disease neuropathological hallmarks as well as cerebrovascular changes are summarized. Across the four most common NDs there are reported reductions in cerebral blood flow (CBF) and increases in blood-brain barrier (BBB) permeability. Overexpression (AD, PD, HD) or underexpression (ALS) of vascular endothelial growth factor which drives brain angiogenesis may underlie ultrastructural changes. While vascular degeneration is widely reported in AD and PD (characterized by decreased microvessel density), elevated microvessel density may occur in early-stage disease and contribute to BBB permeability increases also associated with these diseases. Note: changes are brain region specific.

huntingtin (mHTT) protein, produced by neurons and astrocytes, aggregates within the brain parenchyma, BM of microvessels, and cells of the NVU [171]. Loss-of-function of normal HTT and gain-of-function of mHTT contributes to progressive loss of neurons in the striatum, cortex, and hippocampus, among other regions, accompanied by declines in cognitive and motor functions [170].

In HD patients and mouse models of HD, microvascular density is increased up to two-fold compared to age-matched healthy controls [171, 172]. BBB disruption has been observed in HD mouse models, brain imaging of mild-to-late stage HD patients, and postmortem studies of HD tissue [171]. Changes in tight junction expression that underlie increased BBB permeability were recently found to precede disease presentation in a mouse model (R6/2) [136].

Astrocytes have been implicated as a mediator of microvascular changes; increased astrocytic VEGF in a HD mouse model (R6/2) promoted angiogenesis and loss of pericytes contributing to abnormal cerebral autoregulation [173]. Recent work suggests that BMECs of HD patients are autonomously dysfunctional; human induced pluripotent stem cells (hiPSCs) derived into BMECs from HD patients exhibit elevated angiogenic potential and deficient BBB properties compared to healthy cell lines [137]. Additionally, reductions in cortical CBF and impaired neurometabolic coupling have been reported in early stage HD patients and the R6/2 mouse model, respectively [138, 139].

1.7.3.4. Amyotrophic Lateral Sclerosis (ALS)

During amyotrophic lateral sclerosis, progressive degeneration of motor neurons in the cortex, brainstem, and spinal cord lead to loss of voluntary muscle control and generalized paralysis. Many molecular mechanisms have been implicated in ALS pathogenesis, including failure of proteostatis, mutations of RNA-binding proteins, axonal transport dysfunction, cytoskeletal disarrangement, and dysfunction of glial and neurovascular cell types [178, 179]. ALS-associated neurovascular unit

dysfunction, including BBB breakdown, has been reviewed elsewhere [174]. In SOD1 mutant mouse models, disruption of the blood-spinal cord barrier was observed prior to the development of symptoms of the disease and prior to an inflammatory response [140], suggesting that vascular changes can precede symptomatic disease.

Genetic alterations in expression of hypoxia-inducible genes are heavily implicated in ALS pathogenesis. Mice with reduced VEGF levels develop progressive motor neuron degeneration resembling human ALS, and reduced VEGF accelerates motor neuron degeneration in familial ALS mouse models [175, 176]. Humans with genetic variations of the VEGF promoter that confer low levels of circulating VEGF are at heightened risk to develop ALS [176]. Interestingly, early ALS patients demonstrated reduced CSF VEGF levels independent of VEGF promoter polymorphisms [141]. Insufficient VEGF likely contributes to ALS progression by both depriving neurons of neurotrophic signals and by contributing to BBB dysfunction and hypoperfusion/ischemia [37].

1.8.Summary

During normal brain function, local changes in neural activity are accompanied by local dilation/contraction of microvessels to meet current metabolic demands. Under these conditions the cerebrovascular architecture is generally thought to be fixed and, at the cellular level, the turnover of BMECs is negligible. However, subtraction and pruning of redundant loops suggest that the cerebrovasculature is not completely static during homeostasis. During development, neuronal and glial interactions drive additive changes in the cerebrovasculature, while the loss of neurons associated with aging is accompanied by heterogeneous subtractive changes. Injury and disease can also result in subtractive loss and induce subsequent repair processes. Sustained changes in the global brain microenvironment due to sensory deprivation or hypoxia, can also lead to vascular remodeling and additive or subtractive changes in the cerebrovascular architecture. A

common factor in all additive changes in the cerebrovasculature is VEGF, a protein involved in vasculogenesis and angiogenesis, and expressed and recognized by BMECs, glial cells, and neurons Model systems to study cerebrovascular plasticity are continually advancing. Multiphoton and intravital microscopy support studies of cerebrovascular plasticity in living animal models.[32-35] In humans, neuroimaging modalities (i.e. fMRI) provide real-time metrics of cerebrovascular function, while postmortem histological analyses provide information on cerebrovascular structure. There remains a need for techniques to study human cerebrovascular plasticity with high temporal and spatial resolution. *In vitro* models of cerebrovascular plasticity may satisfy this need. However, current models fail to recapitulate *in vivo* structure, function or plasticity. For example, while transwell assays (comprised of BMECs cultured on a permeable membrane) can achieve physiological permeability, it does not mimic physiological hierarchy or geometry [26]. Without three-dimensional structure, models of cerebrovascular plasticity will fail as they cannot recapitulate additive or subtractive changes of capillaries. Recent advances in stem cell technology, microfluidics, and tissue engineering have led to three-dimensional cerebrovascular models with increasing complexity [180, 181]. However, their ability to achieve characteristic stability of cerebrovascular architecture during homeostasis and plasticity during perturbation has yet to be shown. Development of stable three-dimensional models of the cerebrovasculature will support studies of brain plasticity, as animal models do not always accurately model human homeostasis or pathogenesis.

Chapter 2. Human iPSC-derived blood-brain barrier microvessels: validation of barrier function and endothelial cell behavior

A version of this chapter is published in Biomaterials 190 (2019) 24-37. [181]

Raleigh M. Linville,[1,2] Jackson G. DeStefano,[1,3] Matt B. Sklar,[1] Zinnia Xu,[1,2] Alanna M. Farrell,[1,2]

Max I. Bogorad,[1,3] Chengyan Chu,[4] Piotr Walczak,[4] Linzhao Cheng,[5] Vasiliki Mahairaki,[5,6]

Katharine A. Whartenby,[6] Peter A. Calabresi,[6] Peter C. Searson[1,3]

[1] Institute for Nanobiotechnology, Johns Hopkins University, Baltimore, MD

[2] Department of Biomedical Engineering, Johns Hopkins University School of Medicine, Baltimore, MD

[3] Department of Materials Science and Engineering, Johns Hopkins University, Baltimore, MD

[4] Department of Radiology and Radiological Science, Johns Hopkins University School of Medicine, Baltimore, MD

[5] Institute for Cell Engineering, Johns Hopkins University School of Medicine, Baltimore, MD

[6] Department of Neurology, Johns Hopkins University School of Medicine, Baltimore, MD

2.1. Introduction

The blood-brain barrier (BBB) maintains tight control of the brain microenvironment by regulating fluctuations in chemistry, transport of immune cells, and entry of pathogens and toxins [182-184]. The brain microvascular endothelial cells (BMECs) that form the lumen of the cerebrovasculature are highly specialized, expressing tight junctions which effectively block paracellular transport, and an array of transporters and efflux pumps which regulate transcellular transport. Additionally, BMECs display low turnover and motility to maintain a quiescent state in the healthy cerebrovasculature. Differences in the cerebrovasculature between humans and rodents mean that animal models do not always recapitulate human disease [185]. Therefore, *in vitro* models can provide an important link between human physiology and animal models, and have the potential to

contribute to elucidating disease mechanisms and developing new strategies for drug and gene delivery to the brain. However, for widespread adoption, these *in vitro* models must achieve physiological barrier function and endothelial cell behavior.

Advances in tissue engineering have led to the development of a new generation of perfusable three-dimensional (3D) models of the BBB [186-189]. However, recapitulating physiological tight junction formation and barrier function has been particularly challenging, largely due to the fact that primary and immortalized human and animal brain microvascular endothelial cells exhibit transendothelial electrical resistance (TEER) values well below the range thought to be physiological $(1,500 - 8,000 \ \Omega \ cm^2)$ [190-193]. To overcome this limitation, many existing BBB models incorporate supporting cell types of the neurovascular unit (i.e. astrocytes and pericytes) which improve barrier function, but still do not achieve physiological TEER or permeability. Brain microvascular endothelial cells differentiated from human induced pluripotent stem cells (dhBMECs) display many of the hallmarks of the BBB in two-dimensional (2D) transwell assays including physiological TEER, permeability and efflux behavior [194-197]. Interestingly, BBB phenotype is achieved without supporting cell types. In previous work we have reported on the role of matrix composition and stiffness on the adhesion and barrier formation of dhBMECs relevant to tissue engineering of 3D microvessel models [198].

Here, we report on characterization of an *in vitro* model of a brain post-capillary venule (PCV). PCVs are characterized by diameters of around 100 μm, a relatively thick basement membrane, a perivascular space with limited supporting cells, and a wall shear stress of $1 - 4$ dyne cm^{-2} [199-202]. PCVs are the site for immune surveillance and preferential extravasation of leukocytes, tumor cells, parasites and viruses [28, 203-208]. We report on the structure (i.e. endothelial cell behavior) and function (i.e. permeability) of the human iPSC-derived PCV model, in comparison to non-brain-specific microvessels constructed using human umbilical vein endothelial cells

(HUVECs). We show that the dhBMEC microvessels recapitulate key aspects of the human BBB including physiologically low solute permeability, cell turnover, and cell motility. Compared to self-organizing approaches recently developed for BBB modeling, which mimic angiogenesis and vasculogenesis, our microvessels are functional after only two days of culture and without the complexities of co-culture with astrocytes or pericytes [180, 209]. In addition, endothelial cells are all in contact with extracellular matrix and hence the microvessel lumen is able to constrict or dilate in response to transmural pressure or other perturbations. We provide proof-of-principle examples of how a physiological brain PCV model can be used to study biologically- and clinically-relevant processes, including patient-specific models of neurodegenerative disease, efflux inhibition, hyperosmolar opening of the BBB, and activation by inflammatory cytokines.

2.2. Materials and Methods

2.2.1. Cell culture

Human brain microvascular endothelial cells (dhBMECs) were differentiated from induced pluripotent stem cells (iPSCs) as previously reported [196]. Briefly, iPSCs were singularized using StemPro accutase (Thermo Fisher) and seeded at 15,000 cells cm^{-2} on Matrigel-treated six-well plates (Corning). Cell lines used: BC1 and iPS12 [210], KW01, and AD6 [211]. The BC1 and iPS12 lines were derived from healthy individuals. The AD6 line was derived from skin fibroblasts (Coriell Institute) of a 56-year-old male with Alzheimer's disease harboring the familial AD PSEN1 mutation A246E [211]. The KW01 line was derived from a 73-year-old male with multiple sclerosis. All iPSC lines were used between passage 30 - 70. Cells were cultured in TeSR-E8 media (Stem Cell Technologies) for three days to approximately 40% confluence, with 10 μM ROCK inhibitor Y27632 (ATCC) supplemented for the first 24 hours. The differentiation was then initiated in unconditioned media without bFGF (UM/F-): DMEM/F12 (Life Technologies) supplemented with 20% knockout serum replacement (Life Technologies), 1% non-essential amino

acids (Life Technologies), 0.5% GlutaMAX (Life Technologies) and 0.836 μM beta-mercaptoethanol (Life Technologies). After six days of UM/F- culture, cells were cultured for two days in BBB induction media: human endothelial cell serum-free media (Life Technologies) supplemented with 1% human platelet poor derived serum (Sigma), 2 ng mL^{-1} bFGF (R&D Systems), and 10 μM all-trans retinoic acid (Sigma). Media was changed every 24 hours. After a total of 11 days in culture, cells were detached using accutase and sub-cultured onto plates coated overnight with 50 μg mL^{-1} human placental collagen IV (Sigma) and 25 μg mL^{-1} fibronectin from human plasma (Sigma). Sub-cultures were conducted at a 1:1 surface area ratio (one well of differentiated cells sub-cultured onto one well of six-well plate) and in BBB induction media supplemented with 10 μM ROCK inhibitor Y27632. After one hour, cell monolayers were washed three times with phosphate buffered saline (PBS; Thermo Fisher), detached with accutase, and seeded into microvessels once resuspended in BBB induction media supplemented with 10 μM ROCK inhibitor Y27632 to 50 million cells mL^{-1}.

Human umbilical vein endothelial cells (HUVECs) were used up to passage six. HUVECs were grown in MCDB 131 (Caisson) supplemented with 10% fetal bovine serum (Sigma), 1% pen-strep-glut (Thermo Fisher), 1 μg mL^{-1} hydrocortisone (Sigma), 10 μg mL^{-1} heparin (Sigma), 25 μg mL^{-1} endothelial cell growth supplement (Thermo Fisher), 0.2 mM ascorbic acid 2-phosphate (Sigma), and 80 μM dibutyryl cyclic-adenosine monophosphate (db-cAMP; Sigma). TrypLE Express (Life Technologies) was used to detach cells for routine passing and seeding of microvessels. HUVECs were resuspended to 10 million cells mL^{-1} in media for seeding microvessels.

2.2.2. Microvessel fabrication, perfusion, and maintenance

To fabricate microvessels, 1 cm (length) x 1.75 mm (width) x 1 mm (height) channels were patterned in Sylgard 184 polydimethylsiloxane (PDMS; Dow Corning) using an aluminum mold (Figure 2-1). The PDMS was then plasma-treated, adhered to glass slides, and treated with

trimethoxysilane (Sigma) to reduce formation of bubbles at the PDMS-collagen interface. Neutralized 7 mg mL^{-1} rat tail type I collagen (Corning) was gelled around a 150 μm diameter super-elastic nitinol wire (Malin Co.) for 30 minutes at 37°C. To prevent delamination of the gel, 2% agarose was added to both sides of the collagen gel. Following removal of the template wires, the bare channels were cross-linked with 20 mM genipin (Wako Biosciences) for two hours. Residual genipin was removed by perfusing channels under high flow (~0.5 mL h^{-1}) with PBS for at least 12 hours. Lastly, channels were coated overnight with 50 μg mL^{-1} collagen IV and 25 μg mL^{-1} fibronectin in either HUVEC or dhBMEC microvessel media (composition outlined below). Derived hBMEC microvessels were seeded and perfused using brain microvessel media: endothelial cell serum-free media (Life Technologies) supplemented with 1% human platelet poor derived serum (Sigma), 1% penicillin-streptomycin (Life Technologies), 400 μM db-cAMP, 20 μM phosphodiesterase inhibitor Ro-20-1724 (Calbiochem), and 3% 70-kDa dextran (Sigma). Both retinoic acid and bFGF (present during the last two days of the differentiation) were removed from the microvessel media. Additionally, 10 μM ROCK inhibitor Y27632 was supplemented during the first 24 hours of microvessel perfusion to increase adhesion [198, 212].

HUVEC microvessels were seeded and perfused using HUVEC microvessel media: HUVEC cell culture media supplemented with 400 μM db-cAMP, 20 μM Ro-20-1724, and 3% 70-kDa dextran. These additions have previously been shown to promote barrier function and long-term stability of *in vitro* microvessels [213-215]. Confluent HUVEC microvessels do not form using brain microvessel media (data not shown).

Microvessel shear stress was estimated by Poiseuille's equation: $\tau = \mu Q / 2\pi d^3$ where μ is the fluid dynamic viscosity (~1.4 cP for media supplemented with 3% dextran), Q is the volumetric flow rate, and d is the microvessel diameter. The volumetric flow rate was measured daily as the increase in fluid volume in the lower media reservoir. A physiological shear stress of ~4 dyn cm^{-2} was

maintained with a reservoir height difference (Δh) of 5 cm, corresponding to a volumetric flow rate of ~ 0.5 mL h^{-1}.
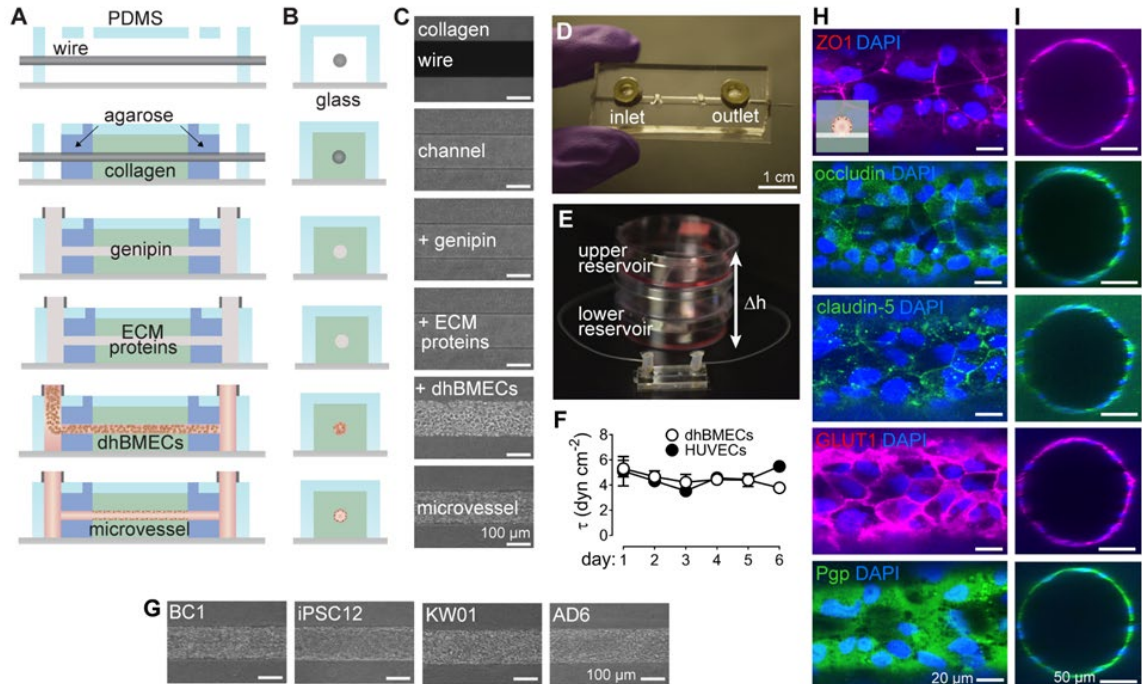
Figure 2-1. Fabrication, perfusion, and maintenance of human iPSC-derived blood-brain barrier microvessels. (A,B) Schematic illustrations of the side- and end-view of 150 μm diameter microvessel fabrication. (C) Phase contrast images of sequential microvessel fabrication steps. (D) PDMS-based microfluidic chip. (E) Perfusion system comprised of tubing connecting inlet and outlet ports to an upper and lower media reservoir (Δh = 5 cm). (F) Shear stress for BC1 dhBMEC and HUVEC microvessels over six days. (G) Phase contrast images of brain-specific microvessels constructed from various iPSC lines including BC1, iPS12, KW01, and AD6 on day two after seeding. (H,I) Fluorescence images of blood-brain barrier (BBB) markers in BC1 dhBMEC microvessels on day 2: zona occluden-1 (ZO1), occludin, claudin-5, glucose transporter-1 (GLUT1), and P-glycoprotein (P-gp). Images shown are a 0.4 μm confocal z-slice of the bottom microvessel pole, or a cross-section of the microvessel. Nuclei visualized with DAPI (blue).

2.2.3. Live-cell imaging

The strategy for live-cell imaging of dhBMEC and HUVEC microvessels is summarized in Figure 2-2. Microvessels were imaged using an inverted microscope (Nikon Eclipse Ti-E) maintained at 37° C and 5% CO_2. Epifluorescence illumination was provided by an X-Cite 120LEDBoost

(Excelitas Technologies). A 10x objective (Nikon) was used for all epifluorescence and phase-contrast images. Imaging of microvessels was conducted on days two, four and six after seeding. Permeability was simultaneously measured for three different molecular weight solutes introduced into the upper media reservoir at a final concentration of 200 µM Lucifer yellow (CH dilithium salt; LY) (Sigma), 5 µM Rhodamine 123 (R123) (Thermo Fisher), and 2 µM Alexa Flour-647-conjugated 10 kDa dextran (Thermo Fisher). A NIS Elements (Nikon) imaging protocol was initiated to acquire both phase contrast and fluorescence images every two minutes for two hours (61 total frames). At every time point six images were collected: (1) a phase contrast image of the top of the microvessel (located and maintained by autofocus), (2-5) phase contrast and fluorescence images of the microvessel midplane, and (6) a phase contrast image of the bottom of the microvessel. To independently excite and collect the emission from each fluorophore, three filter cubes were used: Chroma 39008 for Lucifer yellow (20 ms exposure), Chroma 49003 for Rhodamine 123 (50 ms exposure), and Chroma 41008 for Alexa Fluor-647-conjugated dextran (200 ms exposure). The total image area was 8.18 mm x 0.67 mm, corresponding to ten adjacent frames using a 10x objective.

2.2.4. Permeability

Large images were cropped to an area of 1 mm x 0.67 mm (corresponding to a single 10x magnification frame); a central region of the large image was chosen to minimize contributions of interstitial flow of solutes from the inlet and outlet. Intensity profiles were obtained using ImageJ (NIH). The apparent permeability (cm s^{-1}) is calculated as $P = (d/4)(1/\Delta I)(dI/dt)$, where d is the vessel diameter, ΔI is the initial increase in fluorescence intensity upon luminal filling, and $(dI/dt)_0$ is the rate of increase in fluorescence intensity as solute exits into the gel [216, 217]. Over the course of two hour imaging experiments there are four phases: (i) before the solute reaches the microvessel lumen, (ii) while the solute is filling the microvessel lumen (typically 20-30 minutes),
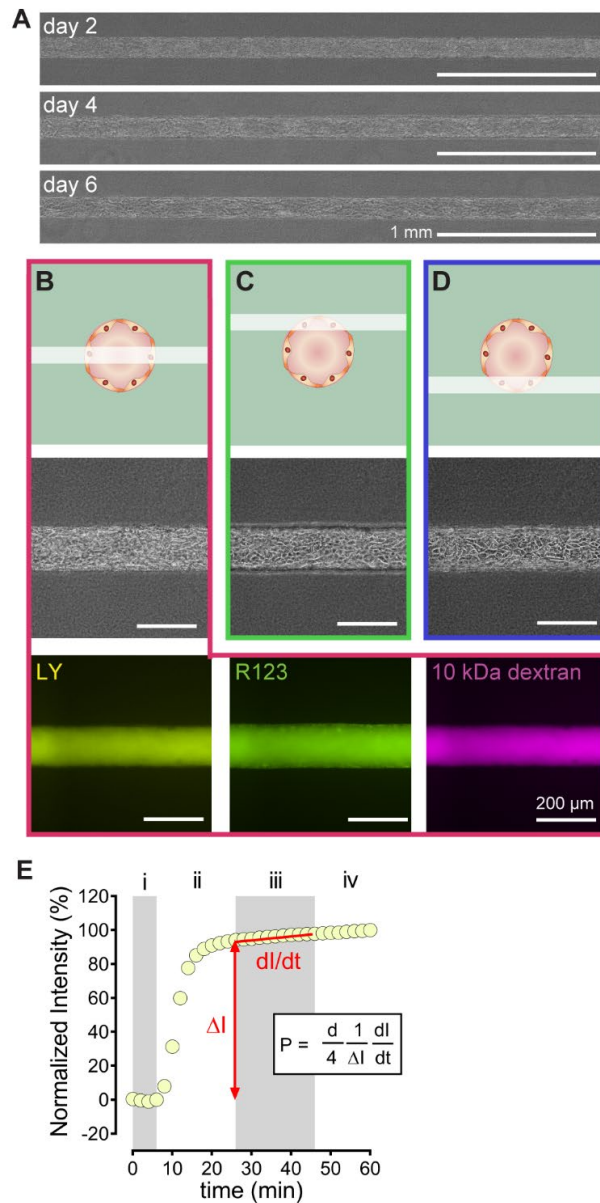
Figure 2-2. Live-cell imaging of human iPSC-derived blood-brain barrier microvessels.(A) representative phase contrast images of a BC1-derived brain microvessel on days two, four and six under a wall shear stress of about 4 dyne cm^{-2}. (B) Phase contrast and fluorescence images of perfusion with Lucifer yellow, Rhodamine 123, and 10 kDa dextran at the microvessel midplane. (C,D) Phase contrast images at the top and bottom planes, respectively. (E) Representative fluorescence intensity for Lucifer yellow for a region of interest comprising both the microvessel and surrounding matrix: (i) Prior to perfusion of the dye. (ii) luminal filling where ΔI represents the increase in fluorescence intensity. (iii) Penetration of the dye into the surrounding matrix results in a linear increase in fluorescence intensity (dI/dt).

(iii) while the solute permeates into the ECM, and (iv) when solute continues to permeate into ECM and where interstitial flow of solutes interferes with quantification. After luminal filling, the intensity increase (dI/dt) was calculated over twenty minutes. For Rhodamine 123, to eliminate the contributions of intracellular accumulation, the permeability was also calculated by considering only the rate of increase in fluorescence intensity in the ECM; unless otherwise noted this value is reported for Rhodamine 123 permeability [218]. The detection limit for permeability of Alexa Flour-647-conjugated 10 kDa dextran ($\leq 1 \times 10^{-7}$ cm s^{-1}) was limited by photobleaching of the genipin cross-linked collagen gel. Some brain microvessels displayed macroscopic breakdown past day four of perfusion (~30% of devices); these microvessels were not considered in time course permeability analysis. Monolayer breakdown is not observed on transwells on this timescale, suggesting that cell-ECM interactions may contribute to model instability.

For studies of efflux inhibition, 2 μM tariquidar (Sigma) was supplemented in brain microvessel media at 36 hours after cell seeding. Day two permeability and cell behavior analysis was conducted as outlined above after 12 hours of tariquidar exposure. To determine the relative contributions of sequestration and transport of solutes we calculated permeability considering an ROI excluding the lumen and intracellular compartment, and an ROI of the entire image frame.

2.2.5. Cell behavior

To assess endothelial cell behavior in microvessels, we quantified cell area (μm^2), proliferation rate (% h^{-1}), the rate of cell loss (% h^{-1}), turnover rate (% h^{-1}), root mean square (RMS) displacement (μm), path length (μm), number of nearest neighbors, and frequency of nearest neighbor change (h^{-1}) of BC1 dhBMEC microvessels. Details of the protocols have been published previously [219-222]. Phase contrast image sequences from the top and bottom planes were independently analyzed at each time point using ImageJ. Analysis was performed in a region of interest (ROI) ~100 μm wide centered along the top or bottom of the microvessel and over the entire length (typically 5 - 7

mm). This width was selected to minimize foreshortening of the lumen due to microvessel curvature. Any regions along the microvessel length that were significantly out of focus were excluded from the ROI. The total number of cells was quantified by identifying individual cell nuclei within the ROI. Cell area was calculated by dividing the total area of the region of interest by the number of cell nuclei. From analysis of fluorescence images following staining with DAPI and f-actin, we independently verified that there was less than 10% error between the measurements.

The rates of cell proliferation and cell loss were quantified through identification of cell division and loss events within the ROI. Proliferation events are easily identified in time-lapse phase contrast images from cell compression, alignment of chromosomes, and the formation of daughter cells. Cell loss events were readily identifiable through cell compression, lysing of cell contents, and removal of the cell from the monolayer. Events were monitored over the duration of time-lapse imaging and labeled with their location and time at which they occurred. The rates of cell proliferation and cell loss (% h^{-1}) were determined by summing the number of events in the imaging window and dividing by the total number of cells within the ROI (n = 16753 dHBMECs and n = 14042 HUVEC cells sampled for analysis).

To assess cell motility, we tracked the location of the cell nuclei within the region of interest over two hours of imaging. Root mean square (RMS) displacement (μm) is a measure of how far the cell moved from its original position, while path length (μm) is a measure of the total distance cells traverse. At least ten cells were randomly selected over the length of the microvessel per timepoint for motility analysis (n = 291 dHBMECs and n = 171 HUVEC cells sampled for analysis). Using ImageJ, a point was placed on the centroid of the cell nucleus at each frame, resulting in an array of (x, y) coordinate pairs for each time point within the time-lapse sequence. A reference point outside the microvessel was tracked to correct for x-y shifts in the imaging plane.

36

Additionally, from phase contrast images we quantified the number of cell neighbors for each cell, as well as the frequency of change in cell neighbors. Cells are considered neighbors when they share a border, and the number of cell neighbors can change due to proliferation, cell loss, cell movement, or due to redistribution of tight junctions. From analysis of fluorescence images stained for f-actin, we verified that there was less than 10% error in the number of cell neighbors between the two methods.

2.2.6. Immunocytochemistry

On day two after seeding, microvessels were washed with PBS for 5 minutes, fixed with 3.7% paraformaldehyde (Sigma) for 15 minutes, permeabilized with 0.1% Triton X-100 (Sigma) for 15 minutes, and blocked with 1% donkey serum (Sigma) overnight at 4°C. Microvessels were incubated for 6 hours at 4°C with primary antibodies and for 20 minutes at room temperature with Alexa Flour-647 and Alexa Flour-488 secondary antibodies (Life Technologies) (Table 2-1). To localize nuclei or f-actin, 1:500 DAPI solution (Thermo Scientific) and 1:50 AlexaFluor647 phalloidin (Invitrogen) were added, respectively. Confocal z-stacks were obtained on a swept field confocal microscope system (Prairie Technologies) with illumination provided by MLC 400 monolithic laser combiner (Keysight Technologies). To fully reconstruct microvessels, approximately four hundred 0.4 μm slices were acquired using a 40x objective (Nikon).

Table 2-1. Antibodies used in this study.

Antibody	Vendor	Species	Cat. No	Dilution
ZO-1	Invitrogen	Rabbit	402200	1:200
GLUT1	Abcam	Rabbit	115730	1:100
P-gp	Sigma	Mouse	P7965	1:50
Claudin-5	Invitrogen	Mouse	35-2500	1:50
Occludin	Invitrogen	Mouse	33-1500	1:50
Laminin α-4	R&D	Mouse	MAB7340	25 μg/mL
VCAM-1	Abcam	Rabbit	134047	1:50
ICAM-1	R&D	Mouse	BBA3	25 μg/mL

2.2.7. Hyperosmolar microvessel opening

An intra-arterial osmotic procedure is used in neuro-oncology for transient opening of the blood-brain barrier to facilitate drug delivery to tumors. To model this procedure, 250 mg mL^{-1} d-mannitol (Sigma) in brain microvessel media was introduced into the upper media reservoir for five minutes on day two following seeding. Mannitol was then replaced with 200 μM Lucifer yellow and 2 μM Alexa Fluor647-conjugated 10 kDa dextran in brain vessel media. Live-cell imaging and analysis was conducted as previously outlined. Additionally, structural changes observed after exposure to mannitol (i.e. intracellular vacuoles) were counted in ImageJ using time-lapse phase contrast images of microvessel poles cropped to an area of twenty cells; vacuole count was normalized to the number of cells.

2.2.8. Leukocyte adhesion

To determine the effect of tumor necrosis factor alpha (TNFα) activation on permeability and leukocyte adhesion, two media conditions were used. In control experiments, microvessels were perfused with endothelial cell serum-free media supplemented with 1% human platelet poor derived serum and 1% penicillin-streptomycin. To model inflammatory conditions, microvessels were perfused with control media supplemented with 10 ng mL^{-1} TNFα (Thermo Fisher) for 12 hours. On day two, either permeability was tested (as previously summarized) or leukocyte adhesion was tested. For both conditions, microvessels were maintained at ~1 dyn cm^{-2} shear stress using fluid reservoirs directly connected to the inlet and outlets. Human peripheral blood mononuclear cells (PBMCs, StemCell Technologies), predominately comprised on lymphocytes and monocytes, were used for adhesion studies. PBMCs were freshly thawed and resuspended in RPMI-1640 media supplemented with 10% FBS and 1% penicillin-streptomycin before use. Prior to the microvessel experiments, PBMCs were labeled by incubating with 5 μM Calcein AM (Thermo Fisher) in their resuspension media for 30 minutes. PBMCs were added to the inlet at a

concentration of 10^6 cells mL^{-1} and allowed to flow through the microvessel for a duration of 30 minutes. After five minutes of washout, fluorescent images of the microvessel poles and midplane were taken to quantify adherent cells, which were normalized to microvessel length. VCAM-1 and ICAM-1 expression was visualized using immunocytochemistry as previously described.

2.2.9. Statistical Analysis

All statistical analysis was performed using Prism ver. 6 (GraphPad). Experimental metrics (i.e. permeabilities, shear stresses, turnover) are presented as means ± standard error of the mean (SEM). The principle statistical tests used were a student's unpaired t-test (two-tailed with unequal variance) for comparison of two groups and an analysis of variance (ANOVA) for comparison of three or more groups. Reported p values were multiplicity adjusted using a Tukey test. A one sample t-test was used to determine if sample mean was statistically different from zero. Differences were considered statistically significant for $p < 0.05$, with the following thresholds: * $p < 0.05$, ** $p < 0.01$, *** $p < 0.001$, **** $p < 0.0001$.

2.3. Results

2.3.1. Human iPSC-derived brain microvessels express blood-brain barrier markers and maintain stable perfusion over at least six days

Using a templating method we have engineered a functional model of a human brain post-capillary venule (PCV) with stem-cell derived brain microvascular endothelial cells (dhBMECs) (Figure 2-1). In previous work we screened matrix composition, stiffness, and soluble factors to promote adhesion and spreading of dhBMECs in tissue-engineered microvessels [198]. Here, dhBMECs were seeded into a cylindrical 150 μm diameter channel in 7 mg mL^{-1} type I collagen gels, cross-linked with 20 mM genipin and coated with fibronectin and type IV collagen. Additionally, ROCK inhibitor Y27632 was added to promote cell survival over the first 24 hours of culture. Microvessels were continually perfused using gravity-driven flow reservoirs, and from analysis of

volumetric flow rates the wall shear stress was determined to be around 4 dyne cm^{-2}, typical of post-capillary venules. This approach enabled the formation of microvessels with dhBMECs derived from multiple iPSC lines. dhBMEC microvessels formed from the BC1 iPSC line displayed proper localization of the tight junction proteins zonula occludens-1 (ZO-1), claudin-5 (CLDN-5) and occludin (OCLN), and blanket expression of glucose transporter 1 (GLUT1) and the p-glycoprotein (P-gp) efflux pump.

2.3.2. Brain microvessels display physiological barrier function

The permeability of dhBMEC and HUVEC microvessels was determined on days two, four and six from simultaneous measurement of the transport of three fluorescent probes: Lucifer yellow (LY), Rhodamine 123 (R123), and Alexa Flour-647-conjugated 10 kDa dextran (Figure 2-2). LY is a small (444.3 Da) negatively charged water-soluble dye used *in vivo* and *in vitro* to assess BBB integrity. Rhodamine 123 is a small molecule (380.8 Da) that is a substrate for efflux pumps, including p-glycoprotein. 10 kDa dextran conjugated to Alexa Fluor-647 is a large molecular-weight polysaccharide used as a marker of vascular permeability. The global permeability was obtained from the increase in intensity of the imaging ROI during solute perfusion.

Representative phase / fluorescence overlays of microvessels during permeability measurements show perfusion of the solute in the lumen and transport into the ECM (Figure 2-3). BC1 dhBMEC microvessels displayed stable permeability over six days. The permeability of Lucifer yellow was 2.50 ± 0.46 x 10^{-7} cm s^{-1} on day two and did not increase on days four and six (p > 0.05), with an average value of 2.84 ± 0.41 x 10^{-7} cm s^{-1} across all time points. The permeability of Rhodamine 123 in dhBMEC microvessels was 6.61 ± 0.26 x 10^{-7} cm s^{-1} on day two when considering the entire ROI for analysis; however, if the microvessel lumen and cells are excluded it was 1.32 ± 0.16 x 10^{-7} cm s^{-1}. This dramatic difference, which was not observed with other solutes (data not shown), was due to significant intracellular accumulation of the dye. Rhodamine 123 permeability
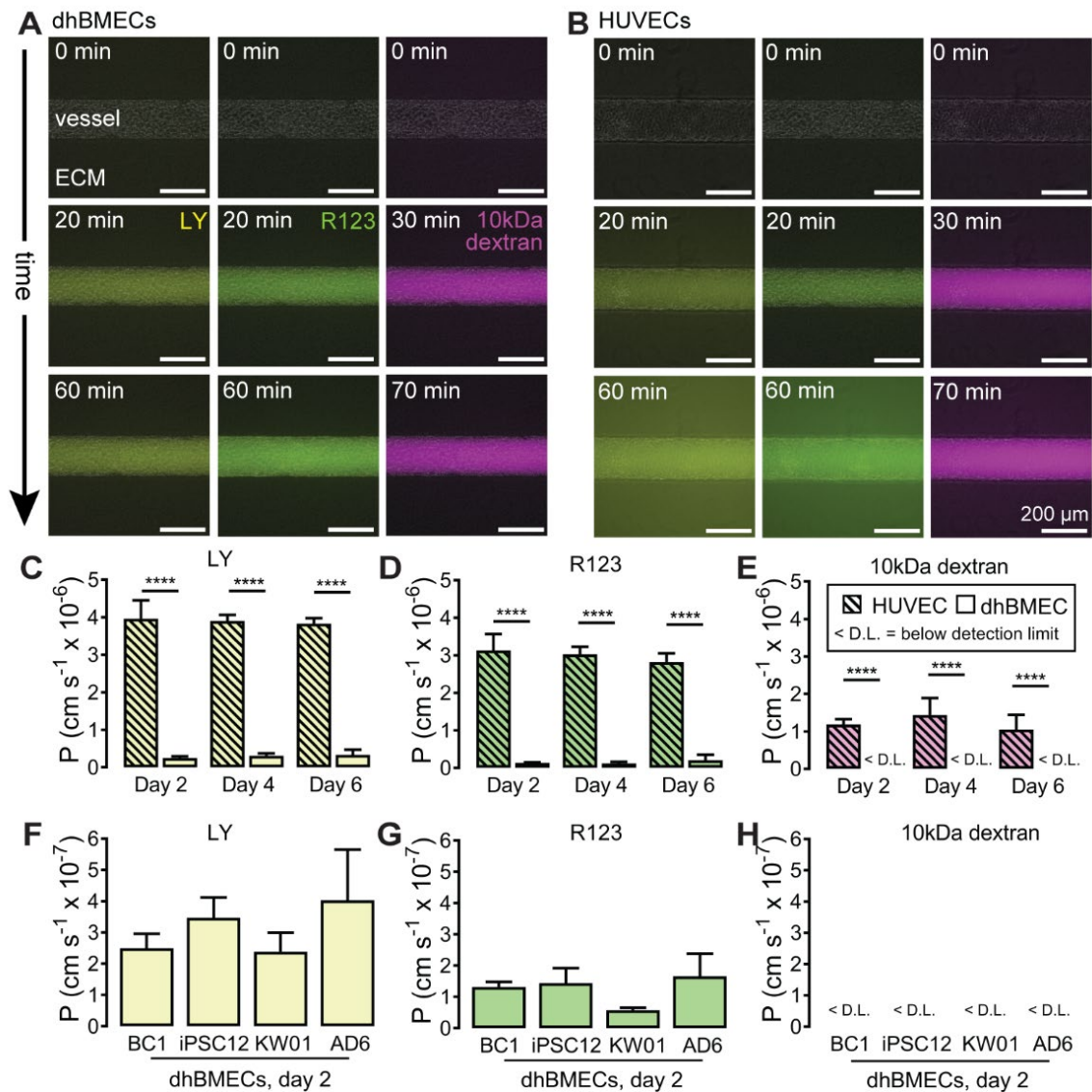
Figure 2-3. Permeability of human iPSC-derived blood-brain barrier microvessels. Representative phase / fluorescence overlays of Lucifer yellow, Rhodamine 123, and 10kDa dextran perfusion in (A) BC1 dhBMEC microvessels, and (B) HUVEC microvessels. t = 0 min represents the frame prior to initiation of luminal filling. Luminal filling occurred on average over 20 minutes for Lucifer yellow and Rhodamine 123, and 30 minutes for 10 kDa dextran. The rate of fluorescence change was determined over subsequent 20 minutes after luminal filling. (C-E) Permeability of Lucifer yellow, Rhodamine 123, and 10 kDa dextran in HUVEC and BC1 dhBMEC microvessels. (F-H) Permeability of Lucifer yellow, Rhodamine 123, and 10kDa dextran, in dhBMEC microvessels derived from multiple iPS cell lines (BC1, iPS12, KW01, AD6) on day two following seeding. Experiments were performed on at least three microvessels for each condition, from at least two independent differentiations.

41

remained stable on day four and six ($p > 0.05$). The permeability of 10 kDa dextran conjugated to Alexa Flour-647 in dhBMEC microvessels was below the detection limit at all timepoints. We observed no plumes of solute entering the ECM associated with focal leaks, indicating tight junction stability.

To assess whether the barrier function of BC1 dhBMEC microvessels was robust, we formed microvessels with dhBMECs derived from the iPS12, KW01 and AD6 lines. The iPS12 line was derived from the cord blood of a healthy female [210]. The KW01 line was derived from a 73-year-old male with multiple sclerosis, and the AD6 line was derived from an individual with Alzheimer's disease with a PSEN1 A246E mutation. Microvessels generated from the iPS12, KW01, and AD6 lines also display low solute permeability. There were no statistically significant differences in Lucifer yellow, Rhodamine 123, or 10 kDa dextran permeability between BC1, iPS12, KW01 and AD6 microvessels on day two ($p > 0.05$ for all comparisons). The barrier function of these four cell lines was also assessed by measuring transendothelial electrical resistance (TEER) in a standard transwell assay, as previously reported [196]. Day two TEER was $2,260 \pm 39$ Ω cm^2 for BC1s, 2260 ± 73 Ω cm^2 for iPS12s, 1330 ± 343 Ω cm^2 for KW01s, and 2160 ± 514 Ω cm^2 for AD6s.

To provide a comparison for the permeability in dhBMEC microvessels, we performed the same experiments in HUVEC microvessels. HUVEC microvessels also display stable permeability over six days. There were no statistically significant differences in permeability between day two, four and six for Lucifer yellow, Rhodamine 123, and 10 kDa dextran ($p > 0.05$ for all comparisons). From the phase / fluorescence overlays, it is evident that the extent of penetration of these solutes into the ECM was significantly larger than in the dhBMEC microvessels. The mean permeability for Lucifer yellow over six days was $3.90 \pm 0.16 \times 10^{-6}$ cm s^{-1}, more than 10-fold higher than in BC1 dhBMEC microvessels. Similarly, the permeability of Rhodamine 123 was $3.00 \pm 0.16 \times 10^{-}$

^{6} cm s^{-1}, about 20-fold higher than in dhBMEC microvessels. The permeability of 10 kDa dextran over six days was 1.23 ± 0.19 x 10^{-6} cm s^{-1}. No focal leaks were observed in HUVEC microvessels during solute perfusion. A similar value for the permeability of 10 kDa dextran and the absence of focal leaks have previously been reported in HUVEC microvessels cultured under similar conditions [213].

2.3.3.Brain microvessels display distinct endothelial cell dynamics

The behavior of endothelial cells was assessed from analysis of phase contrast images at the microvessel poles (Figure 2-4). Rates of cell proliferation, loss, and turnover were determined by direct counting of cell events to eliminates possible errors associated with staining markers to quantify mitosis and apoptosis [223].

In dhBMEC microvessels the proliferation rate decreased significantly over time, from 1.66 ± 0.281 % h^{-1} on day two to 0.199 ± 0.064 % h^{-1} on day six ($p < 0.0001$). The cell loss rate also decreased significantly from 1.015 ± 0.067 % h^{-1} on day two to 0.334 ± 0.083 % h^{-1} on day six ($p = 0.0004$). The net turnover (% h^{-1}), calculated by subtracting the rate of cell loss from the rate of proliferation, decreased from 0.648 ± 0.302 % h^{-1} on day two to -0.134 ± 0.050 % h^{-1} on day six ($p = 0.0121$); the resulting day six turnover was not statistically different from zero ($p = 0.1146$). Proliferation and cell loss events were equally distributed over the entire two-hour imaging window, as evident by linear increases in cumulative events as a function of time ($r > 0.98$ for each plot); while on day two proliferation events occurred more frequently than cell loss events, this trend reversed by day six.

In HUVEC microvessels the rates of proliferation, cell loss, and turnover remained stable over six days ($p > 0.05$ for all comparisons). HUVECs displayed lower cell rates of proliferation and loss than dhBMECs on day two and four ($p < 0.05$ for all comparisons). By day six, the rates of proliferation, cell loss, and turnover were not statistically different between HUVECs and

Figure 2-4. Endothelial cell dynamics of BC1 dhBMEC microvessels. (A, B) Representative time-lapse images depicting cell division and cell loss, respectively. (C-E) Rates of proliferation, cell loss, and turnover rate, respectively, on days 2, 4, and 6 following seeding. (F) Cumulative proliferative and cell loss events during imaging of BC1 dhBMEC microvessels. (G) RMS displacement. (H) Representative path for a dhBMEC (blue line) and HUVEC (black line) cell on day 2 following seeding. (I) Scatter plot showing the change in dhBMEC position over two hours normalized to the initial position for all cells tracked, the average cell displacement vector (x, y) = (1.16 μm, 0.22 μm). (J) Scatter plots of dhBMEC cell path and RMS displacement (dotted black line denotes average cell diameter). (K) Number of cell neighbors. (L) Fluorescence image showing representative six cell neighbors of dhBMEC microvessels. (M) The frequency of change in the number of cell neighbors. (N-O) Fluorescence images showing a stain for f-actin and basement membrane protein laminin α4 on the bottom pole of a microvessel on days 2 and 6. (P) Confocal cross-sections of laminin α4 on days 2 and 6. Experiments were performed on at least three microvessels for each condition, and from at least three independent differentiations.

dhBMECs (p > 0.05 for all comparisons). It is difficult to completely decouple endothelial cell behavior across both cell lines due to differences in media composition; however, high cAMP levels used in both microvessel medias have previously been found to reduce cell turnover [213].

Phase contrast images, DAPI stains, and f-actin stains confirm that the average dhBMEC area ranges from about 600 to 700 μm^2, corresponding to an average cell diameter of ~28 μm. This is a useful metric for comparing length scales of cell motion. Root mean square (RMS) displacement for dHBMECs did not change over time (p > 0.05 for all comparisons) and was on average 8.72 $\pm$ 0.75 μm over two hours of imaging. The RMS displacement for HUVECs was not significantly different than dhBMECs (p > 0.05 for all comparisons), similarly remaining below 10 μm. We observe that the typical dhBMEC and HUVEC displacement was less than the diameter of an average cell, and that the cell motility corresponds predominantly to small fluctuations in position within the monolayer. There was no clear spatial directionality of cell motility, as across all dhBMECs the average displacement vector over two hours of imaging was 1.16 μm, 0.22 μm (x, y). Furthermore, cell path length widely varied between individual dhBMECs, but was on average an order of magnitude higher than RMS displacement.

To assess the spatial organization of endothelial cells within the microvessels, we determined the number of neighbors that share a boundary for each cell. The average number of cell neighbors for both dhBMECs and HUVECs was between six and seven. The frequency of change in number of cell neighbors for dhBMEC microvessels was 0.406 $\pm$ 0.054, suggesting that cells experience a change in number of cell neighbors once every 2.5 hours. This frequency was the same across cell types and time points (p > 0.05 for all comparisons).

To assess cytoskeletal organization, we stained dhBMEC microvessels for f-actin. On day two, f-actin was localized to cell-cell junctions with no preferred orientation. After six days, we also observe some intracellular stress fibers in addition to localization at cell-cell junctions, although

they do not appear to be aligned with flow. These observations have previously been reported for HUVECs in 2D monolayers [221]. To assess basement membrane maturation we stained dhBMEC microvessels for laminin α4; we did not stain for collagen IV and fibronectin as they were used to coat collagen channels to promote cell adhesion. On day two, expression was punctate, but by day six, laminin expression was uniform around the microvessel.

2.3.4. P-gp inhibition

To assess efflux activity, we measured the permeability of Rhodamine 123 with and without the p-glycoprotein inhibitor tariquidar. 2 µM tariquidar treatment increased Rhodamine 123 permeability from 1.32 ± 0.16 x 10^{-7} cm s^{-1} to 2.66 ± 0.44 x 10^{-6} cm s^{-1} ($p = 0.0149$) (Figure 2-5). The permeability of Lucifer yellow and 10 kDa dextran did not change in the presence of tariquidar ($p > 0.05$). Rhodamine 123 accumulates within endothelial cells and results in increasing fluorescence intensity during permeability experiments. The ratio of permeability calculated from the ECM (by excluding the lumen / intracellular compartment) and permeability calculated by the entire imaging frame (P_{ECM} / P_{total}) was ~0.8 for Lucifer yellow in BC1 dhBMEC and HUVEC microvessels, indicating negligible intracellular accumulation. For Rhodamine 123, P_{ECM} / P_{total} was 0.749 ± 0.022 for HUVEC microvessels, 0.203 ± 0.027 for BC1 dhBMEC microvessels, and 0.381 ± 0.031 for tariquidar treated BC1 dhBMEC microvessels. These results show that: (1) dhBMEC microvessels display greater intracellular Rhodamine 123 accumulation compared to HUVECs (as indicated by a lower ratio, $p < 0.0001$) and (2) tariquidar treatment increases the contribution of transcellular transport compared to intracellular accumulation compared to non-treated controls (as indicated by a higher ratio, $p = 0.0046$). We note that Rhodamine 123 is an active mitochondrial stain and increased accumulation could result from a higher mitochondrial density in dhBMECs. The ratio of Lucifer yellow to Rhodamine 123 permeabilities (P_{LY} / P_{R123}) indicates the relative rates of paracellular and transcellular transport. dHBMECs and HUVECs display values of P_{LY} /
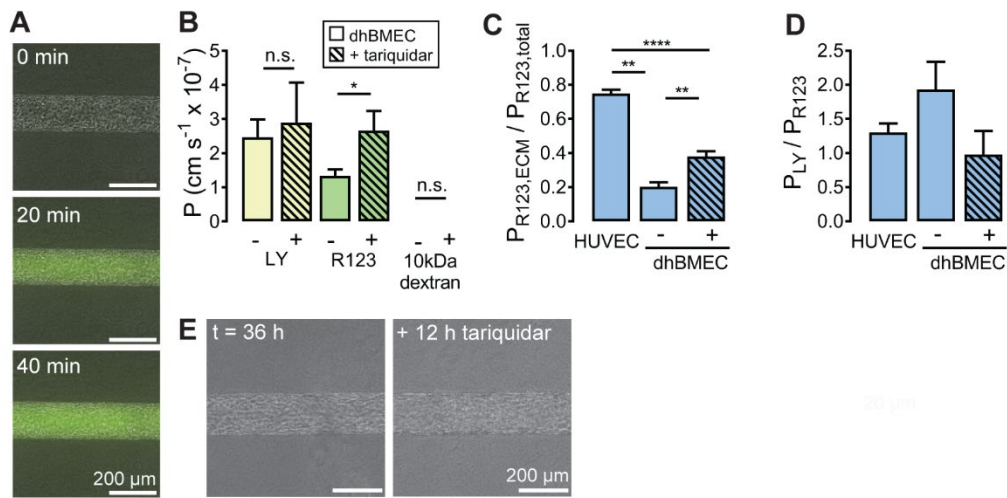
Figure 2-5. Blood-brain barrier efflux inhibition. Microvessels were exposed to 2 μM tariquidar treatment for 12 hours. (A) Phase / fluorescence overlays showing Rhodamine 123 permeability in BC1 dhBMEC microvessels treated with tariquidar for 12 hours. (B) Comparison of BC1 dhBMEC microvessel permeability with and without tariquidar treatment. (C) The ratio of Rhodamine 123 permeability calculated only considering the ECM to including the ECM, lumen and intracellular compartments (P_{ECM}/P_{total}) in HUVEC and BC1 dhBMEC microvessels with and without tariquidar treatment. (D) Ratio of Lucifer yellow permeability to Rhodamine 123 permeability (P_{LY} / P_{R123}). (E) Phase contrast images of BC1 dhBMEC microvessels before and after tariquidar treatment. Data collected from at least three BC1 dhBMEC microvessels, from at least two independent differentiations for each experimental condition.

P_{R123} of ~1.9 and ~1.3, respectively. With 12 hours of tariquidar perfusion P_{LY} / P_{R123} was < 1 suggesting an increase in the transcellular transport (no statistical significance, p > 0.05). Additionally, 12 hours of exposure did not result in apparent cytotoxicity as observed by preserved barrier function and microvessel structure.

2.3.5. Hyperosmolar blood-brain barrier opening

To model a protocol used clinically for transient opening of the BBB, on day two we introduced mannitol (1.4 M) to the upper fluid reservoir for five minutes and then immediately perfused brain microvessels with Lucifer yellow and 10 kDa dextran to study changes in permeability (Figure 2-6). Fluorescence images show both global transport of Lucifer yellow and 10 kDa dextran into
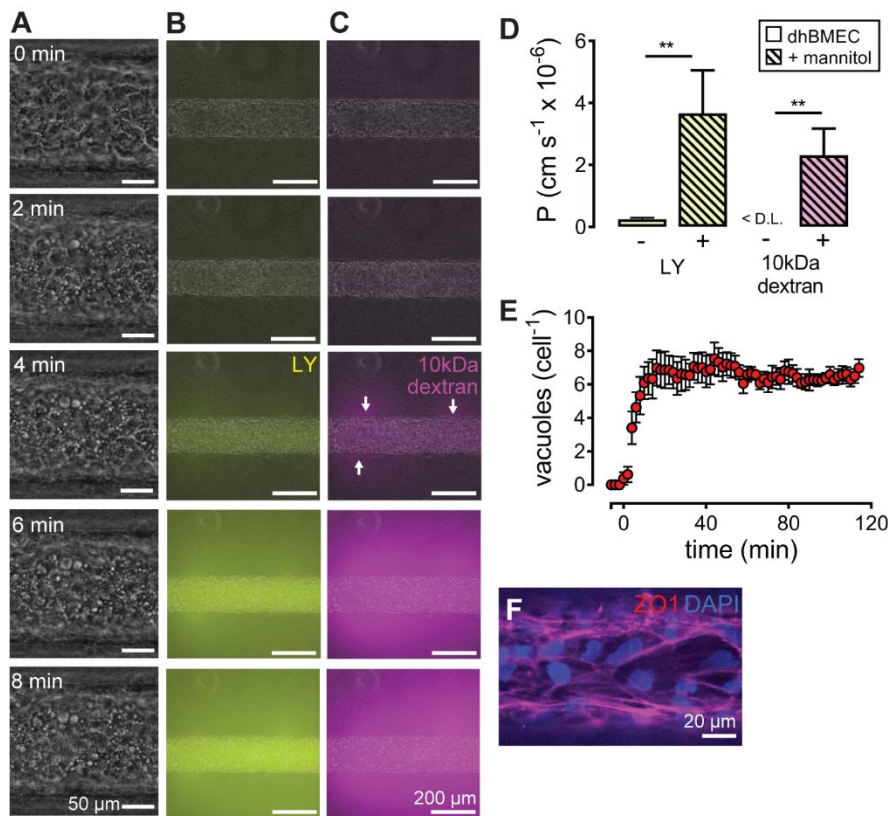
Figure 2-6. Hyperosmolar blood-brain barrier opening. On day two, 1.4 M mannitol was introduced into the upper fluid reservoir for five minutes, followed by Lucifer yellow and 10 kDa dextran. (A) Phase contrast images at the pole of a BC1 dhBMEC microvessel following mannitol exposure. t = 0 represents the frame prior to arrival of mannitol into the lumen. Corresponding phase / fluorescence overlays for (B) Lucifer yellow and (C) 10 kDa dextran. Plumes of 10kDa dextran entering the ECM are marked with arrows. (D) Day two permeability increases with mannitol exposure. (E) Vacuoles per cell over two hours of imaging. (F) Fluorescence image showing f-actin phalloidin stain at the pole of a microvessel following mannitol exposure. Data collected from at least three BC1 dhBMEC microvessels, from at least two independent differentiations for each experimental condition.

the ECM, as well as focal leaks indicating disruption of endothelial cell-cell junctions. Following

mannitol injection, the average permeability of Lucifer yellow was $3.67 \pm 1.39 \times 10^{-6}$ cm s^{-1},

approximately 15-fold higher than homeostatic brain microvessels on day two (p = 0.0025).

Similarly, 10 kDa dextran permeability increased to $2.32 \pm 0.86 \times 10^{-6}$ cm s^{-1} (p = 0.0047). Recall

that the permeability of 10 kDa dextran was not detectable in dhBMEC microvessels. The average

10 kDa dextran permeability was also approximately two-fold higher than the baseline permeability in HUVEC microvessels (1.23 ± 0.19 x 10^{-6} cm s^{-1}), although not statistically significant ($p > 0.05$). The loss of intracellular water following mannitol exposure is associated with formation of vacuoles [224], which are observed in phase contrast images. The number of vacuoles plateaued over approximately 20 minutes following injection of mannitol, reaching a maximum value of approximately six per cell. Lucifer yellow and 10 kDa dextran remain excluded from endothelial cells (images not shown) indicating that vacuoles are not formed by invagination of the plasma membrane. Phalloidin staining following mannitol exposure shows increased stress fiber formation indicating actin cytoskeleton disruption.

2.3.6. Brain microvessels are responsive to cytokine activation

To assess the feasibility that our model can be used to visualize immune cell interactions under inflammatory conditions, we stimulated microvessels with 10 ng mL^{-1} TNFα for 12 hours. Exposure of dhBMEC microvessels to TNFα resulted in upregulation of adhesion molecules ICAM-1 and VCAM-1 (Figure 2-7). In non-treated microvessels ICAM-1 and VCAM-1 expression was punctate, however, following TNFα exposure expression of these adhesion molecules was uniform across the microvessel lumen. Treatment with TNFα did not alter the permeability of Lucifer yellow, Rhodamine 123, or 10 kDa dextran when compared to control microvessels ($p > 0.05$ for all comparisons). Fluorescently labeled human peripheral blood mononuclear cells (PBMCs) were perfused in the microvessels for 30 minutes at a shear stress of ~1 dyne cm^{-2}. Following a five-minute wash out, adherent PBMCs were clearly visible attached to the endothelium. Microvessels exposed to TNFα showed higher numbers of adherent PBMCs (23.0 cells cm^{-1}) as compared to control microvessels (1.75 cells cm^{-1}) ($p < 0.0001$). While transendothelial migration events were not observed during the experiments, microvessels exposed to TNFα with adherent PBMCs displayed macroscopic breakdown within 24 hours.
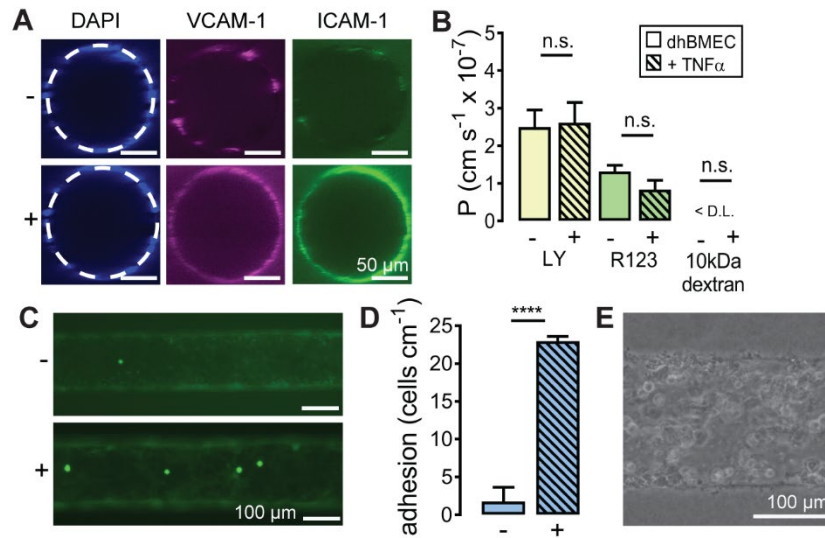
Figure 2-7. Brain post-capillary venular model of leukocyte adhesion during inflammation. (A) Fluorescence images of the cross section of BC1 microvessels showing upregulation of surface adhesion markers (VCAM-1, ICAM-1) following 12-hour cytokine treatment with 10 ng mL^{-1} TNF-α. (B) Permeability of Lucifer yellow, Rhodamine 123, and 10 kDa dextran in BC1 dhBMEC microvessels following treatment with TNF-α. (C) Representative fluorescence images showing PBMCs adhered to the bottom pole of BC1 dhBMEC microvessels with and without cytokine activation. (D) Adhesion of human peripheral blood mononuclear cells (PBMCs) increases with TNF-α exposure. (E) Phase contrast image showing macroscopic breakdown of cytokine treated microvessels exposed to PBMCs within 24 hours.

2.4. Discussion

2.4.1. Barrier function

We have characterized the structure and barrier function of 150 μm diameter microvessels formed using human iPSC-derived BMECs (dhBMECs). Physiological barrier function was established after only two days and maintained for at least four additional days, enabling time course studies of biologically- and clinically-relevant perturbations.

One of the most important functions of the BBB is to restrict access to the brain. Lucifer yellow permeability of BC1 dhBMEC microvessels was 2.84 ± 0.41 x 10^{-7} cm s^{-1} over six days, very close to values that we have previously reported for dhBMEC monolayers in a 2D transwell assay [196], and close to estimated values of 1 - 2 x 10^{-7} cm s^{-1} in 15 μm pial post-capillary venule microvessels

in rats.[225] In addition, the permeability of 10 kDa dextran remained below the detection limit, showing that dhBMEC microvessels effectively block transport of large molecular weight solutes. Numerous studies have shown that dyes (i.e. Evans Blue), which bind to albumin (66.5 kDa), are excluded from the brain implying extremely low permeability [226]. Similarly, four hours after systemic injection of 20 kDa dextran, no dye extravasation was found in the brain parenchyma in a hamster model [227]. However, more recent *in vivo* imaging in rat pial post-capillary venules have reported finite and relatively high permeabilities of about 1 - 2 x 10^{-7} cm s^{-1} for 10 - 70 kDa dextrans [228, 229], which is inconsistent with other results showing restricted transport of large molecular weight solutes across the BBB. Reconciling these differences in *in vivo* permeabilities, which may be due to the substantial regional BBB heterogeneity [230], is important towards validating tissue-engineered models.

Physiological values for TEER are thought to be in the range of 1,500 - 8,000 Ω cm^2 [190-193]. As Lucifer yellow permeability in dhBMEC microvessels was the same as values obtained in transwell assays (where TEER was above 1,500 Ω cm^2), this implies that the transendothelial electrical resistance (TEER) was also likely similar, as previously shown for dhBMECs cultured on hydrogel materials in 2D [198]. Together, these results suggest that we have achieved physiological barrier function within perfusable 3D microvessels. A further implication of these results is that physiological barrier function is dependent on the ability of the hBMECs to form tight junctions, and that other cell types, such as astrocytes and pericytes, are not required for establishment of barrier function. Evidence for this hypothesis comes primarily from *in vitro* transwell experiments where the presence of astrocytes or pericytes (or astrocyte extract) in the basolateral chamber increases TEER [231-237]. However, these experiments were performed with BMECs displaying non-physiological TEER (< 1,500 Ω cm^2). In most of these studies, TEER values increased but did not reach physiological values.

Other strategies for engineering microvessels using primary BMECs, regardless of inclusion of supporting cell types (i.e. pericytes and astrocytes), result in permeabilities still significantly higher than values reported here [186-189]. For example, in one model incorporating primary human BMECs, astrocytes, and pericytes, the permeability of 3 kDa dextran was reported to be 2 - 4 x 10^{-6} cm s^{-1} [187]. As acknowledged by the authors, this high permeability for a large molecule did not recapitulate BBB barrier function, and was likely associated with their reported low TEER values of the primary BMECs (40 - 50 Ω cm^2). Therefore, we hypothesize that rather than being responsible for maintenance of barrier function, it is likely that these supporting cells provide factors that promote recovery of barrier function towards physiological values. This hypothesis is further supported by studies that utilize astrocytes and/or pericytes to improve the barrier function of non-brain specific endothelial cells (HUVEC or iPSC-derived) in microvascular networks [180, 209].

In addition to forming functional microvessels from iPSCs from two healthy individuals (BC1 and iPS12), we also created microvessels from iPSCs from an individual with multiple sclerosis (KW01), and an individual with Alzheimer's disease (AD6). Disruption of the BBB is associated with many neurodegenerative disorders and may manifest through non-cell autonomous toxicity of endothelial cells [131, 179]. Recently, iPSC-derived BMECs from individuals with Huntington's disease (HD) were found to display abnormal barrier function, which may contribute to HD pathology [137]. Here we show that the barrier function of microvessels formed from dhBMECs from individuals with AD and MS show no difference in permeability to Lucifer yellow, Rhodamine 123, and 10 kDa dextran compared to iPSCs from healthy individuals. While these results suggest that the mutations associated with AD and MS in these iPSC lines do not induce changes in permeability, other transport systems have not yet been studied.

2.4.2.Endothelial cell dynamics

Turnover is an important but often overlooked parameter in benchmarking tissue engineered vascular models. The turnover of BMECs in the human brain has not been reported, and there are only limited data from animal models [32, 238, 239] and other tissue beds [240, 241]. Similarly, there are very few studies on the effect of disease (i.e. brain cancer, neurogenerative disease) on brain endothelial cell turnover. Over six days, the turnover of dhBMECs in BC1 microvessels decreases to reach a net turnover rate close to zero. While the proliferation rate was less than values previously reported in 2D dhBMEC monolayers cultured on glass under similar shear stress (0.35 % h^{-1}), the rate of cell loss was significantly higher than in 2D (0.01% h^{-1}) [220]. Results from thymidine labeling studies in mice suggest proliferation rates for BMECs of about 0.04 % h^{-1} [238], an order of magnitude or more lower than endothelial cells in other tissues [240, 241]. Two-photon intravital microscopy studies in adult mice have shown: (1) no change in capillary segment diameter, capillary segment length, and the position of branch points over about 30 days [32], and (2) no detectable endothelial cell division over ten days based on BrdU labeling of cortical microvessels [239]. These results suggest that the rates of cell proliferation and loss need to be further decreased to achieve physiological turnover.

Tracking of dhBMECs in microvessels showed that 96.5% of cells do not move more than an average cell diameter (28 μm) over two hours, as we have shown previously in 2D dhBMEC monolayers [220]. The maximum number of neighbors for an isotropic object in 2D is six, corresponding to a hexagonal or close-packed lattice, whereas for a random distribution the number of cell neighbors is expected to be five. In dhBMEC microvessels, the average number of neighbors for each cell was between six and seven. As we have hypothesized previously, a close packed network of cells (hexagons) is a way to minimize the total length of cell-cell junctions per unit length of vessel [242]. To verify cell shape we traced junctional f-actin stains for 150 cells fixed

on day six. dhBMECs were relatively rounded, with a circularity of about 0.73 and an inverse aspect ratio of about 0.57, similar to values obtained in 2D under static conditions [220], suggesting that the circularity and orientation of dhBMECs was independent of geometry or shear stress. The number of cell neighbors changed once approximately every 2.5 hours for dhBMECs; this rate of change was not due to turnover since the rates of proliferation (0.19 % h^{-1}) and cell loss (0.33 % h^{-1}) mean that the average time for loss / gain of a neighboring cell is about 50 hours. Similarly, this change was not due to migration of cells within the monolayer because most cells do not move more than one cell length. Based on observations from phase contrast videos, we suggest that the changes in neighboring cells are associated with formation and loss of triple junctions that result in dynamic changes in the number of neighbors. Whether these transient changes in the number of cell neighbors play a significant role in determining paracellular permeability remains to be established.

The basement membrane is an important component of the BBB, comprising several proteins including collagen IV, fibronectin, and laminin [243, 244]. Time course actin and laminin stains indicate that dhBMECs are actively modify the surrounding ECM and reorganizing their actin cytoskeleton; the links between these changes and cell behavior remain to be established.

2.4.3. Efflux inhibition

ATP-binding cassette (ABC) efflux transporters including P-glycoprotein (P-gp), actively transport many lipophilic compounds out of brain microvascular endothelial cells, limiting their penetration into the CNS [245]. Important P-gp substrates include anticancer drugs, immunosuppressive agents, antibiotics, corticoids, antivirals, antidepressants, antiepileptic drugs, and many other therapeutics [246]. Thus, modulation of efflux transporters represents a key strategy to improve CNS drug delivery. However, P-gp inhibition has had limited clinical success due to issues with drug toxicity and poor pharmacokinetics [247]. Existing *in vitro* and *in vivo* models of P-gp

inhibition have several limitations. *In vitro* models, such as transwell assays or substrate accumulation assays, enable confirmation of the polarization of efflux transporters to the luminal membrane but do not provide direct visualization of transport phenomena. In contrast, the pharmacokinetics *in vivo* in animal model do not precisely match that of humans [248-250].

Tariquidar is a potent third generation P-gp inhibitor that has undergone multiple preclinical trials to improve drug delivery to the brain [251-253]. Tariquidar plasma concentrations between 2 - 3 µM are utilized to effectively limit P-gp efflux. In our model, 12-hour perfusion of 2 µM tariquidar increased Rhodamine 123 permeability two-fold, while disruptions in paracellular permeability were not observed. In healthy humans, continuous infusion of tariquidar, which was predicted to achieve near complete inhibition of p-glycoprotein, increased the verapamil distribution volume 2.73-fold, similar to the results reported here [252].

2.4.4. Blood-brain barrier opening

Many techniques have emerged to modulate BBB permeability for delivery of therapeutic compounds, including: focused ultrasound [254], enterotoxin analogs [255], siRNA delivery systems [256], and exosomes [257], however, few have been translated to the clinic. Systemic intravenous injection of the hyperosmolar agent mannitol is used clinically to reduce cerebral edema in a wide range of acute conditions [258]. However, bolus intra-arterial injection over 1 - 2 minutes at a high concentration (close to the solubility limit of around 1.4 M), results in endothelial cell shrinkage that is sufficient to induce transient opening of the BBB [259]. Hyperosmolar BBB opening has been used to improve delivery of chemotherapeutics, stem cells, and viral vectors into the brain [260-262]. Despite the more than 100-year history of research into hyperosmotic agents in the brain and the renewed interest in image-guided opening of the BBB [263], the procedure is not reproducible [264] highlighting the need for mechanistic studies at the cellular level. Understanding the processes occurring during hyperosmotic therapy is complicated by the complex

structure and function of brain vasculature. Several major arteries supply the brain and regulation of blood flow by the Circle of Willis results in variable and irreproducible mixing and distribution of solutes throughout the brain. Animal models are valuable for studying these phenomena; however, there are substantial differences in vascular anatomy and cerebral blood flow between humans and animal models [265, 266]. Thus, *in vitro* models provide the opportunity to study hyperosmotic therapy under controlled conditions.

In response to a five-minute bolus of 1.4 M mannitol, we observed a 15-fold increase in the permeability of Lucifer yellow, confirming blood-brain barrier opening. In addition, the permeability of 10 kDa Dextran, which was below the detection limit under baseline conditions, increased to 10-fold higher than Lucifer yellow under baseline conditions. Over two hours of imaging, barrier function remained disrupted, although some leakage of dye was transient. Previous studies have found that mannitol exposure results in transient reductions in TEER both *in vivo* [190] and in *in vitro* culture of primary brain microvascular endothelial cells [267]. From histological studies, brain penetration of herpes simplex virus following hyperosmolar BBB opening suggests a transient defect size up to 120 nm [268]. In our model, mannitol results in leakage of 10 kDa dextran, which has a hydrodynamic size of 4.8 nm [269]. Future studies will explore the reversibility of BBB opening and the dynamics of pore formation. Additionally, hyperosmotic stress resulted in formation of vacuoles within endothelial cells. Vacuole formation is a mechanism to buffer cells against increases in ion concentration that occurs due to the associated decrease in cell volume. Vacuoles formation plateaus after only 20 minutes and remains steady over the subsequent 1.5 hours (despite an only transient exposure to mannitol). Fluorescent solutes were not found to accumulate within the cells suggesting that vacuoles are not direct mediators of BBB disruption during hyperosmotic therapy, as suggested previously *in vivo* [224].

2.4.5. Inflammation

Studies of leukocyte interactions in the cerebrovasculature are usually performed in the autoimmune encephalomyelitis (EAE) mouse model of multiple sclerosis or in 2D *in vitro* models [270, 271]. We show that it is possible to study leukocyte dynamics within 3D models of human post-capillary venules, which supports visualization in a well-controlled environment [272]. Immune trafficking across the BBB is low under physiological conditions, however, increased infiltration is implicated in neurological disease [273]. Endothelial ICAM-1 and VCAM-1 expression promotes leukocyte adhesion [274, 275], an early step in extravasation, which occurs preferentially in PCVs of the brain [203-205]. In BC1 dhBMEC microvessels, exposure to inflammatory cytokine TNFα resulted in upregulation of VCAM-1 and ICAM-1, and corresponding increased adhesion of human peripheral blood mononuclear cells.

We also found that TNFα activation resulted in no change in barrier function. This observation is contradictory to results from *in vitro* 2D models [276-279], existing 3D BBB models [187, 188], and *in vivo* animal models [280], all of which report increased permeability of BMECs exposed to TNFα. However, as described previously, *in vitro* models utilizing BMECs with non-physiological TEER may be more susceptible to disruptive changes in barrier function [281]. Therefore, our results suggest that TNFα stimulation alone, without other blood components and conditions associated with an immune response, is insufficient to induce BBB disruption. Interestingly, 24 hours after TNFα activation and PBMC adhesion studies, microvessels displayed macroscopic breakdown suggesting a possible role of cytokine secretion. In our model, no transendothelial migration events were observed, presumably since there was change in barrier function, but also potentially due to the restrictive nature of a dense cross-linked collagen hydrogel. Although they lack the biological complexity of animal models, these proof-of-principle results highlight a

57

potential advantage of *in vitro* models to deconvolve complex processes occurring during inflammation.

2.5. Conclusions

We report on barrier function and endothelial cell behavior of human iPSC-derived blood-brain barrier microvessels resembling *in vivo* post-capillary venules. Microvessels are generated from multiple iPS cell lines and display localization of tight junction proteins, and expression of key transporters and efflux pumps. Physiological barrier function is achieved within two days, requires no co-cultured cells, and is maintained for at least four days. Over the course of six days, endothelial cells reach quiescence and develop a uniform basement membrane. We demonstrate successful modulation of both transcellular and paracellular permeability using P-gp inhibitor tariquidar and hyperosmolar agent mannitol, respectively. Cytokine activation using TNFα resulted in upregulation of leukocyte adhesion molecules (VCAM-1 and ICAM-1) and increased leukocyte adhesion, but resulted in no change in permeability suggesting that activation alone is insufficient to induce BBB disruption. Human iPSC-derived blood-brain barrier microvessels serve as a robust patient-specific platform to study transport phenomena and endothelial cell behavior during health and disease.

Chapter 3. Modeling hyperosmotic blood–brain barrier opening within human tissue-engineered in vitro brain microvessels

Raleigh M. Linville,[1,2] Jackson G. DeStefano,[1,3] Matt B. Sklar,[1] Chengyan Chu,[4] Piotr Walczak,[4] Peter C. Searson[1,2,3]

[1] Institute for Nanobiotechnology, Johns Hopkins University, Baltimore, MD

[2] Department of Biomedical Engineering, Johns Hopkins University, Baltimore, MD

[3] Department of Materials Science and Engineering, Johns Hopkins University, Baltimore, MD

[4] Department of Radiology and Radiological Science, Johns Hopkins University School of Medicine, Baltimore, MD

3.1. Introduction

The human blood-brain barrier (BBB) restricts delivery of therapeutics to the brain for treatment of CNS disease [283]. Tight junctions (TJs) between adjacent brain microvascular endothelial cells (BMECs) restrict paracellular transport of solutes, while expression of efflux pumps regulates transcellular transport [3]. Therefore, drug therapies are largely limited to small lipophilic molecules that have moderate to high rates of passive transport across BMEC membranes. However, reversible disruption of TJs can be exploited to transiently increase bioavailability of a broad range of therapeutics into the brain [284, 285].

Intra-arterial (IA) infusion of hyperosmotic agents, such as mannitol, is one approach for transient BBB opening (BBBO) [259]. Drug delivery techniques based on IA administration have distinct advantages including high regional drug concentration, high spatial selectivity, rapid onset of action, and limited systemic dose [286]. Systemic intravenous (IV) administration of mannitol is widely used in the clinic to reduce cerebral edema, however, IA injection at a sufficiently high concentration (close to the solubility limit of around 1.4 M), causes BMEC shrinkage which is sufficient to induce transient BBBO [259, 287, 288]. This technique has been used for several decades in both preclinical models and clinical studies to improve delivery of chemotherapeutics, stem cells, and gene vectors [260-262, 289-293]. The reproducibility of BBBO can be difficult to control due to dilution of the injected dose by collateral blood supply in the Circle of Willis, as well as more distally in microcirculation [265, 294]. Advances in image-guided insertion of catheters beyond the Circle of Willis into specific locations in the cerebrovasculature have renewed interest in hyperosmotic BBBO for delivery of therapeutic and diagnostic agents [263, 292, 295, 296].

Although hyperosmotic therapies have been studied for more than 100 years [297], the mechanism of action is not fully elucidated. The current model of hyperosmotic BBBO assumes that water loss from BMECs into the capillary lumen induces vasodilation, resulting in a homogeneous increase in BBB permeability [259]. Much of what we know about hyperosmotic therapies relies on magnetic resonance imaging (MRI) and positron emission tomography (PET) [295]. However, these techniques are not well suited for interrogating mechanisms at the cellular level. Here, we report on real-time imaging of hyperosmotic BBBO on the scale of individual cells in a tissue-engineered microvessel model of the cerebrovasculature incorporating stem cell-derived human BMECs (dhBMECs) [26, 181, 198]. From fluorescence imaging of different molecular weight solutes following exposure to different mannitol doses, we assess spatial and temporal changes in barrier function, while from phase contrast imaging we assess changes in BMEC structure. The key observations are: (1) mannitol causes transient focal leaks that result in a significant increase in the overall permeability, (2) the focal leaks occur at small (1 – 2 μm) sub-cellular disruptions in the endothelium, (3) the global TJ network is unaffected by mannitol, and (4) the increase in permeability is due solely to paracellular transport. We establish the timeline of events following hyperosmotic BBBO, including spatially heterogenous increases in paracellular permeability and BMEC vacuolation. Finally, we show that bFGF has an important role in modulating the susceptibility to BBBO and recovery. Our results highlight the ability to evaluate drug delivery mechanisms using a tissue-engineered microvessel model of the human BBB.

3.2. Materials and Methods

3.2.1. MRI during BBBO in mice

Animal experiments were performed in accordance with guidelines for the care and use of laboratory animals approved by the Institutional Animal Care and Use Committee of Johns Hopkins University, designed in compliance with the Animal Welfare Act regulations and Public Health

Service (PHS) policy, and were performed in accordance with ARRIVE guidelines. Four SCID mice (male, 6-8 weeks old, 20-25 g, Jackson Laboratory) were used in this study. Carotid artery catheterization was performed as previously described [295], before mice were transferred to a Bruker 11.7 T MRI scanner. T1 (TR/TE 350/6.7ms)-weighted and dynamic T1 imaging (TR/TE 2000/3.5ms, field of view = 14×14 mm, acquisition time = 8 s and 40 repetitions) of the brain was acquired. 1.4 M mannitol (Hospira) was administered intra-arterially for 1 minute at an injection speed of 0.15 ml min^{-1}. Five minutes after mannitol dosing, mice received 0.07 mL of Gadoteridol (Gd; Bracco Diagnostics) intraperitoneally. T1-weighted images were obtained 5 minutes post-Gd injection to visualize BBB integrity; for dynamic monitoring of BBBO, T1 scans were acquired during and after a 1-minute infusion of 1.4 M mannitol mixed with Gd (5.6 mg/mL).

1 mm x 1 mm regions of interest (ROIs) were drawn on MRI images corresponding to: (1) contralateral hippocampus, (2) contralateral cerebral cortex, (3) ipsilateral cerebral cortex, and (4) ipsilateral hippocampus. The Gd contrast ratio post-mannitol versus pre-mannitol was computed using ImageJ (NIH) and normalized to contralateral hippocampus (ROI 1; where BBBO does not occur). For dynamic T1 measurements identical ROIs were used and contrast intensity (normalized between 0 and 1 for ROI 4) plotted over five minutes.

3.2.2. Blood-brain barrier microvessel fabrication

Human brain microvascular endothelial cells (dhBMECs) were differentiated from induced pluripotent stem cells (iPSCs) as previously reported [181, 196]. The BC1 iPSC line derived from a healthy individual was used for all experiments [210]. BC1 dhBMECs show transendothelial electrical resistance (TEER) values above 1500 Ω cm^2 in two-dimensional culture, when cultured in media supplemented with retinoic acid [196, 298].

BBB microvessels were fabricated as previously reported [181, 198]. The microfluidic device consists of a 150 μm diameter and 1 cm long microvessel lined with BC1 dhBMECs in a genipin-

cross-linked type I collagen hydrogel contained in a polydimethylsiloxane housing. Inlet and outlet fluid reservoirs are connected to a flow loop to maintain a shear stress of approximately 4 dyne cm^{-2} [181, 198]. Functional BBB microvessels with physiological barrier function are formed two days following seeding dhBMECs in the microfluidic device [181, 198]. After establishing barrier function (defined as day 0), timelapse imaging experiments were initiated.

Microvessels were perfused with media (denoted as BBB microvessel media): human endothelial cell serum-free media (Life Technologies) supplemented with 1% human platelet poor derived serum (Sigma), 1% penicillin-streptomycin (Life Technologies), 400 μM db-cAMP (Sigma), 20 μM phosphodiesterase inhibitor Ro-20-1724 (Calbiochem), 3% 70 kDa dextran (Sigma), and 10 μM ROCK inhibitor Y27632 (ATCC, only supplemented for first 24 hours after seeding). Where noted, 20 ng mL^{-1} recombinant human basic fibroblast growth factor (R&D systems; 146 aa, bFGF) was supplemented for either the initial 24 hours of device perfusion (day -2 to day -1) or for 48 hours following imaging experiments (day 0 to day 2).

3.2.3. Live-cell imaging of BBB opening

The experimental design and timeline of dosing and assessment of barrier function during live-cell imaging is summarized in Figure 3-1. Microvessels were maintained at 37 ˚C and 5% CO_2 in a live-cell chamber, and imaged on an inverted microscope (Nikon Eclipse TiE). Epifluorescence illumination was provided by an X-Cite 120LEDBoost (Excelitas Technologies). On day 0 (two days after seeding microvessels), media was removed from the upper reservoir and replaced with 1.4 M mannitol (Sigma) and 5 μM Sodium fluorescein (Sigma) prepared in BBB microvessel media for two, five, or ten minutes depending on the mannitol dose. After dosing, the upper reservoir was replaced with BBB microvessel media containing 200 μM Lucifer yellow (CH dilithium salt; LY) (Sigma) and 2 μM Alexa Fluor647-conjugated 10 kDa dextran (Thermo Fisher). A NIS Elements (Nikon) imaging protocol was initiated immediately following addition of Lucifer yellow and 10
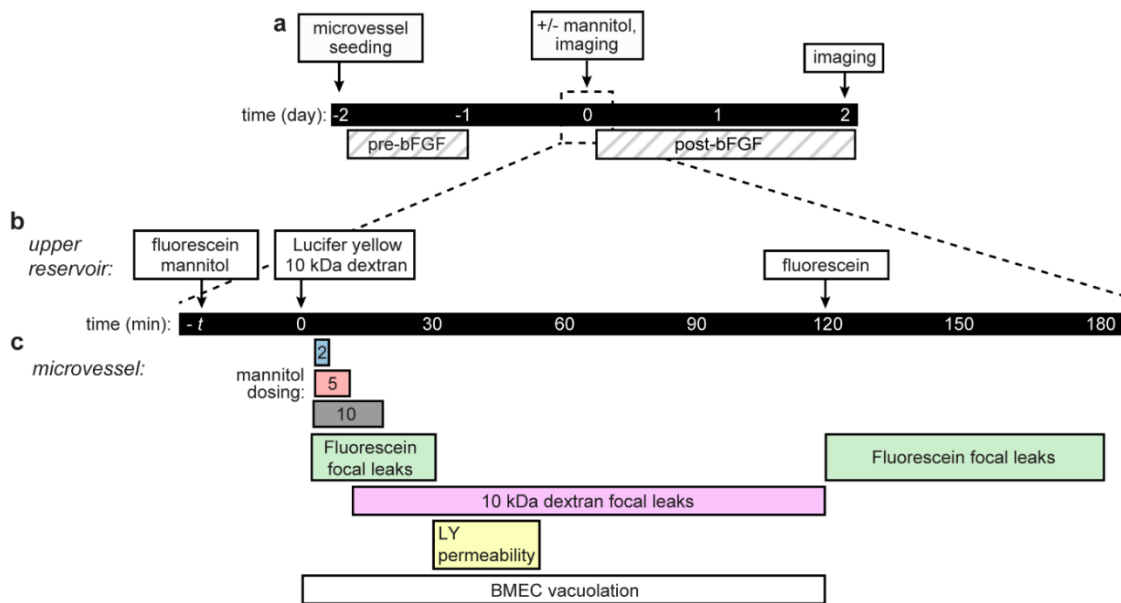
Figure 3-1. Live-cell imaging experimental design and timeline. Timeline over four days. Devices are seeded with dhBMECs (day -2) and form into BBB microvessels over two days. On day 0, microvessels are dosed with or without mannitol and imaging is conducted. On day 2 (48 hours later) imaging is conducted again. bFGF treatment is applied for the initial 24 hours after seeding, or for 48 hours after day 0 imaging. (b) Fluorescein and mannitol are added to the upper reservoir at time -2 to -10 minutes. Next, Lucifer yellow and 10 kDa dextran are added and the microfluidic device is immediately imaged for two hours. Afterwards, microvessels are re-exposed to fluorescein for one hour. (c) 2, 5 and 10-minute mannitol doses are visible in the microvessel as fluorescein fluorescence shortly after imaging begins. Fluorescein focal leaks are counted during mannitol dosing and during fluorescein re-administration. Once, 10 kDa dextran enters the microvessel lumen focal leaks are counted over the remaining 2-hour imaging window. Lucifer yellow (LY) permeability is calculated over 20 minutes following luminal filling. BMEC vacuolation is counted over the entire 2-hour imaging window.

kDa dextran to the upper reservoir. Phase contrast and fluorescence images were acquired every two minutes for two hours (61 frames). At every time point six images were collected: (1) a phase contrast image of the top of the microvessel, (2-5) phase contrast and fluorescence images of the microvessel midplane, and (6) a phase contrast image of the bottom of the microvessel. To independently excite and collect the emission from each fluorophore, three filter cubes were used: Chroma 39008 for Lucifer yellow (20 ms exposure), Chroma 49003 for fluorescein (50 ms

exposure), and Chroma 41008 for dextran (200 ms exposure). The total image area was approximately 8.2 mm x 0.67 mm, corresponding to ten adjacent frames using a 10x objective. Mannitol (MW 182.2) dosing was indirectly monitored using co-administered fluorescein (MW 376.3 Da), a small fluorescent compound that does not exhibit intracellular accumulation. Fluorescein begins filling the microvessel several minutes after imaging is initiated due to transit within 40 cm long tubing, which connects the upper reservoir and microvessel (Figure 3-5, A). Since convective flux is proportional to fluid velocity and not dependent on the physicochemical properties of a solute, it is reasonable to assume that mannitol and fluorescein are transported at the same rate; therefore, the fluorescein intensity can be used as a proxy to identify the duration and maximum of the mannitol dose. After two hours of imaging, microvessels were re-perfused with fluorescein for one hour to monitor recovery of barrier function.

3.2.4. Spatial permeability analysis

Analysis is summarized in Figure 3-2. Large images were sectioned into ten regions of interest (ROIs), each with dimensions of 820 μm x 670 μm. Time course fluorescence intensity profiles of Lucifer yellow were obtained using ImageJ. Microvessel permeability (cm s^{-1}) was calculated as $P = (d/4)(1/\Delta I)(dI/dt)$, where d is the vessel diameter, ΔI is the increase in fluorescence intensity upon luminal filling, and $(dI/dt)_0$ is the rate of increase in fluorescence intensity as the solute is transported across the endothelium into the surrounding matrix [216, 217]. The rate of increase of fluorescence intensity, from which the permeability is calculated, was determined from a linear least squares fit over twenty minutes following luminal filling. Lucifer yellow permeability was calculated for each of the ten ROIs, with the minimum across all ROIs reported as $P_{min}(LY)$. Five adjacent ROIs with the lowest mean permeability were used to analyze spatial heterogeneity of BBBO; ROIs outside this range were discarded from analysis as they were not buffered from slow

interstitial leakage of dye into the hydrogel from the inlet and outlet, which artificially increases permeability values.

Focal leaks induced by mannitol were manually counted in ImageJ. Focal leaks appear as radial extravascular plumes of fluorescence due to diffusion of dye into the hydrogel from the leakage site. Focal leaks were counted over the initial dosing of mannitol and over the one-hour fluorescein re-administration. In the 2 hours following dosing, the x-position along microvessels (from 0 to 8,200 μm) and time of appearance of individual 10 kDa dextran focal leaks were recorded. The total number of 10 kDa dextran focal leaks during two hours following dosing was normalized to microvessel length (# cm^{-1}). To assess penetration of 10 kDa dextran into the surrounding matrix, the fluorescence intensity was determined in the five adjacent ROIs with the lowest mean permeability excluding the microvessel lumen, corresponding to two-thirds of the imaging frame (total area = 1.83 mm^2). Within this region, the normalized cumulative and instantaneous change in fluorescence intensity was plotted as a proxy for drug extravasation.
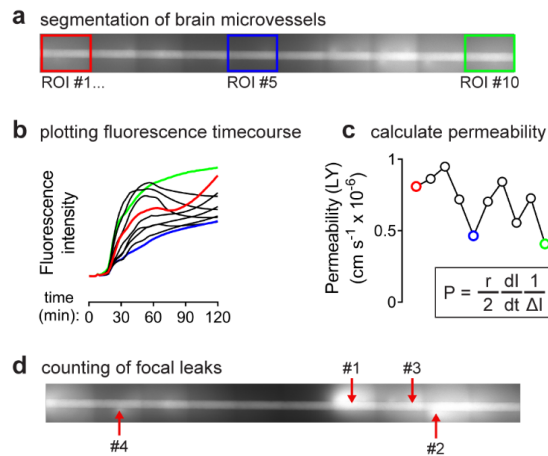
Figure 3-2. Spatial permeability analysis. (a) Microvessels are sectioned into ten regions of interest (ROIs). (b) Fluorescence is plotted over two hours for each ROI. (c) Permeability is extrapolated from the shape of the curve, critical inputs are the jump in fluorescence intensity due to luminal filling (ΔI), the rate of increase in fluorescence after filling (dI/dt) and the microvessel radius. (d) Focal leaks are manually counted from fluorescein and 10 kDa dextran fluorescence images.

3.2.5. Phase contrast analysis

Structural changes observed after exposure to mannitol (i.e. intracellular vacuoles) were counted in ImageJ using time-lapse phase contrast images at the microvessel poles cropped to an area of twenty cells; the vacuole count was then normalized to the number of cells (# cell^{-1}). Vacuole quantification was verified by comparison to the corresponding fluorescence images following treatment with 2 μM Calcein AM (ThermoFisher), which stains all intracellular compartments besides vacuoles (Figure 3-7, A). Vacuole density did not vary substantially along the x-axis of microvessels, justifying sampling of a single region containing twenty cells (Figure 3-7, B).

To probe vacuole localization and function, four fluorescence assays were used: 2 μM Calcein AM for live cells, 4 μM ethidium homodimer-1 (ThermoFisher) for dead/dying cells, 2 μg mL^{-1} Hoechst 33342 (ThermoFisher) for nuclei, and pHrodo™ Green AM Intracellular pH Indicator (ThermoFisher) for intracellular pH (following manufacturer suggested protocols). For these experiments, microvessels were: (1) washed with live-cell imaging solution (LCIS; ThermoFisher) for 5 minutes, (2) stained at 37 ˚C for 30 minutes, (3) washed with LCIS for 5 minutes, and (4) imaged as previously described.

Cell loss events were recorded from time-lapse imaging at the microvessel midplane. These events are visible as BMECs balling-up and detaching from the endothelium. Events were normalized to the length of microvessel, based on analysis within representative ~465 μm long microvessel image sections. Cell density was determined by manual counting in a 32,000 μm^2 area at the pole region of a microvessel (~100 cells).

3.2.6. Confocal and epifluorescence imaging of hyperosmotic BBB opening

Blood-brain barrier microvessels were constructed using the WTC iPSC line with CRISPR-edited tagging of zona occludens-1 (ZO1) with enhanced green fluorescent protein (EGFP) [299]. 5-minute mannitol doses were administered as previously described. However, fluorescein and

Lucifer yellow were excluded from experiments due to fluorescence overlap with the fluorescently-tagged ZO1. Instead, 10 kDa dextran was supplemented within the brain microvessel media during and after mannitol dosing to monitor formation and recovery of focal leaks. 10× epifluorescence and 40× confocal images were collected as previously described [300].

3.2.7. bFGF pre-treatment in two-dimensional assays

Upon completion of the differentiation, dhBMECs were singularized using warm Accutase for 10 minutes. Corning® Transwell® polyester membrane cell culture inserts (1.12 cm^2 area, 0.4 μm pore size) and eight-chambered borosilicate cover glass wells (Lab Tek) were seeded at 1×10^6 cells cm^{-2}. All surfaces were coated overnight with 50 μg mL^{-1} human placental collagen IV (Sigma) and 25 μg mL^{-1} fibronectin from human plasma (Sigma). Two cell culture medias were tested: (1) BBB microvessel media (as outlined in methods) and (2) BBB microvessel media supplemented with 20 ng mL^{-1} recombinant human basic fibroblast growth factor. TEER recordings and immunocytochemistry were conducted 48 hours after plating on transwells (day 0) as previously described [196]. The density of DAPI-stained nuclei was calculated using particle analysis in ImageJ. Normalized fluorescence intensity of 10× images of zona occludens-1 (ZO1) or claudin-5 stained monolayers was used as a proxy for protein expression.

3.2.8. Statistical analysis

All statistical analysis was performed using Prism ver. 8 (GraphPad). Metrics are presented as mean ± standard deviation (SD). The principle statistical tests used were a student's unpaired t-test (two-tailed with unequal variance) for comparison of two groups, and an analysis of variance (ANOVA) for comparison of three or more groups. Reported p-values were multiplicity adjusted using a Tukey test. Differences were considered statistically significant for $p < 0.05$, with the following thresholds: * $p < 0.05$, ** $p < 0.01$, *** $p < 0.001$. To determine the time course of

experimental metrics, the beginning of the mannitol dose is designated as t = 0 and the half-time represents the time following dosing at which the metric reaches half its maximum value.

3.3. Results

3.3.1. Hyperosmotic blood-brain barrier opening in mice

To establish a clinically relevant comparison for *in vitro* experiments, *in vivo* measurements of BBBO following mannitol dosing were performed in a mouse model. Contrast enhanced T1 MRI, a standard technique for monitoring BBB status both clinically and in animal models [295], was used to imaging of BBBO following dosing with mannitol. At hemodynamically safe IA infusion rates, consistent BBBO occurs in subcortical brain structures (primarily the hippocampus), while the cerebral cortex and the contralateral brain regions are not reproducibly opened (Figure 3-3, A). The Gadoteridol (Gd) contrast enhancement after mannitol dosing (compared to the value to before dosing) and normalized to the unaffected brain ROI, shows robust opening in the ipsilateral hippocampus (> 2-fold increase) compared to other regions ($p < 0.01$ for each comparison) (Figure 3-3, B). Due to the relatively low spatial resolution of MRI, opening appears to result in a uniform increase in permeability. Additionally, high spatial resolution using multiphoton microscopy is not possible in mice as BBBO is not reproductively observed in superficial brain regions [295].

A 1-minute injection of mannitol, along with Gd, during real-time T1 MRI demonstrates the temporal and spatial signature of BBBO in the mouse brain (Figure 3-3, C). Analysis of the ipsilateral hippocampus (ROI 4) shows that BBBO occurs shortly after cessation of mannitol infusion (less than one minute later) (Figure 3-3, D). Additionally, while MRI enables non-invasive assessment of BBBO, precise calculations of vascular permeability are complicated because gadolinium is a contrast agent rather than a tracer, and T1 relaxivity-derived measures lack precision [301].
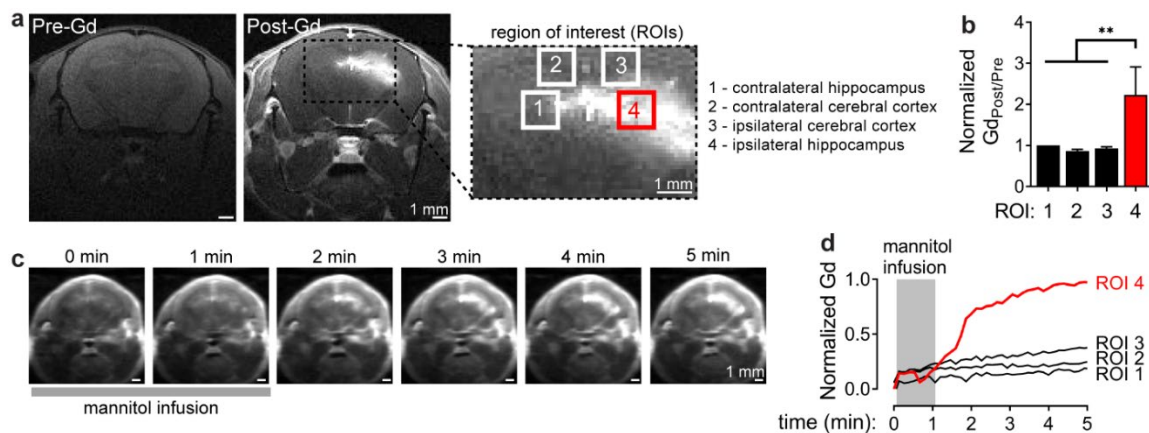
Figure 3-3. Hyperosmotic BBB opening in mice. (a) T1 magnetic resonance (MR) images were acquired before 1-minute 1.4 M mannitol infusion and 5 minutes after subsequent Gadoteridol (Gd) injection. (b) The ratio of Gd contrast post- and pre-mannitol exposure (normalized to ROI 1). The ipsilateral hippocampus displays Gd enhancement, while other regions do not. (c) T1 images during and after a 1-minute 1.4 M mannitol injection with Gd. (d) Dynamics of normalized Gd contrast across ROIs; only the ipsilateral hippocampus (ROI 4) displays significant enhancement, which occurs rapidly following cessation of mannitol infusion. Pre/Post T1 (n = 4 mice), dynamic T1 (n = 1 mouse).

3.3.2. Mannitol induces spatially heterogenous and dose-dependent increases in solute permeability in a tissue-engineered BBB model

To study the mechanisms of hyperosmotic BBBO, we introduced mannitol into a tissue-engineered model of the BBB with a single 1 cm long microvessel that mimics the dimensions (~ 150 μm diameter) and wall shear stress (4 dyne cm^{-2}) of a post-capillary venule (Figure 3-4, A-B) [181]. Two days after seeding stem cell-derived human BMECs into genipin-crosslinked collagen channels (day 0), the formation of a confluent monolayer (Figure 3-4, C) results in physiological barrier function, as previously reported [198]. Microvessels were perfused with mannitol and the tracer fluorescein for 2 or 5 minutes. Following dosing, the microvessels were then perfused with the fluorescent probes Lucifer yellow and 10 kDa dextran (Figure 3-4, D-E). During this process, phase contrast microscopy was used to monitor the status of the endothelium, and epifluorescence imaging was used to visualize the transport of fluorescein, Lucifer yellow, and dextran out of the
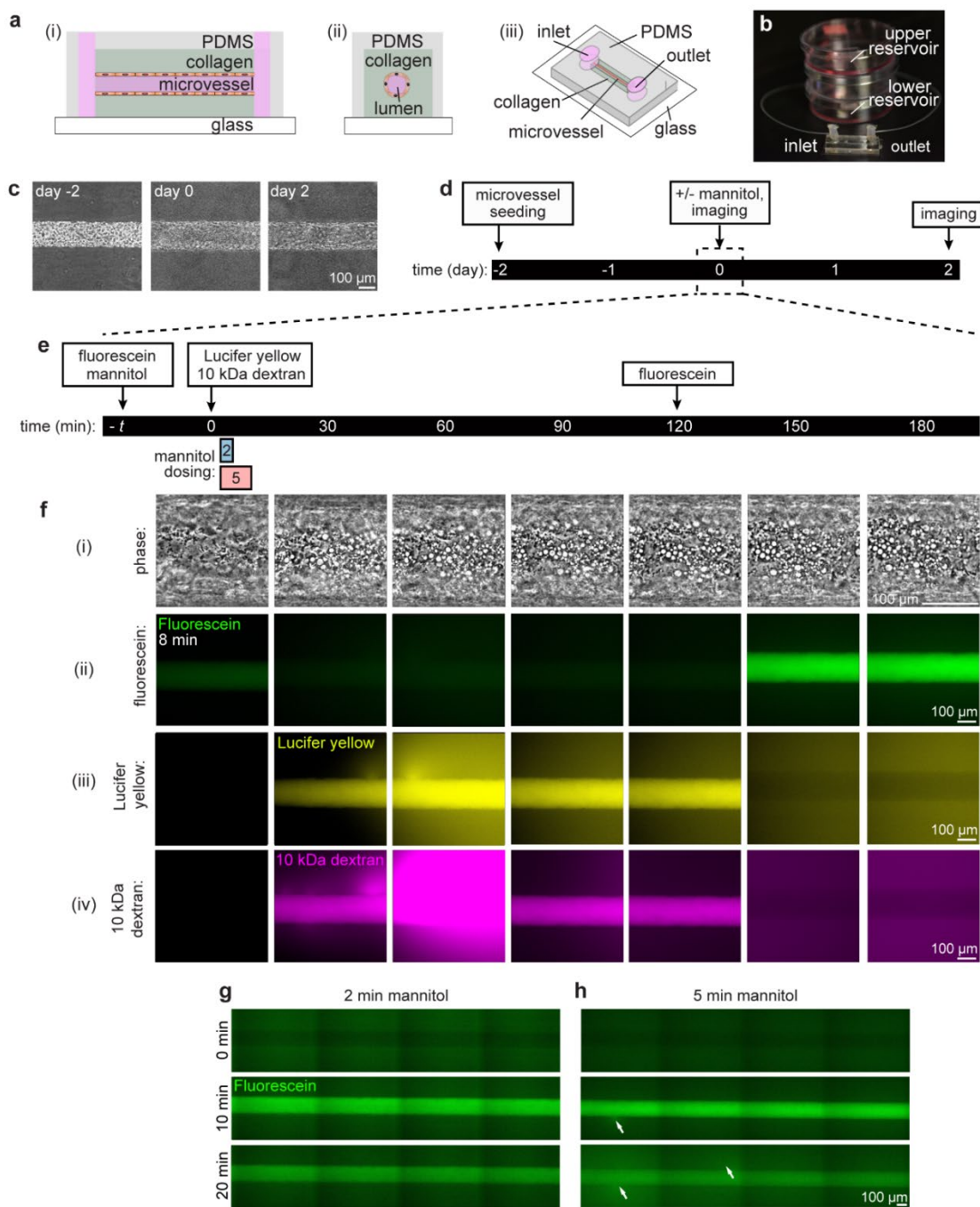
Figure 3-4. Three-dimensional human in vitro model of hyperosmotic BBB opening. (a) Schematic illustrations of tissue-engineered iPSC-derived BBB microvessels including: (i) side view, (ii) front view, and (iii) three-dimensional view. (b) Microvessels are continually perfused at ~4 dyne cm⁻² shear stress via gravity-driven flow reservoirs. (c) Phase contrast images of microvessel following seeding (day -2), microvessel formation (day 0) and 48 hours later (day 2).

(d) Experimental timeline over four days. (e) Imaging protocol for studying human BBB opening. Mannitol and fluorescein are added to the upper reservoir for two, five or ten minutes. Next Lucifer yellow and 10 kDa dextran are added to the upper reservoir for two hours. Fluorescein is re-administered for another hour. (f) Timelapse images of: (i) phase, (ii) fluorescein, (iii) Lucifer yellow, and (iv) 10 kDa dextran are shown for a representative microvessel dosed with 1.4 M mannitol for five minutes. (g-h) Representative fluorescence images of fluorescein during 2-minute and 5-minute mannitol doses. Fluorescein focal leaks are widely observed during 5-minute exposure. White arrows denote the sites of focal leaks.

lumen and into the surrounding matrix (shown for a representative 5-minute mannitol dose in

Figure 3-4, F).

Fluorescein provides a proxy for the time-dependent concentration of mannitol in the microvessel

and enables visualization of BBBO during and immediately after (~10 minutes) mannitol dosing.

Fluorescein focal leaks develop during dosing, indicating that BBBO occurs rapidly following

exposure to mannitol. The densities of focal leaks during dosing were 0.24 ± 0.54 cm^{-1} and $5.59 \pm$

4.35 cm^{-1} for 2-minute and 5-minute mannitol doses, respectively (Figure 3-5).
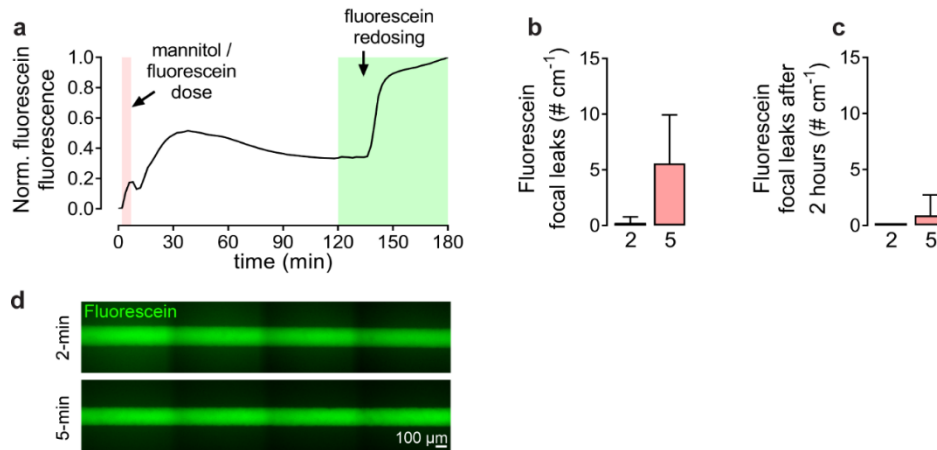
Figure 3-5. Fluorescein tracing of BBB microvessels. (a) Time course of fluorescein fluorescence for representative 5-minute mannitol microvessel. Fluorescein fluorescence peaks during mannitol dosing. Re-administration of fluorescein is used to monitor short-term recovery of barrier function. (b) Fluorescein focal leaks (n = 5 for each mannitol dose). Only 5-minute mannitol exposure results in robust focal leak formation. (c) Fluorescein focal leaks after redoing two hours later (n = 4 for each mannitol dose). 100% of 2-minute and 75% of 5-minute mannitol exposures displayed no focal leaks. (d) Representative images showing the absence of focal leaks after fluorescein re-administration.

Following dosing with mannitol, Lucifer yellow (MW 444 Da) and 10 kDa dextran were introduced into the microvessel to assess barrier function over the subsequent two hours. Mannitol induces dose-dependent changes in permeability (Figure 3-6, A-B). To assess the spatial heterogeneity in Lucifer yellow leakage, we determined the permeabilities in five adjacent segments (820 μm in width) along the length of the microvessels over 2 hours after dosing with mannitol (Figure 3-6, C). Under baseline conditions (no mannitol), the Lucifer yellow permeability along the length of the microvessel varies by less than 68% between five adjacent ROIs. In contrast, there is substantial spatial variation in Lucifer yellow permeability following 2- and 5-minute mannitol doses (on average 228%). This variation is due to the appearance of focal leaks in different segments. The minimum Lucifer yellow permeability across ROIs was $1.59 \pm 0.87 \times 10^{-7}$ cm s^{-1} (control), $8.27 \pm 8.66 \times 10^{-7}$ cm s^{-1} (2-minute mannitol), and $28.8 \pm 18.4 \times 10^{-7}$ cm s^{-1} (5-minute mannitol). 5-minute mannitol doses result in significantly higher Lucifer yellow permeability compared to the control and 2-minute mannitol ($p = 0.004$ and $p = 0.033$, respectively) (Figure 3-6, D). The maximum Lucifer yellow segment permeability (5-minute dose) was about 8×10^{-6} cm s^{-1}, 50-fold higher than the average baseline permeability (control). This increase in permeability represents the upper limit for transiently enhancing drug delivery. Additionally, mannitol dosing resulted in increased variation in the Lucifer yellow permeability, with a 10-fold higher standard deviation compared to the controls.

Increases in Lucifer yellow permeability result from discrete disruptions in barrier function at sites of focal leaks. From analysis of 10 kDa dextran images, we found that focal leaks were located randomly across the entire length of microvessels (Figure 3-6, E). Over the two-hour imaging period immediately after mannitol dosing, control microvessels displayed no focal leaks, 2-minute mannitol microvessels displayed ~3 focal leaks cm^{-1}, and 5-minute mannitol microvessels displayed ~18 focal leaks cm^{-1} (Figure 3-6, F). In subsequent experiments we focus on 5-minute.

72
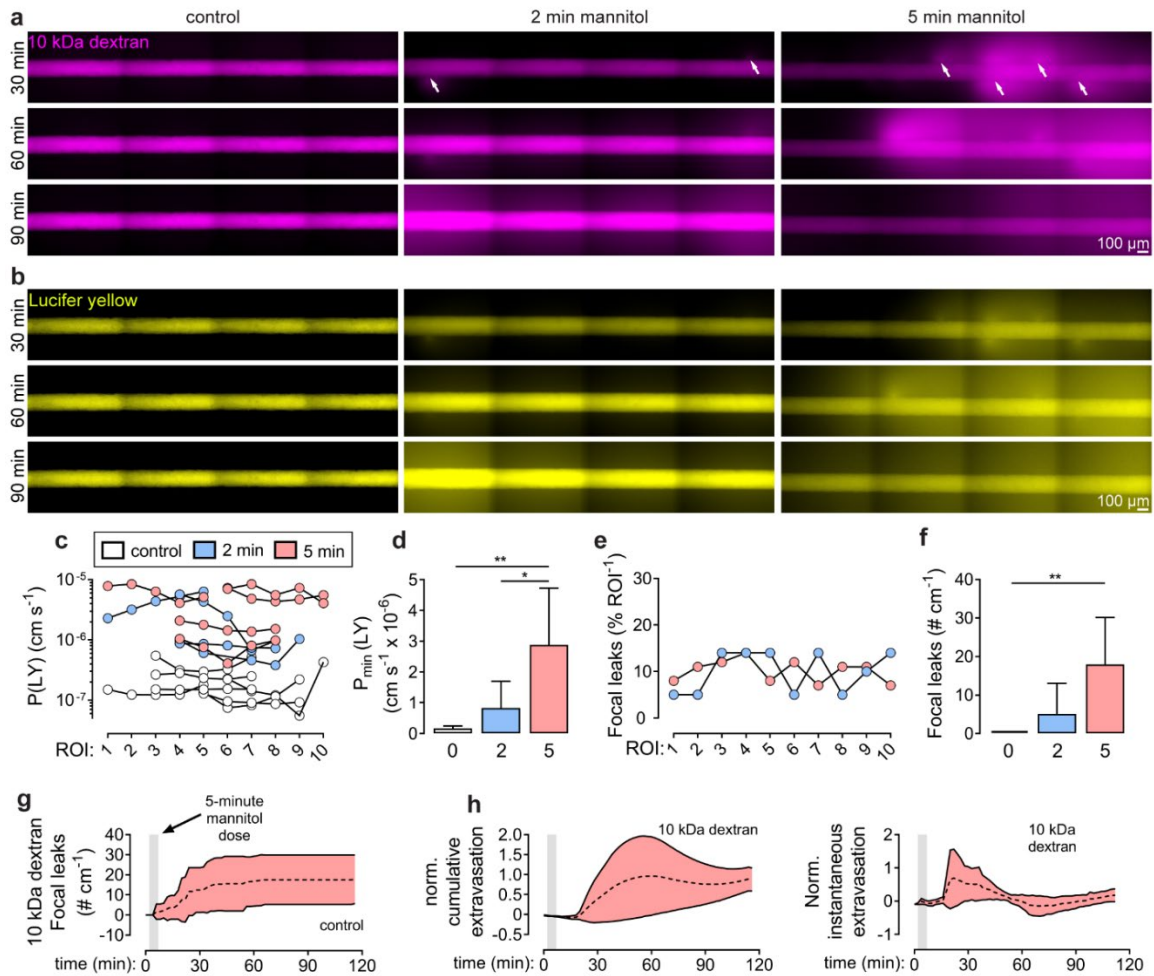
Figure 3-6. Spatially heterogeneous dose-dependent hyperosmotic BBB opening. Representative images at 30, 60, and 90 minutes for (a) 10 kDa dextran and (b) Lucifer yellow under baseline conditions (no mannitol; control) or after 2-minute or 5-minute bolus doses of 1.4 M mannitol. White arrows denote sites of focal leaks. The onset of the mannitol dose begins approximately 2 minutes after injection into the reservoir. Following the mannitol dose, the microvessels are perfused with Lucifer yellow and 10 kDa dextran for 2 hours. (c) The spatial dependence of Lucifer yellow permeability along microvessels (ROI = 825 μm segment) is highly heterogeneous following mannitol exposure. (d) Minimum Lucifer yellow permeability (i.e. the segment with the lowest permeability) for each condition. (e) Focal leaks are uniformly distributed along the length of the microvessels. (f) Focal leak density for each condition. (g) Cumulative 10 kDa dextran focal leaks and (h) normalized cumulative and instantaneous 10 kDa dextran extravasation following a 5-minute mannitol dose. The dotted line represents the mean, while upper and lower solid lines represent the mean ± SD; time is normalized to onset of mannitol dosing at t = 2 minutes. Control (n = 6 microvessels), 2-minute mannitol dose (n = 5 microvessels), and 5-minute mannitol dose (n = 5 microvessels).

73

To determine the time course of BBBO, the number of 10 kDa dextran focal leaks and the penetration of the dye into the matrix were analyzed as a function of time (Figure 3-6, G-H). New focal leaks are not observed after ~60 minutes following onset of a 5-minute mannitol dose. Additionally, extravasation of 10 kDa dextran occurs rapidly; half of all extravasation occurs within 30 minutes following onset of mannitol administration, while no extravasation is observed in control microvessels, as previously reported [181].

To assess microvessel recovery, fluorescein was re-administered after the initial two-hour imaging window for an additional hour. For 2-minute mannitol doses, fluorescein focal leaks were rare during dosing (0.24 ± 0.54 cm^{-1}) and none were observed during fluorescein re-administration (Figure 3-5, C-D), indicating that BBBO is reversed and normal barrier function is re-established. For a 5-minute mannitol dose, while fluorescein focal leaks were observed (5.59 ± 4.35 cm^{-1}) during initial dosing, two hours later focal leaks were rare (0.91 ± 1.82 cm^{-1} over 1 hour) and not observed in most microvessels (75%) (Figure 3-5, C-D). After fluorescein re-administration only 4% of all focal leaks observed during 10 kDa dextran perfusion displayed persistent opening, indicating general reversal of BBBO within two hours of dosing.

3.3.3. Endothelium response to mannitol dosing

From phase contrast images, mannitol dosing induced morphological changes including BMEC shrinkage, thinning of the endothelium, and vacuolation. Upon mannitol dosing, vacuoles formed in the dhBMECs (Figure 3-8, A); their density increased rapidly following the onset of mannitol dosing and reached a plateau thirty minutes later (Figure 3-8, B). The formation of vacuoles was dose-dependent; 2-minute doses resulted in 6.7 ± 2.1 cell^{-1}, while 5-minute doses resulted in significantly higher vacuolation of 10.6 ± 1.9 cell^{-1} ($p = 0.005$) (Figure 3-8, C). Vacuoles were 3.8 ± 1.5 μm in diameter within microvessels exposed to 5-minute mannitol (Figure 3-7, C), excluding the possibility that these structures are lysosomes or endosomes [302].

To gain insight into vacuole localization, microvessels were stained with Calcein AM and DAPI. Interestingly, the cytoplasmic stain Calcien AM was found to distinguish cytoplasm and nucleus from vacuoles. Vacuoles were distributed heterogeneously within dhBMECs including within cell nuclei, within the cytoplasm, or at the boundary of cell nuclei (Figure 3-7, D). Additionally, BMEC nuclei appeared distorted following mannitol treatment, likely due to abrupt changes in cell shape which alters nuclear shape via the actin cytoskeleton [303].
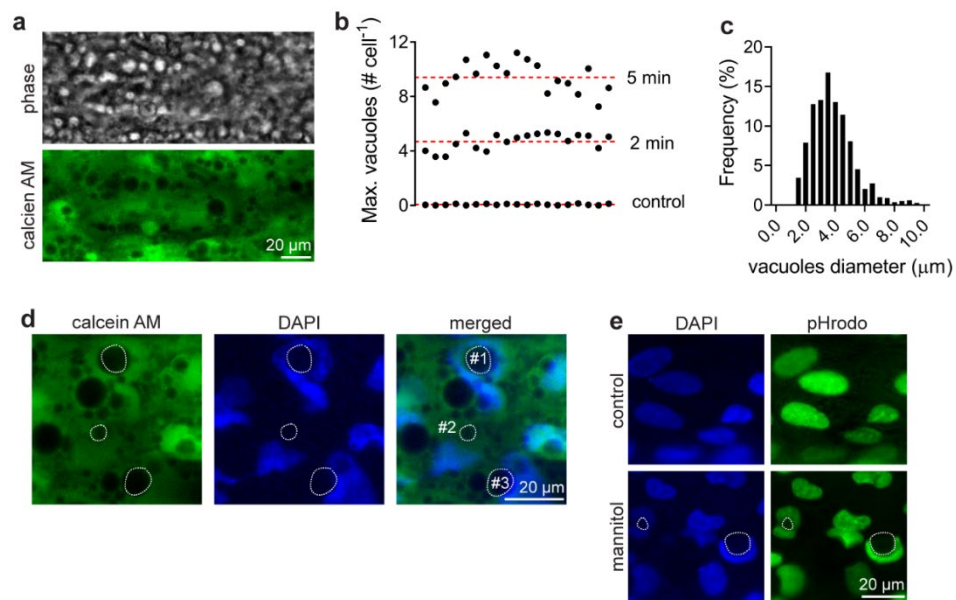
Figure 3-7. Vacuole quantification and characterization. (a) Vacuoles appear as white circles using phase contrast imaging, and are distinct from cytoplasm when stained with Calcein AM. Similar vacuole localization and counts are observed across both methods (representative images shown). (b) Longitudinal analysis of vacuoles for a sample from each condition (x-axis represents > 6 mm). There is not substantial variation in vacuole density along the length of microvessels. (c) Probability distribution of vacuole diameter for 5-minute mannitol exposed microvessels (n = 1127 vacuoles across n = 5 microvessels). The mean vacuole diameter is ~4 μm. (d) Calcein AM and DAPI stains of mannitol-exposed microvessels: vacuoles are not stained with Calcien AM, vacuoles localize internuclear (#1), extranuclear (#2) and in contact with both nucleus and cytoplasm (#3). (e) DAPI and pHrodo Green AM stains of microvessels show that intracellular pH does not appear to localize to vacuoles.

Vacuole formation could occur via multiple mechanisms. Dextran remained excluded from intracellular compartments during and after mannitol dosing (Figure 3-8, D-E), indicating that vacuoles did not form as plasma membrane invaginations. Dextran did not accumulate within the cytoplasm or vacuoles in the BMECs at any point during our experiments, implying that mannitol induces changes in paracellular permeability but not transcellular permeability for compounds with similar or higher molecular weight. To further confirm that mannitol does not induce changes in membrane integrity, microvessels were stained before, or 30 minutes after, a 5-minute mannitol dose. Most BMECs remained viable following mannitol treatment (Calcein AM), and although ethidium homodimer-1 positive cells were slightly more prevalent this was an exceedingly small population (~0.06 %) (Figure 3-8, F-G). Next, we hypothesized that intracellular vacuoles were formed in response to an increase in hydrogen ion concentration (decrease in pH) resulting from the rapid loss of water. However, there was no change in intensity or localization of a pH indicator dye (Figure 3-7, E). The dye was co-localized with DAPI, suggesting that nuclei are the most acidic cell compartment under baseline conditions. However, it is difficult to definitively conclude that vacuoles do not have a lower pH as indicator dyes could be restricted from entry into vacuoles, cleaved in the cytoplasm, or self-quenched at high concentrations. Vacuoles have been observed *in vivo* following mannitol treatment, but were not correlated with BBBO [224].

Vacuole formation reduced the definition of dhBMECs in phase contrast imaging, making it difficult to measure cell loss events [181]. However, from timelapse imaging at the microvessel midplane, loss of dhBMECs from the endothelium is observed following mannitol dosing. Cell loss is dose-dependent, with events observed ~6 or ~2 times more frequently following 5-minute doses, compared to control and 2-minute doses, respectively (Figure 3-8, I). Increased apoptosis has previously been observed following hyperosmotic stress in other cell types [304, 305].
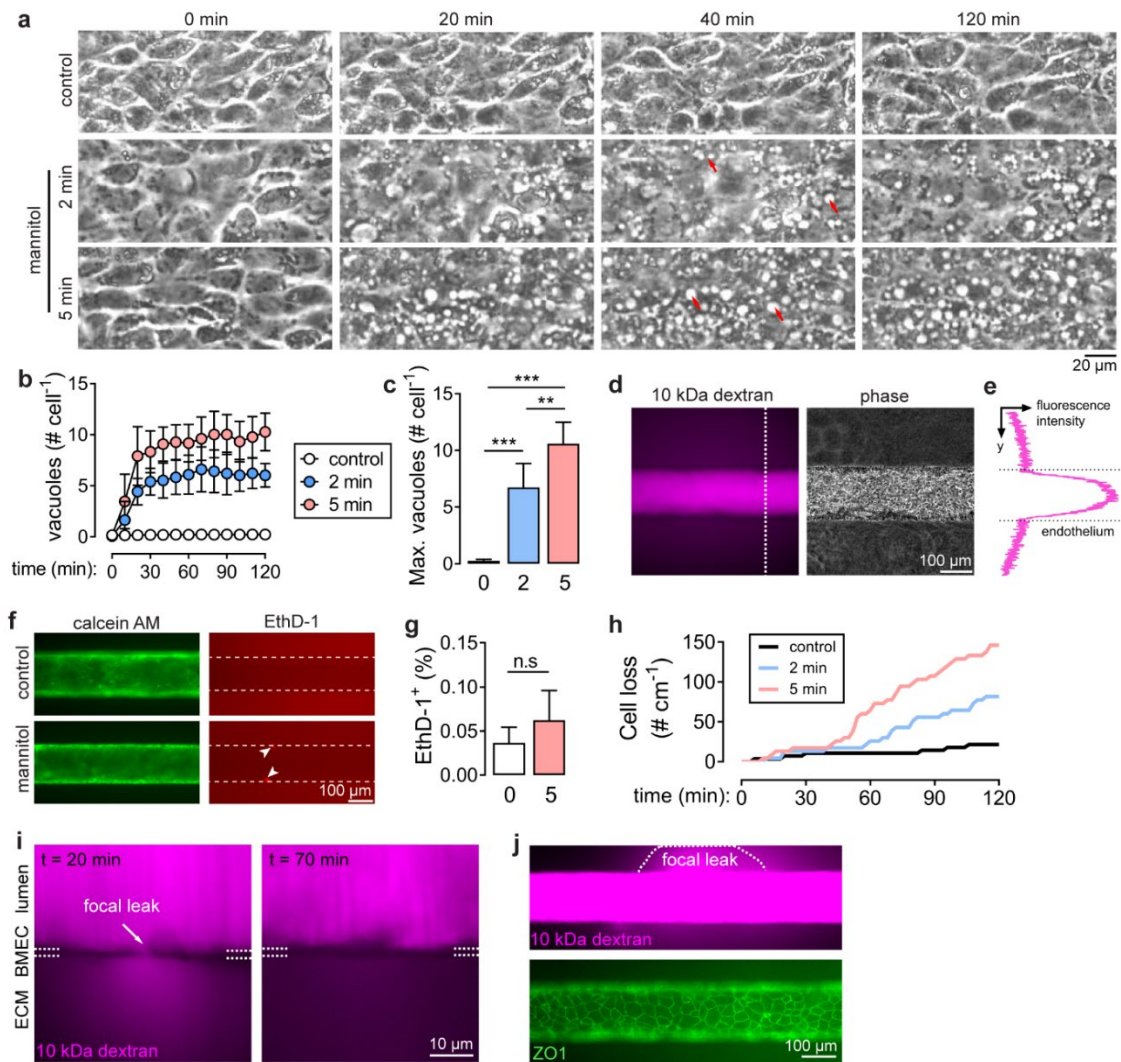
Figure 3-8. Hyperosmotic vacuole formation and tight junction disruption in BBB microvessels. Vacuolation of endothelial cells is dose-dependent: (a) representative time course images of bottom plane of microvessel upon exposure to mannitol. $t = 0$ minutes represents addition of Lucifer yellow and 10 kDa dextran to the upper reservoir, after which the onset of mannitol dose occurred eight or six minutes later for the 2-minute or 5-minute mannitol doses shown, respectively. Red arrows denote examples of vacuoles visible from phase contrast microscopy. (b) Time course of vacuole formation, (c) maximum vacuoles across doses. (d-e) 10 kDa dextran does not accumulate intracellularly following mannitol exposure: (d) representative 10 kDa dextran and phase contrast images, (e) intensity projection of 10 kDa dextran along the dashed white line in subsequent subpanel. (f-g) Live-dead stains (Calcien AM, ethidium homodimer-1) and percentage of ethidium homodimer-1 positive cells before and after mannitol exposure ($n = 3$ microvessels). (h) Cumulative cell loss over two hours for each condition. (i) Confocal imaging at the midplane of a microvessel following a 5-minute mannitol dose shows a focal leak (about $1 - 2$ μm) of 10 kDa dextran across the endothelium. 50 minutes later, the

endothelium is intact showing that the focal leak has closed. (j) Epifluorescence image of a 10 kDa dextran focal leak at the midplane of a microvessel following a 5-minute mannitol dose. Concurrent epifluorescence imaging of tight junctions (ZO1) shows no global changes in TJ localization during hyperosmotic BBB opening.   For quantification of vacuoles and cell loss: control (n = 6 microvessels), 2-minute mannitol dose (n = 5 microvessels), and 5-minute mannitol dose (n = 5 microvessels). All other presented images (d-j) were following a 5-minute mannitol dose.
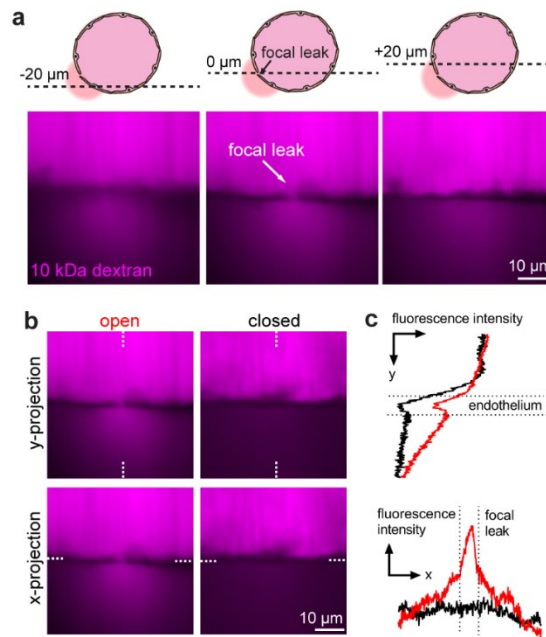
Figure 3-9. Confocal tracing of focal leaks during hyperosmotic BBB opening (5-minute mannitol dose). (a) Focal leaks are visible as a pathway of fluorescence from lumen to ECM that is restricted to a specific z-plane.   20 μm above or below this plane BMECs do not display accumulation of 10 kDa dextran or other obvious disruptions. (b) Time lapse imaging during (open; t = 20 min) and after (closed; t = 70 minutes) focal leakage. (c) Fluorescence intensity along projections of the y- and x-axis, respectively (dashed white lines).   Open focal leaks display elevated 10 kDa dextran fluorescence at the plane of the endothelium.

3.3.4. Characterization of focal leaks

Confocal images during perfusion with 10 kDa dextran shown that the focal leaks are associated

with small gaps (1 – 2 μm) in the endothelium (Figure 3-8, I). Images above and below the z-plane

(0.4 μm thickness) show no leakage (Figure 3-9). There is no evidence of intracellular accumulation

of 10 kDa dextran, indicating that focal leaks are paracellular. Healing of the focal leak is evident

from exclusion of 10 kDa dextran from the endothelium 50 minutes later.

To further investigate the mechanism of tight junction disruption, we performed live-cell imaging of BBB microvessels where the dhBMECs were differentiated from iPSCs with fluorescently labeled zona occludens-1 (ZO1). Following mannitol administration the global tight junction structure is not perturbed (Figure 3-8, J). Direct visualization of TJ disruption at the site of a focal leak is not possible due to limited z-resolution at the microvessel midplane where the focal leaks are visualized. However, from analysis of the images at the top and bottom of the microvessels, we can show that there is no disruption in ZO1 within about 125 μm (~5 cell lengths) of a focal leak (Figure 3-10).
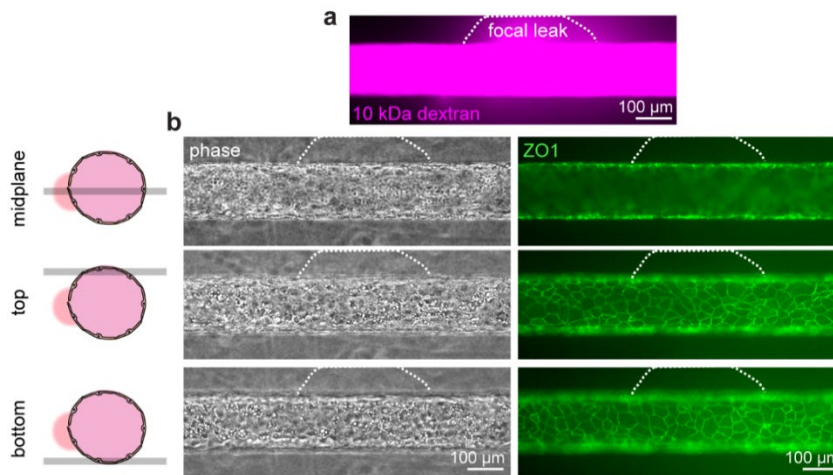
Figure 3-10. Confocal tracing of focal leaks and tight junctions during hyperosmotic BBB opening. (a) 5-minute mannitol doses result in focal leaks visible by 10 kDa dextran leakage at the microvessel midplane. (b) Phase contrast and zona occludens-1 (ZO1) fluorescence images were acquired at the midplane and microvessel poles, during focal leakage. Visualization of TJ disruption is challenging at the microvessel midplane, while at planes above and below the focal leak, tight junctions appear intact and well-localized.

3.3.5. bFGF pre-treatment attenuates BBB opening

To assess the role of bFGF in modulating BBB function, microvessels were treated with 20 ng mL^{-1} bFGF during the initial 24 hours after cell seeding (Figure 3-11). Control microvessels (no

mannitol) pre-treated with bFGF displayed similar Lucifer yellow permeability on day 0 compared to control microvessels (p = 0.449), although there was an increase in the number of vacuoles (p = 0.003) (Figure 3-11, B). Pre-treatment with bFGF increases the transendothelial electrical resistance (TEER) of iPSC-derived BMEC monolayers within 2D transwells (p = 0.021, Figure 3-12, A). However, increased TEER was not associated with increases in endothelial cell density (p = 0.750), total tight junction fluorescence intensity (p = 0.755), or junctional localization (Figure 3-12, B-D). Microvessels pre-treated with bFGF and then exposed to a 5-minute mannitol dose (on day 0) were less susceptible to BBBO (Figure 3-11, C). The minimum Lucifer yellow permeability and the presence of focal leaks were reduced with bFGF pre-treatment (p = 0.029 and 0.036, respectively) compared to control microvessels (Figure 3-11, D). For example, following a 5-minute mannitol dose, the minimum permeability was 3.02 ± 2.14 x 10^{-7} cm s^{-1}, 10-fold lower than with no bFGF treatment. Similarly, the number of focal leaks decreased from 18 ± 12 cm^{-1} to 1.8 ± 1.6 cm^{-1} following pre-treatment with bFGF. The maximum number of vacuoles per cell was slightly higher with bFGF pre-treatment, although not statistically significant (p = 0.113) (Figure 3-11, D).

However, microvessels pretreated with bFGF and exposed to a 10-minute mannitol dose displayed BBBO (Figure 3-13).The minimum Lucifer yellow permeability was higher than bFGF-pretreated microvessels not exposed to mannitol (p = 0.0459), and similar to that of 2-minute mannitol doses in control microvessels; both displayed an average minimum Lucifer yellow permeability of approximately 7 - 8 x 10^{-7} cm s^{-1}, about 5-fold higher than the control. 10 kDa dextran focal leaks were observed with 10-minute mannitol dose (9.3 ± 8.3 cm^{-1}), although not significantly greater than controls (no bFGF). The concentration of vacuoles increased compared to controls (p = 0.0002) but was similar to those observed with 5-minute mannitol treatment, suggesting that vacuolation may plateau at high doses. The permeability of microvessels pre-treated with bFGF
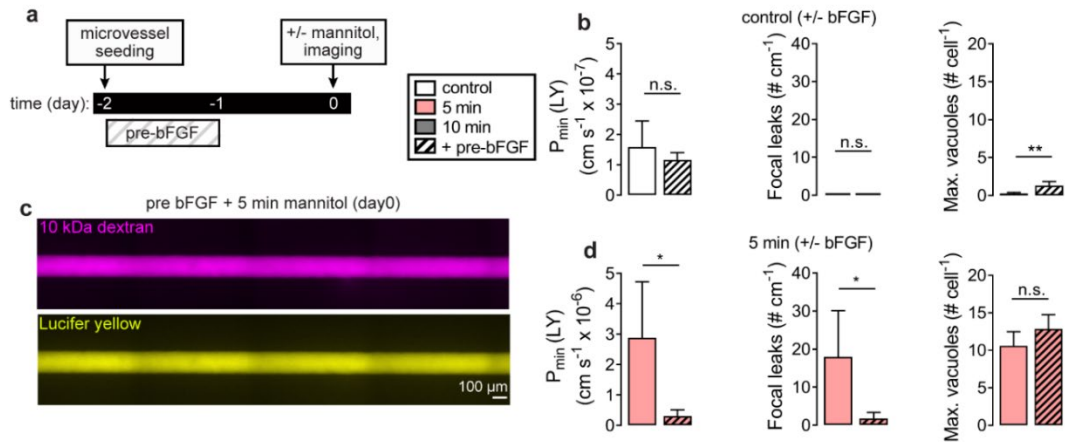
Figure 3-11. Basic fibroblast growth factor (bFGF) pre-treatment mitigates BBB opening. (a) Summary of 20 ng mL^{-1} bFGF treatment. (b) Comparison of the minimum Lucifer yellow permeability, the number of focal leaks, and the number of vacuoles following a 5-minute mannitol dose with (n = 3) and without bFGF pre-treatment with (n = 6). (c) Representative images of 10 kDa dextran and Lucifer yellow in bFGF pre-treated microvessels following a 5-minute mannitol dose showing no focal leaks. (d) Comparison of the minimum Lucifer yellow permeability, the number of focal leaks, and the number of vacuoles following a 5-minute mannitol dose with (n = 4) and without bFGF pre-treatment with (n = 5).
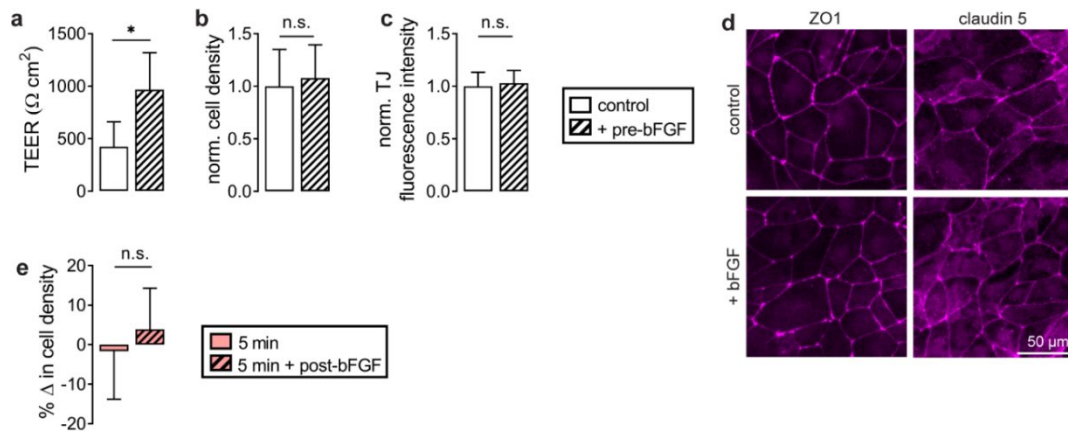
Figure 3-12. Influence of bFGF pre- and post-treatment. (a) Basic fibroblast growth factor (bFGF) pre-treatment increased transendothelial electrical resistance (TEER) of dhBMEC monolayers in a transwell on day 0, in the absence of mannitol dosing (n = 5). (b) bFGF pre-treatment had no effect on cell density (n = 4). (c) Analysis of zona occludens-1 and claudin-5 in immunofluorescence images showed no effect on junction intensity in immunofluorescence images (n = 4). (d) Immunofluorescence images of zona occludens-1 and claudin-5 in two-dimensional monolayers on day 0 display no clear difference with and without bFGF pre-treatment. (e) Cell density obtained from analysis of phase contrast images of microvessels 2 days following a 5-minute mannitol dose (n = 3). bFGF post-treatment (continuous perfusion beginning 2 hours following mannitol treatment) resulted in a small but non-significant increase in the cell density.
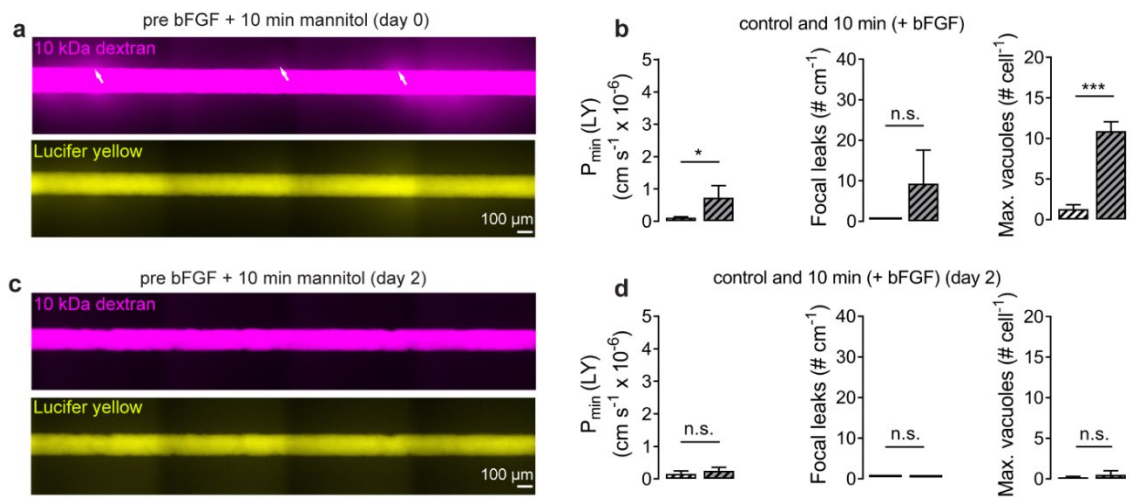
Figure 3-13. Basic fibroblast growth factor (bFGF) pre-treatment mitigates BBB opening, requiring a longer dose to induce opening. (a) Representative images of 10 kDa dextran and Lucifer yellow in bFGF pre-treated microvessels exposed to 10-minute mannitol, focal leaks are denoted with white arrows. (b) Comparison of minimum Lucifer yellow permeability, focal leaks and vacuoles between microvessels pre-treated with bFGF exposed to no mannitol (n = 3) or 10-minute mannitol (n = 3). (c) Representative images of 10 kDa dextran and Lucifer yellow in bFGF pre-treated microvessels exposed to 10-minute mannitol 48 hours after mannitol exposure (day 2), focal leaks are not observed. (d) Comparison of minimum Lucifer yellow permeability, focal leaks and vacuoles between microvessels pre-treated with bFGF exposed to no mannitol (n = 3) or 10-minute mannitol (n = 3) on day 2; BBB opening is reversible.

and exposed to 10-minute mannitol doses returned to baseline levels within 48 hours (by day 2). On day 2, the minimum Lucifer yellow permeability, the number of focal leaks, and the vacuole density were indistinguishable from baseline bFGF pre-treated microvessels (p > 0.05).

3.3.6. bFGF post-treatment enhances BBB stability 48 hours after mannitol dosing

Endogenous bFGF circulates in human blood at concentrations in serum below ~10 pg mL^{-1} [306]. To aid in recovery and repair following injuries, administration of exogenous bFGF or other growth factors has been explored [307-310]. Treatment with hyperosmotic agents perturbs endothelial homeostasis and causes significant stress to BMECs. Previously, we showed that focal leaks two hours following a 5-minute mannitol dose were rare events, indicating recovery of barrier function.

To investigate the long-term response to mannitol stress, we investigated barrier function 48 hours following treatment with and without bFGF continuously administered starting 2 hours after mannitol dosing (Figure 3-14, A). Without bFGF post-treatment, BBB microvessels displayed variable barrier function 48 hours following a 5-minute mannitol dose (Figure 3-14, B). The minimum Lucifer yellow permeability decreased 48 hours following dosing (day 2) and was approximately three times higher than the baseline control although not statistically significant (p = 0.360) (Figure 3-14, C). While widespread disruption of the monolayer was not observed 48 hours following dosing, some microvessels did display leakage of 10 kDa dextran indicating instability of barrier function (Figure 3-14, D). With bFGF post-treatment, all microvessels displayed stable barrier function following hyperosmotic BBBO (Figure 3-14, F). The minimum Lucifer yellow permeability 48 hours following 5-minute mannitol dosing was $3.42 \pm 1.74 \times 10^{-7}$ cm s^{-1}, approaching physiological values, and similar to controls (no mannitol, no bFGF) (p = 0.132) (Figure 3-14, G). In addition, with bFGF post-treatment no focal leaks were observed, representing a significant decrease from the response immediately after mannitol dosing (p = 0.047) (Figure 3-14, H). The recovery of dhBMEC vacuolation was not dependent on bFGF post-treatment; under both conditions vacuolation decreased by ~10-fold 48 hours following 5-minute mannitol dosing (p = 0.007 and 0.013, for control and bFGF post-treatment microvessels respectively) (Figure 3-14, E, I). Administration of bFGF after mannitol dosing was associated with a small, non-significant increase in cell density, possibility due to increased BMEC proliferation (p = 0.326, Figure 3-12, E)
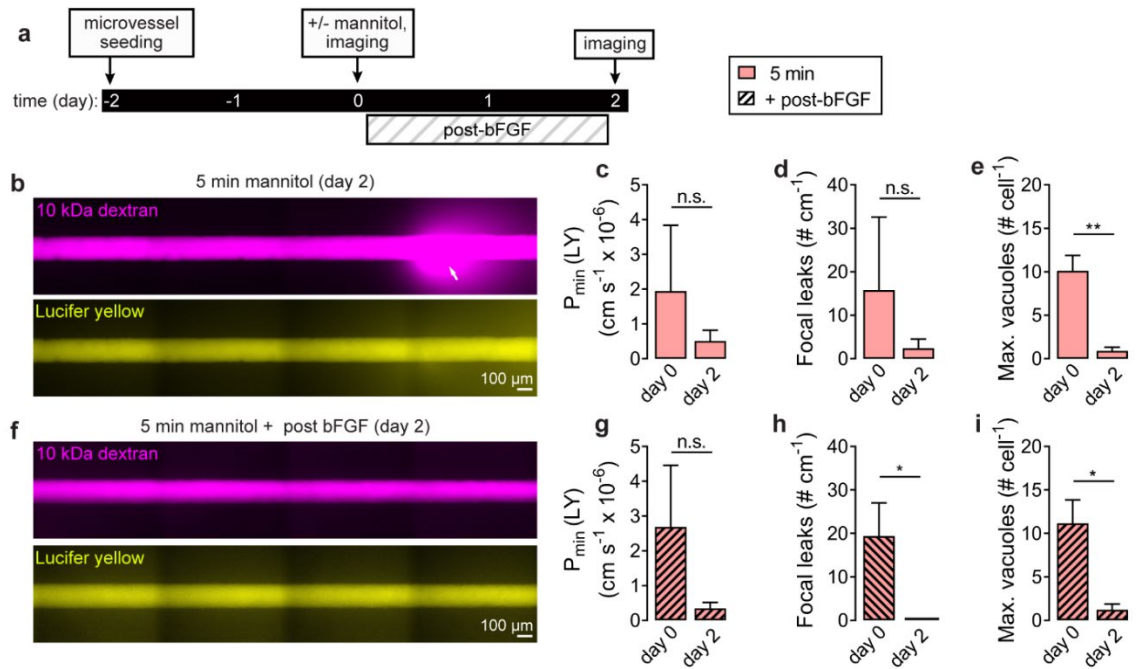
Figure 3-14. bFGF post-treatment promotes BBB repair following hyperosmotic opening. (a) Microvessels were continuously perfused with 20 ng mL^{-1} bFGF following a 5-minute mannitol dose. (b) Representative images of 10 kDa dextran and Lucifer yellow on day 2 following a 5-minute mannitol. Focal leaks are denoted by white arrows. (c-e) Comparison of minimum Lucifer yellow permeability, the number of focal leaks, and the number of vacuoles after a 5-minute mannitol dose, and on day 2 following dosing (n = 3). (f) Representative images of 10 kDa dextran and Lucifer yellow on day 2 following a 5-minute mannitol dose in bFGF post-treated microvessels. No focal leaks are observed. (g-i) Comparison of minimum Lucifer yellow, the number of focal leaks, and the number of vacuoles after a 5-minute mannitol dose, and on day 2 following dosing in microvessels post-treated with bFGF (n = 3).

3.4. Discussion

MRI assessment of BBB status in animal models does not provide sufficient spatial resolution for studying the mechanisms of BBBO. Here, we utilize time lapse imaging to visualize hyperosmotic BBBO in a tissue-engineered microvessel model with human stem cell-derived BMECs [181, 198]. In the current model for transient hyperosmotic BBBO, removal of water induces vasodilation, and above a critical threshold (related to the product of osmolarity and injection duration), vasodilation causes sufficient mechanical stress to disrupt TJs, resulting in increased paracellular transport [259,

287, 288]. This model usually assumes a time-dependent but spatially homogeneous increase in permeability [259].

3.4.1. Mannitol induces spatially heterogeneous increases in paracellular permeability

The key observations from imaging mannitol-induced BBBO in microvessels are: (1) mannitol causes transient focal leaks that result in a significant increase in the overall permeability, (2) the focal leaks occur at small (1 – 2 μm) sub-cellular disruptions in the endothelium, (3) the global TJ network is unaffected by mannitol, and (4) the increase in permeability is due solely to paracellular transport. Together these results suggest that focal leaks are formed by disruption of TJs between adjacent cells.

A 1 cm long, 150 μm diameter microvessel consists of ~8,000 cells (average cell area is 625 μm^2), with each cell having ~6 neighbors [181], corresponding to a total of 48,000 unique cell-cell junctions. Therefore, the observation of 18 focal leaks (assuming that focal leaks occur when a single cell-cell junction is disrupted) in response to a 5-minute mannitol dose corresponds to a failure of 0.04% of TJs or ~0.25% of all dhBMECs. This suggests that there is a distribution of TJ strengths and it is the weakest TJs that are the first to be disrupted during mannitol dosing. Consistent with this hypothesis, spatial heterogeneity in endothelial barrier function was reported in 2D monolayers in response to histamine treatment utilizing total internal reflection fluorescence (TIRF) microscopy [311].

Under baseline conditions, the permeability of 10 kDa dextran is below the detection limit and there is no appreciable intracellular accumulation indicating negligible paracellular and transcellular transport. Following mannitol dosing, the permeability of 10 kDa dextran increases via focal leaks but there is no intracellular accumulation or widespread BMEC membrane permeabilization (i.e. low ethidium homodimer-1 fraction), consistent with negligible transcellular transport. Despite the low incidence of TJ failure, dramatic increases in permeability are still observed. For example,

the minimum Lucifer yellow segment permeability increases 20-fold over 20 minutes following a 5-minute mannitol dose. This increase matches previous measurements of baseline Lucifer yellow permeability within human umbilical vein endothelial cell microvessels ($\sim$4 x 10^{-6} cm s^{-1}) [181]. These results suggest that transient BBBO following mannitol dosing is associated with a small number of focal leaks that are responsible for rapid extravasation of solutes into the surrounding matrix. We note that mechanisms of BBBO and response to mannitol may be different in other conditions, such as trauma and stroke [1, 312, 313].

3.4.2. Timeline of hyperosmotic BBB opening, drug delivery and recovery

To further elucidate the timeline of opening and recovery, we normalized experimental metrics to the onset of a 5-minute mannitol dose (Figure 3-16). Fluorescein focal leaks appear during mannitol dosing, suggesting that changes in BBB permeability can occur almost instantaneously, matching observations from dynamic T1 MRI. The emergence of dhBMEC vacuolation and the decrease in microvessel diameter show delayed responses compared to focal leaks, with half-times of 6.5 and 12 minutes, respectively, after dose onset. This suggests that vacuolation and changes in microvessel diameter are not direct mediators of BBBO.

Drug delivery, based on extravasation of 10 kDa dextran, is proportional to focal leak density and persistence. The cumulative number of focal leaks for 5-minute mannitol doses display a half-time of 20 minutes after dose onset. The extravasation of 10 kDa dextran occurs over a longer period (τ = 30 minutes), due to the persistence of focal leaks. The persistence of focal leaks following a 5-minute mannitol dose spanned an order of magnitude, from less than 2 minutes to more than 20 minutes (Figure 3-15). Determining the persistence time was complicated due to impingement of dextran from neighboring focal leaks. Cell loss is significantly delayed from the onset of focal leaks and leakage of fluorescent probes into the matrix (τ = 60 minutes), supporting the hypothesis that focal leaks are associated with TJ disruption and not cell loss from the endothelium
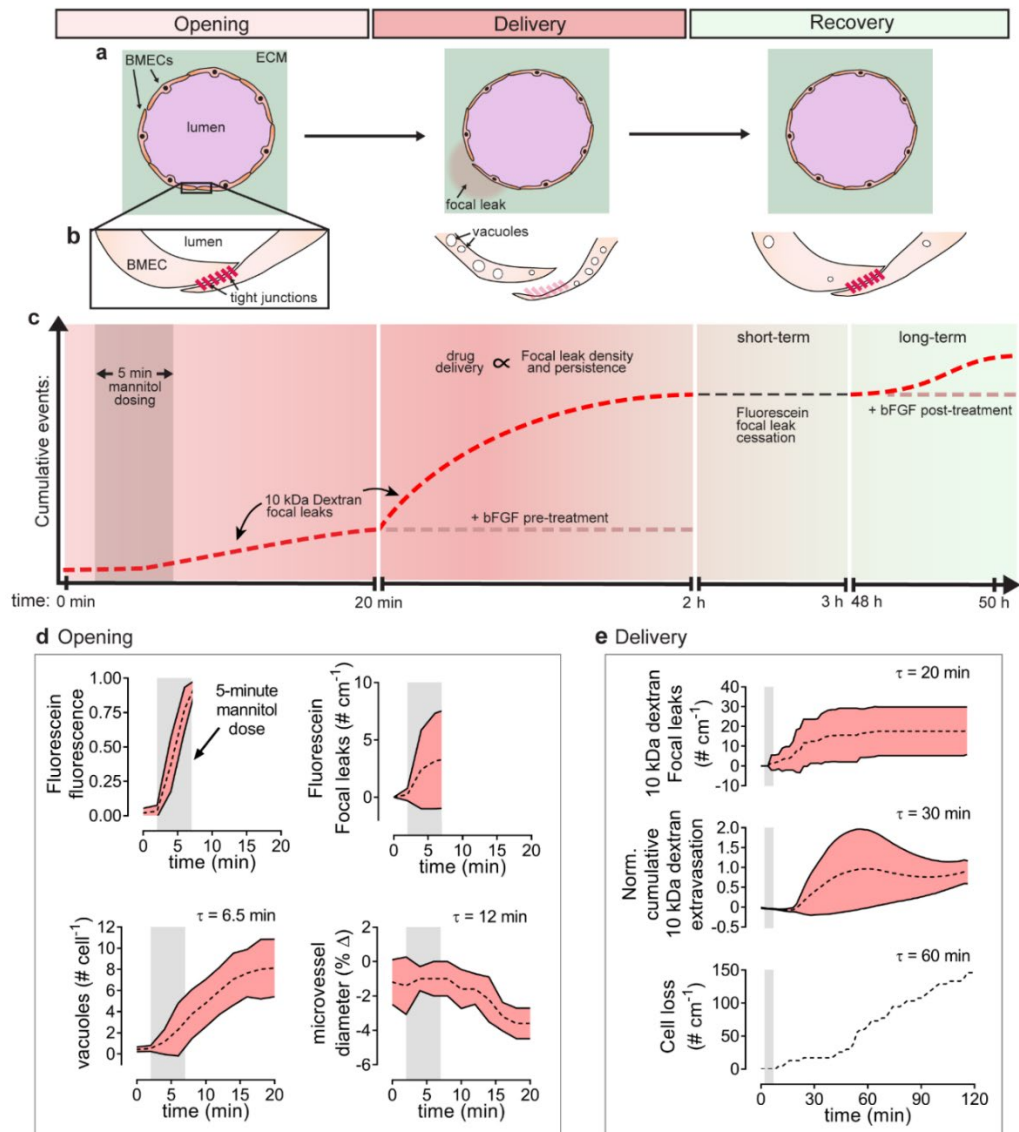
Figure 3-15. Mechanisms of hyperosmotic BBB opening, drug delivery, and recovery. Cross-sectional view of BBB microvessels during and after mannitol dosing, with (b) zoom-in on tight junctions (TJs) between adjacent BMECs. (c) Mechanistic timeline: fluorescein focal leaks first emerge during dosing followed by vacuoles and 10 kDa dextran focal leaks after dosing. Drug delivery is proportional to focal leak density and persistence. Short-term recovery is visible as cessation of fluorescein focal leaks, while in the long-term mannitol can compromise stability. TJ strengthening (bFGF pre-treatment) mitigates BBB opening, while BMEC proliferation (bFGF post-treatment) promotes BBB opening. (d) Time course of events over the initial 20 minutes of imaging and (e) over two hours of imaging following a 5-minute mannitol dose (n = 5 microvessels). All events are normalized to the 5-minute dose in which fluorescein fluorescence peaks, corresponding to the vertical grey bar from 2 to 7 minutes. Half-times (τ) are reported with respect to onset of dose (t = 2 minutes). The dotted line represents the mean, while upper and lower solid lines represent the mean plus or minus one standard deviation.

(Figure 3 16, E). Over two hours following a 5-minute dose ~2% of all BMECs are lost from the microvessel, likely due to induced apoptosis from hyperosmotic stress [301, 302].10 kDa dextran extravasation into the ECM (a proxy for drug delivery into the brain) is dramatically increased by mannitol dosing. In contrast, in the absence of mannitol dosing, there is no detectable leakage of dextran from the microvessel. Techniques to modulate transcellular permeability, including efflux pump inhibition, have a more modest potential to alter CNS drug penetration. For example, p-glycoprotein inhibition *in vivo* [252] and *in vitro* [181] modulates efflux pump substrate permeability by only 2- to 3-fold. Thus, hyperosmotic methods for BBBO have a distinct advantage for delivery of large molecular weight compounds that are not efflux substrates.
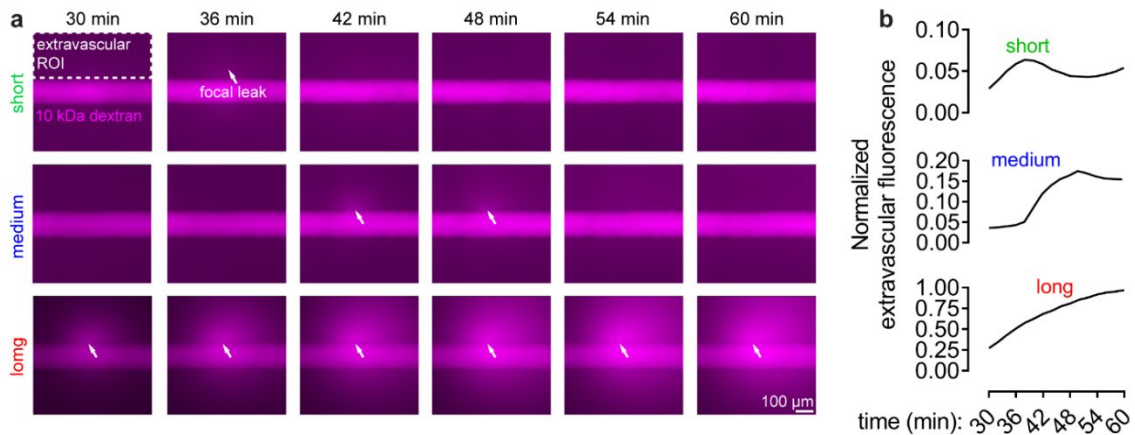
Figure 3-16. Persistence of 10 kDa dextran focal leaks. (a) For a representative 5-minute mannitol exposed microvessel, focal leaks of various persistence are shown. White arrows denote an active focal leak characterized by increasing extravascular fluorescence. (b) Normalized extravascular fluorescence (within the dotted ROI drawn in sub-panel a) is plotted over 30 minutes. Duration of extravascular fluorescence increase corresponds to focal leaks of short, medium and long persistence. t = 0 minutes represents addition of Lucifer yellow and 10 kDa dextran to the upper reservoir, after which the onset of mannitol dose occurred two minutes later for the 5-minute mannitol dose shown.

Based on the time-dependent responses, we propose that mannitol induces shrinkage of BMECs which increases the tensile stress on TJs (Figure 3-16, Figure 3-17). Cell shrinkage continues to a point where TJs between adjacent cells are compromised. Assuming a distribution of TJ strength, the weakest TJs fail first resulting in transient focal leaks and a local increase in paracellular permeability. Microvessels exposed to low doses of mannitol do not reliably open due to insufficient cell volume loss, while bFGF pre-treatment strengthens TJs preventing BBBO. Long term failure of barrier function is likely due to accumulated hyperosmotic stress on BMECs, which can be recovered by promoting cell proliferation with bFGF post-treatment.
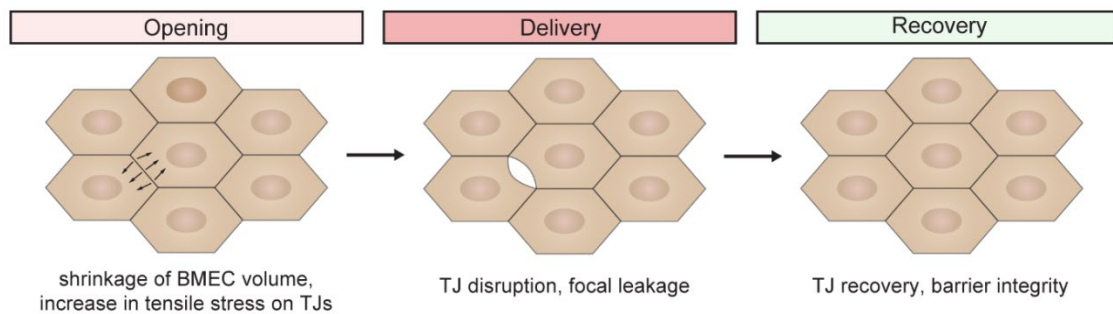
Figure 3-17. Proposed mechanism of hyperosmotic BBB opening, drug delivery, and recovery. Mannitol induces cell shrinkage which increases tensile stress on tight junctions (TJs). Opening occurs as a function of the magnitude of cell shrinkage and TJ strength (i.e. insufficient cell volume loss or strengthened TJs prevent BBB opening). Paracellular permeability increases due to focal leakage at the site of TJ disruption. Once TJs are re-established, barrier integrity is resumed.

3.4.3.Baseline permeability is not a predictor of susceptibility to BBB opening

Pre-treatment with bFGF does not alter baseline permeability of microvessels but does increases the mannitol dose required to induce BBBO. This suggests that bFGF shifts the distribution of TJ strengths so that longer doses are required to exert sufficient stress on the weakest TJs to initiate opening. In the context of the brain, it is possible that some regions are more resistant to opening due differences in TJ expression, even though the permeability to small molecules is independent

of location. For example, the cerebral cortex does not exhibit significant BBBO following hyperosmotic therapy in mice [295]. It is not well understood if this is due to heterogeneity of TJ strength [230] or hemodynamics and the mannitol distribution compared to other brain regions. *In vitro,* treatment with bFGF upregulates primary hBMECs TJ proteins [308]. Additionally, while bFGF is not required to achieve physiological barrier function (low permeability), as shown here and previously [181], its removal during seeding of transwells with dhBMECs reduces transendothelial electrical resistance (TEER). Thus, bFGF is likely able to shift the distribution of TJ strengths so that a 10-minute mannitol dose is required to induce disruption. Importantly, these results imply that the culture conditions of *in vitro* BBB models impact interpretation of BBBO efficacy.

3.4.4. Long-term recovery to BBB opening is promoted by bFGF

Fluorescein focal leaks were not observed two hours after a 2-minute mannitol dose and were uncommon (25% of microvessels) following a 5-minute dose, indicating that barrier function has largely recovered within two hours. However, the hyperosmotic stress on dhBMECs resulted in inconsistent barrier function 48 hours following dosing in the absence of exogenous growth factors. Focal leaks and increased permeabilities were observed 48 hours after 5-minute mannitol doses. In previous work, BBB microvessels not exposed to mannitol displayed no focal leaks and stable permeability over six days after seeding [181]. Post-treatment of microvessels with bFGF promoted recovery from hyperosmotic stress in the 48 hours following dosing. A possible explanation for the influence of bFGF is that it promotes cell growth, and increases cell density, thereby reducing the stress on the dhBMECs in response to hyperosmotic stress. Although, we measure a small increase in cell density, it is not significant ($p = 0.326$, Figure 3-12, E). However, only a small increase in cell density may be sufficient to reduce the stress on TJs.

In vivo studies of the duration of osmotic BBBO have reported conflicting timelines [265, 294, 314]. These inconsistencies likely result from differences in species, anesthetic agents, infusion rates, doses, tracers, and imaging techniques, among other factors. Across 38 human subjects, good-to-excellent BBB disruption was obtained in ~75% of patients, while the remaining 25% displayed poor-to-moderate disruption [294]. This study reported that the BBB remained open for at least 40 minutes after osmotic exposure and returned to baseline after six to eight hours following induction of good-to-excellent BBBO [294]. We find that BBBO is generally reversible within two hours. Additionally, our results suggest that mannitol treatment induces stress in dhBMECs that, for larger doses, manifests two days later as disruptions in barrier function, but which can be recovered by bFGF treatment. bFGF exerts a protective effect on BBB damage following traumatic brain injury and intracerebral hemorrhage in mice [308, 309]. While bFGF treatment is not required to reverse hyperosmotic therapies *in vivo*, supporting cells (i.e. pericytes [315] or astrocytes [316]) may play a role in recovery.

3.4.5. Model advantages and limitations

Our tissue-engineered microvessel model mimics key components of the human BBB, including physiological permeability, cylindrical geometry, cell-matrix interactions, and shear stress.[26] Microvessels formed from dhBMECs exhibit low permeability of small molecules, consistent with physiological BBB function in animal models [225, 317]. Previous *in vitro* studies have relied on modeling hyperosmotic BBBO within two-dimensional microfluidic systems [318] or hollow-fiber based platforms [267, 319], where direct visualization of cell behavior is challenging. There are two main limitations to our model for studying hyperosmotic BBBO. (1) Microvessels are comprised of only BMECs. Recent evidence suggests that other cellular components of the BBB are not necessary to maintain physiological permeability *in vitro* [26, 320], but may play a critical role in the response to injury or stress as observed *in vivo* [321, 322], which is not captured here.

(2) Microvessels mimic features of brain post-capillary venules but are larger than brain capillaries (typically 8 - 10 μm). The influence of diameter on BBBO susceptibility is unknown. These differences may explain discrepancies in mannitol doses required to initiate BBB opening.

Chapter 4. Three-dimensional induced pluripotent stem-cell models of human brain angiogenesis

A version of this chapter is published in Microvascular Research 132 (2020) [323]

Raleigh M. Linville,[1,2] Diego Arevalo,[1,2] Joanna C. Maressa,[1,3] Nan Zhao,[1] and Peter C. Searson[1,2,3]

[1] Institute for Nanobiotechnology, Johns Hopkins University, Baltimore, MD

[2] Department of Biomedical Engineering, Johns Hopkins University, Baltimore, MD

[3] Department of Materials Science and Engineering, Johns Hopkins University, Baltimore, MD

4.1. Introduction

Brain angiogenesis is a multistage process by which new capillaries sprout from existing blood vessels. The culmination of brain angiogenesis during development results in a 600 km network of capillaries forming the blood-brain barrier (BBB) [4]. Brain microvascular endothelial cells (BMECs), which form the interface between the vascular system and the brain parenchyma, regulate transport into the brain via expression of tight junctions (TJs), efflux pumps, and nutrient transporters [6, 26]. The ability to study brain angiogenesis *in vitro* has been limited by a lack of 3D models and an appropriate source of brain microvascular endothelial cells. Consequently, previous studies have relied on two-dimensional assays such as the Matrigel tube assay and cord-forming assays, or utilize primary / immortalized cells, which display an incomplete BBB phenotype [324-326].

To enable imaging of angiogenesis in 3D, we have adapted the fibrin bead angiogenesis assay [327], forming a confluent monolayer of iPSC-derived brain microvascular endothelial cells

(dhBMECs) on microbeads (BBB beads). The beads are then embedded in a collagen I hydrogel, which mimics the native stiffness of brain parenchyma [328]. We then explore how changes in the chemical and extracellular matrix microenvironment influence angiogenesis. We report on the influence of pro-angiogenic cues including vascular endothelial growth factor (VEGF) [70], wnt7a/b [71], and basement membrane [329]. In addition, to mimic pathological angiogenesis in response to oxidative stress, we report on the dose-dependent effects of hydrogen peroxide.

DhBMECs have emerged as an attractive cell source for BBB models as: (1) species differences mean that animal models do not always recapitulate human disease [185, 330], (2) reliable and diverse protocols have been developed to differentiate BMECs [194, 196, 197], and (3) patient-specific and CRISPR gene-edited iPSCs are available for controlled studies on how genetic mutations impact cell phenotype [137, 331, 332]. Additionally, dhBMECs recapitulate key aspects of BBB phenotype including high transendothelial electrical resistance, restriction of paracellular permeability, and efflux activity [26] [333]. Primary and immortalized BMECs, which de-differentiate during *in vitro* culture [334], are often deficient in these characteristics and are not easily scalable for isogenic or patient-specific studies [335].

We also apply our results from the BBB bead angiogenesis assay to improve design of tissue-engineered hierarchical BBB models. Existing 3D models of brain angiogenesis based on self-organization approaches [180, 209, 336] fail to recapitulate the hierarchy of the human BBB, consisting of capillaries fed by an input arteriole and output venule. Engineering hierarchal microvascular models is limited by the spatial and temporal resolution of current techniques [336-339]. Our lab has demonstrated a hybrid approach relying on both templating and angiogenesis to form hierarchical microvascular networks using human umbilical vein endothelial cells (HUVECs) [340]. Here, after formation of microvessels resembling post-capillary venules (PCVs) by seeding dhBMECs into channels patterned within ECM [300], we apply optimized angiogenic factors to

promote sprouting and anastomosis between adjacent microvessel to recapitulate a key aspect of human BBB function, low solute permeability. Our three-dimensional models provide a diverse toolbox for studies of brain angiogenesis.

4.2. Materials and methods

4.2.1. Cell culture

Brain microvascular endothelial cells (BMECs) were differentiated from hiPSCs similar to published protocols [196, 300]. The WTC iPSC line [299] with red fluorescent protein-tagged plasma membrane (Allen Cell Institute) was used to facilitate live-cell monitoring of angiogenesis. WTC iPSCs were plated at 10,000 cells cm^{-2} on Matrigel-coated plates and grown for two days in mTESR1 (StemCell Technologies) to approximately 25% confluency, with 10 μM ROCK inhibitor Y27632 (RI; ATCC) supplemented for the initial 24 hours. Subsequent six-day treatment with unconditioned media without bFGF (UM/F-): DMEM/F12 (Life Technologies) supplemented with 20% knockout serum replacement (Life Technologies), 1% non-essential amino acids (Life Technologies), 0.5% GlutaMAX (Life Technologies) and 0.836 μM beta-mercaptoethanol (Life Technologies), and two-day treatment with RA media: human endothelial cell serum-free media (Life Technologies) supplemented with 1% human platelet poor derived serum (Sigma), 2 ng mL^{-1} bFGF (R&D Systems), and 10 μM all-trans retinoic acid (RA; Sigma) produces dhBMECs. Differentiations were conducted over a ten-passage window on six-well plates using media volumes of 1 mL and daily media switches. Transendothelial electrical resistance (TEER) measurements were used to confirm the quality of differentiations as previously reported [196]; the average TEER for WTC-RFP cells after 48 hours was ~2,500 Ω cm^2.

VeraVec HUVEC-TURBO-GFP cells (HUVECs; Angiocrine Bioscience) were used as a non-brain specific endothelial cell control. HUVECs were grown in "HUVEC media": MCDB 131 (Caisson) supplemented with 10% fetal bovine serum (Sigma), 1% pen-strep-glut (Thermo Fisher), 1 μg mL^{-}

^{1} hydrocortisone (Sigma), 10 µg mL^{-1} heparin (Sigma), 25 µg mL^{-1} endothelial cell growth supplement (Thermo Fisher), and 0.2 mM ascorbic acid 2-phosphate (Sigma). HUVECs were used until passage 7 and routinely passed using TrypLE Express (Life Technologies).

4.2.2. Forming endothelial monolayers on microbeads

Assay protocols were adapted from those developed for primary endothelial cells [327]. 150 µm diameter Cytodex™ 3 microcarrier beads (GE Healthcare) were prepared according to manufacturer recommendations. Beads were coated overnight with 50 µg mL^{-1} human placental collagen IV (Sigma) and 25 µg mL^{-1} fibronectin from human plasma (Sigma). dhBMECs were singularized using 30 minute StemPro accutase (ThermoFisher) treatment and incubated at a ratio of 1000:1 (dhBMECs:beads) for two hours under gentle agitation every 30 minutes. "Bead seeding media" was comprised of human endothelial cell serum-free media (Life Technologies) supplemented with 1% human platelet poor derived serum (Sigma), 1% Penicillin Streptomycin (Thermo Fisher), 2 ng mL^{-1} bFGF (R&D Systems), 10 µM all-trans retinoic acid (Sigma), and 10 µM ROCK inhibitor Y27632 (RI). Inclusion of RI was required to enable cell adhesion, as previously found for collagen-based biomaterials [198]. After two hours, non-adherent dhBMECs were removed and beads were cultured for 24 hours on a shaker at 100 rpm in bead seeding media. To form HUVEC coated beads, identical protocols were used with the following differences: (1) incubation with cells for only one hour, (2) use of HUVEC media without supplementation with RI.

4.2.3. Immunocytochemistry

After 24 hours on a shaker (day 1), beads were fixed and stained to assess protein expression. Beads were rinsed with room-temperature phosphate-buffered saline (PBS; ThermoFisher) and then collected using brief centrifugation (30 seconds at 0.3 g). Beads were fixed using ice-cold methanol for 15 minutes, blocked for 30 minutes in PBS with 10% normal goat serum (Cell Signaling

Technology) and 0.3% Triton X-100 (Millipore Sigma), and then treated with primary antibodies diluted in blocking buffer overnight at 4 ˚C (Table 4-1). After washing with PBS three times, cells were treated with 1:200 Alexa Flour-488 or Alexa Flour-647 secondary antibodies (Life Technologies) diluted in blocking buffer for 45 minutes at room temperature. To physically constrain beads for confocal imaging and to stain cell nuclei, beads were loaded onto eight-chambered borosilicate cover glass wells with Fluoromount-G with DAPI (Invitrogen). Confocal images were acquired at 40x magnification on a swept field confocal microscope system (Prairie Technologies) with illumination provided by an MLC 400 monolithic laser combiner (Keysight Technologies). As a negative control, beads were not exposed to primary antibodies to determine signal due to non-specific secondary antibody binding. To conduct immunocytochemistry of microvessels, antibodies and buffers were perfused through microvessel lumens with identical incubation times.

Table 4-1. Antibodies used in this study.

Antibody	Vendor	Species	Cat. No	Dilution
Occludin	Invitrogen	Rabbit	40-4700	1:100
Claudin-5	Invitrogen	Mouse	35-2500	1:200
GLUT1	Abcam	Rabbit	115730	1:200
P-gp	Sigma	Mouse	P7965	1:100
CD31	ThermoFisher	Rabbit	RB-10333	1:25
FGFR2	R&D	Mouse	MAB684	1:100
VEGFR2	R&D	Mouse	MAB3572	1:100
GPR124	R&D	Mouse	MAB8896	1:100

4.2.4. Permeability assay

Beads were suspended in 200 μM Lucifer yellow (CH dilithium salt; LY) (Sigma) to confirm restriction of paracellular transport. After three hours, confocal images were acquired at the bead midplane to determine accumulation of LY from the fluorescence within beads. Three conditions were tested: (1) blank beads without LY, (2) blank beads with LY, and (3) dhBMEC beads with

LY. A circular region of interest (ROI) within beads was used to compare normalized fluorescence intensity across conditions.

4.2.5. Bead angiogenesis assay

On day 1 (24 hours after seeding dhBMECs), beads were suspended into hydrogels at ~100 beads mL^{-1} and gelled in a 250 μL volume within eight-chambered borosilicate cover glass wells (Lab Tek). Hydrogels were comprised of 6 mg mL^{-1} neutralized rat tail type I collagen (Corning). After 30 minutes of gelation, cell culture media was added on top of hydrogel and replenished daily. Both cell culture media and ECM conditions were toggled to optimize angiogenic growth. Basal media consisted of human endothelial cell serum-free media (Life Technologies) supplemented with 1% human platelet poor derived serum (Sigma) and 1% Penicillin Streptomycin (Thermo Fisher). Basal media was further supplemented with 20 ng mL^{-1} bFGF (R&D Systems), 50 ng mL^{-1} recombinant human Wnt-7a (Wnt7a; Fisher Scientific), and 50 ng mL^{-1} recombinant human VEGF-165 (VEGF; Biolegend).   In some experiments, hydrogels were supplemented with additional ECM components, including 1.5 mg mL^{-1} growth factor reduced Matrigel (Corning), 1.5 mg mL^{-1} fibrin, and 0.5 mg mL^{-1} fibronectin from human plasma. Fibrin composite hydrogels were formed by combining 2 U mL^{-1} thrombin from bovine plasma (Sigma) with 6 mg mL^{-1} neutralized rat tail type I collagen (Corning), before addition of 1.5 mg mL^{-1} fibrinogen from bovine plasma (Sigma). Across all experiments, media was replenished daily (250 μL volume).

4.2.6. Imaging and analysis

Phase contrast and epifluorescence images (Texas Red filter) of beads were acquired on an inverted microscope (Nikon Eclipse TiE) at 10x magnification. For each experimental condition, ten images (technical replicates) of individual beads were collected at day 2, 4 and 6 after embedding in hydrogels. Beads whose endothelium grew along the glass-collagen interface were excluded from analysis. Angiogenic sprouts were defined as perpendicular protrusions from beads, with length

greater than thickness. Three measures were calculated in ImageJ (NIH): (1) Angiogenic percentage (%), defined as the percentage of beads that display angiogenic sprouts, (2) sprout density (# bead^{-1}), and (3) maximum sprout length (μm).

4.2.7.Modeling oxidative stress

Hydrogen peroxide (H$_2$O$_2$; Sigma) was prepared in water and then supplemented in media to final concentrations of 1 mM and 10 μM. Vehicle treatment consisted of 1% water. H$_2$O$_2$ was added after embedding beads in hydrogels and was included in daily media switches. All oxidative stress experiments were conducted in 6 mg mL^{-1} rat tail type I collagen and 1.5 mg mL^{-1} Matrigel, treated with basal media for 6 days.

4.2.8.Microvessel fabrication

Three-dimensional BBB microvessels were fabricated as previously reported [300]. Briefly, 1 cm (length) x 1.75 mm (width) x 1 mm (height) channels were cast in polydimethylsiloxane (PDMS; Dow Corning) using an aluminum mold. Neutralized 6 mg mL^{-1} rat tail type I collagen supplemented with 1.5 mg mL^{-1} Matrigel was gelled surrounding a template 150 μm diameter super-elastic nitinol wire (Malin Co.). After 30 minutes at 37 ˚C, template wires were removed to leave behind a channel that was subsequently seeded with singularized dhBMECs. Microvessels were perfused under ~2 dyne cm^{-2} shear stress using fluid reservoirs as previously reported [328]. For the first 24 hours, "bead seeding medium" was perfused through channels to promote microvessel formation. Then, experimental media were perfused for 6 days.

4.2.9.Hierarchical model

A hierarchical microvascular model was fabricated based on a previously reported model using HUVECs [340]. Two template 150 μm diameter super-elastic nitinol wires were suspended with a separation distance (d) of 100 – 200 μm. Microvessels were perfused at 2 dyne cm^{-2} shear stress. All hierarchical models were generated in 6 mg mL^{-1} rat tail type I collagen and 1.5 mg mL^{-1}

Matrigel, perfused with basal media + 20 ng mL^{-1} bFGF for 5 days. To assess barrier function, 2 µM 500 kDa dextran (Thermo Fisher) was perfused through microvessels for thirty minutes before, during, and after anastomosis. Phase contrast and fluorescence images were acquired every two minutes, as previously reported [328]. ImageJ was used to plot fluorescence intensity over time, where permeability is calculated as $(r/2)(1/\Delta I)(dI/dt)0$, where r is the microvessel radius, ΔI is the jump in total fluorescence intensity upon luminal filling, and $(dI/dt)_0$ is the rate of increase in total fluorescent intensity over one hour [216, 300].

4.2.10. Statistical Analysis

Statistical testing was performed using Prism ver. 8 (GraphPad). Measures are reported as mean ± standard error of the mean (SEM). A one-way analysis of variance (ANOVA) test was used for comparison of three or more groups. Reported p-values were multiplicity adjusted using a Tukey test. Differences were considered statistically significant for $p < 0.05$, with the following thresholds: * $p < 0.05$, ** $p < 0.01$, *** $p < 0.001$.

4.3. Results

4.3.1. Fabrication of a three-dimensional model of brain angiogenesis

To assess the angiogenic potential of iPSC-derived brain microvascular endothelial cells (dhBMECs), we adapted the bead angiogenesis assay [327]. dhBMECs were differentiated from the WTC iPSC line with a fluorescently-tagged plasma membrane (Figure 4-1, A-B). Beads were coated with extracellular matrix (ECM) proteins collagen IV and fibronectin, and then incubated with dhBMECs for 2 hours to achieve a uniform coating (Figure 4-1, C-D). Beads were cultured for 24 hours to enable the formation of a confluent monolayer of dhBMECs (BBB beads). The beads were then embedded within extracellular matrix (ECM) to study chemical and physical cues that guide angiogenesis. An entire six-well plate of dhBMECs is sufficient for coating ~12,000 beads, demonstrating the scalability of our approach.
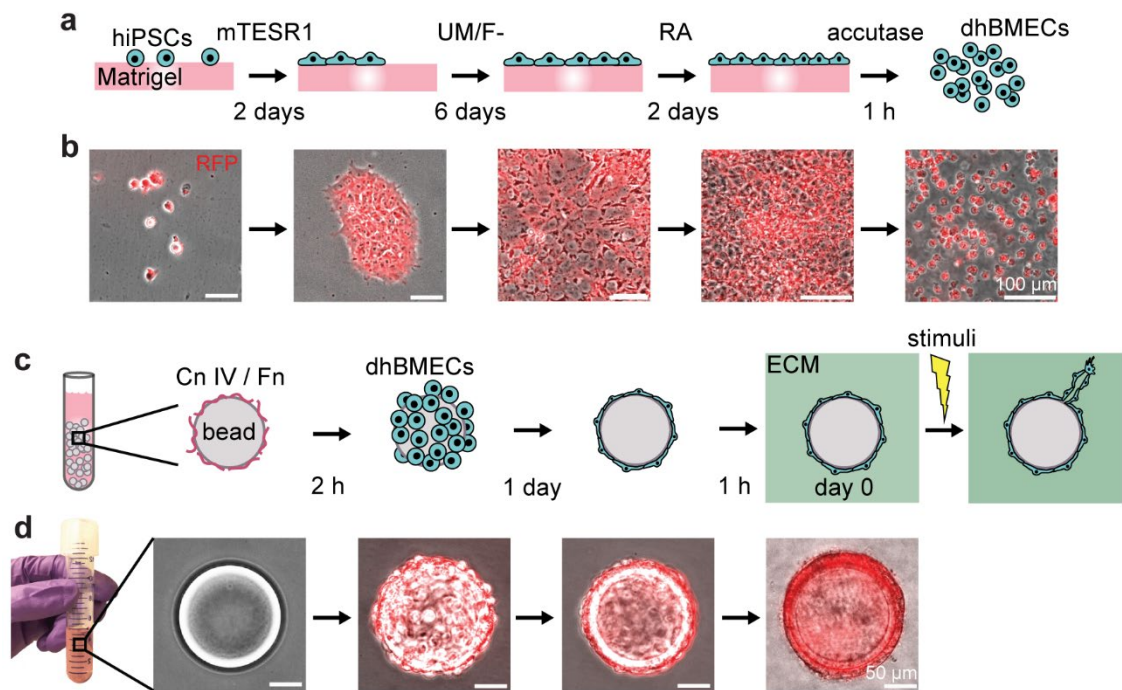
Figure 4-1. Three-dimensional iPSC model of brain angiogenesis. (a) Schematic timeline of the differentiation of human induced pluripotent stem cell (hiPSC) into brain microvascular endothelial cells (dhBMECs) using sequential treatments with mTESR1, UM/F- and RA media (composition defined in Methods) over ten days on Matrigel-coated plates. (b) Phase contrast / epifluorescence overlays corresponding to steps shown in Fig. 1a. WTC iPSC line with RFP-tagged plasma membrane was used. (c) Schematic timeline of the bead angiogenesis assay showing multiplexed coating of beads with collagen IV (Cn IV) and fibronectin (Fn), seeding with dhBMECs, formation of blood-brain barrier (BBB) beads, embedding of BBB beads into extracellular matrix (ECM), and treatment with angiogenic stimuli. (d) Phase contrast / epifluorescence overlays corresponding to steps shown in Fig. 1c.

Beads coated with dhBMECs display expression of key BBB and endothelial markers, including claudin-5, occludin, glucose transporter 1 (GLUT1), p-glycoprotein (Pgp), and CD31 (Figure 4-2, A), as previously reported in 2D assays [194, 196, 197]. Protein expression of BBB markers was unique to dhBMECs, while the endothelial marker (CD31) was also expressed by human umbilical vein endothelial cells (HUVECs) (Figure 4-3). Additionally, BBB beads express the critical angiogenic ligand receptors fibroblast growth factor receptor 2 (FGFR2), vascular endothelial growth factor receptor 2 (VEGFR2), and G protein-coupled receptor 124 (GPR124) (Figure 4-2,

B). Since tight junction proteins (claudin-5 and occludin) restrict paracellular transport into the brain, barrier function was assessed by incubating beads in Lucifer yellow (LY) for 3 hours (Figure 4-2, C). Three conditions were tested: (1) blank beads (no dhBMECs) without LY, (2) blank beads with LY, and (3) beads with a dhBMEC monolayer with LY.   The core of the beads is comprised of a permeable dextran polymer and hence beads without a dhBMEC monolayer showed high fluorescence intensity after three hours incubation with LY. In contrast, beads with a dhBMEC monolayer significantly restricted accumulation of solutes within the core (p < 0.001) (Figure 4-2, D-E). Beads with HUVEC monolayers restrict Lucifer yellow accumulation less than dhBMECs (p = 0.028), consistent with previous studies showing that dhBMECs display at least 10-fold lower permeability compared to HUVECs [300, 341] (Figure 4-4, A).

4.3.2.Influence of chemical factors

To assess the influence of pro-angiogenic factors, we incubated BBB beads in three media conditions: (1) basal media, (2) basal media + 20 ng mL^{-1} bFGF, and (3) basal media + 20 ng mL^{-1} bFGF + 50 ng mL^{-1} VEGF + 50 ng mL^{-1} wnt7a. Across these conditions, the BBB beads were embedded within 6 mg mL^{-1} collagen I hydrogels.   In the absence growth factors, angiogenic behavior was not widely observed (Figure 4-5, A): after six days, only 10% of beads displayed visible sprouts (Figure 4-5, B). In the presence of bFGF alone, some angiogenic behavior was observed. The angiogenic fraction and maximum sprout lengths were increased compared to beads cultured in the absence of bFGF (p = 0.026 and p = 0.013, respectively), while sprout density was not statistically different (p = 0.097) (Figure 4-5, B-D). The addition of VEGF and wnt7a produced on average higher angiogenic phenotype (Figure 4-5, A), which was increased compared to basal conditions (p = 0.004, 0.012, and 0.018, respectively), but not statistically significant compared to bFGF exposure alone (Figure 4-5, B-D). The average sprout length for beads in VEGF and wnt7a increased linearly with time with a growth rate of approximately 20 µm day^{-1} (Figure 4-5, E).
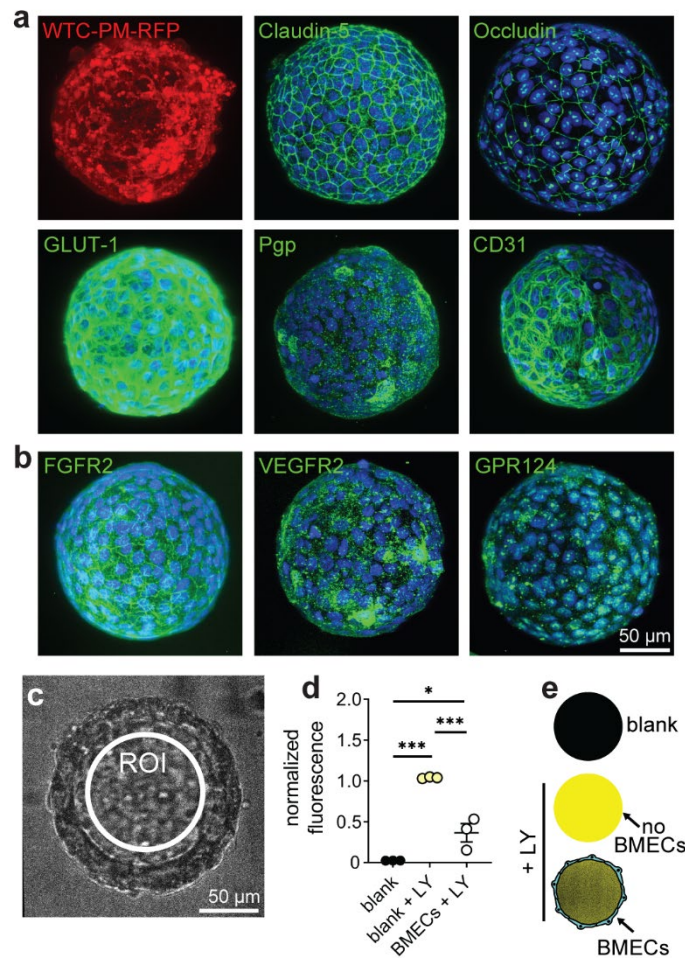
Figure 4-2. Characterization of BBB beads: protein expression and function. (a) Confluent monolayers of dhBMECs on 150 μm diameter beads express localized tight junction proteins (occludin and claudin-5), the glucose transporter-1 (GLUT1) nutrient transporter, the p-glycoprotein (Pgp) efflux pump, and endothelial markers (CD31). (b) BBB beads express receptors for basic fibroblast growth factor (FGFR2), vascular endothelial growth factor (VEGFR2), and wnt7a (GPR124). Beads were incubated in 200 μM Lucifer yellow (LY) for 3 hours. Three conditions were tested: (1) blank beads without LY, (2) blank beads with LY, and (3) beads with dhBMEC monolayers with LY. (c) Quantification of LY fluorescence in a circular region of interest (ROI) within the beads using confocal microscopy (shown is corresponding phase contrast image). (d) Comparison of normalized fluorescence across conditions (N = 3). (e) Normalized fluorescence images for each condition; beads with dhBMECs significantly restrict accumulation of LY. dhBMECs were generated from the plasma membrane (PM) RFP-tagged WTC iPSC line. * $p < 0.05$. *** $p < 0.001$.
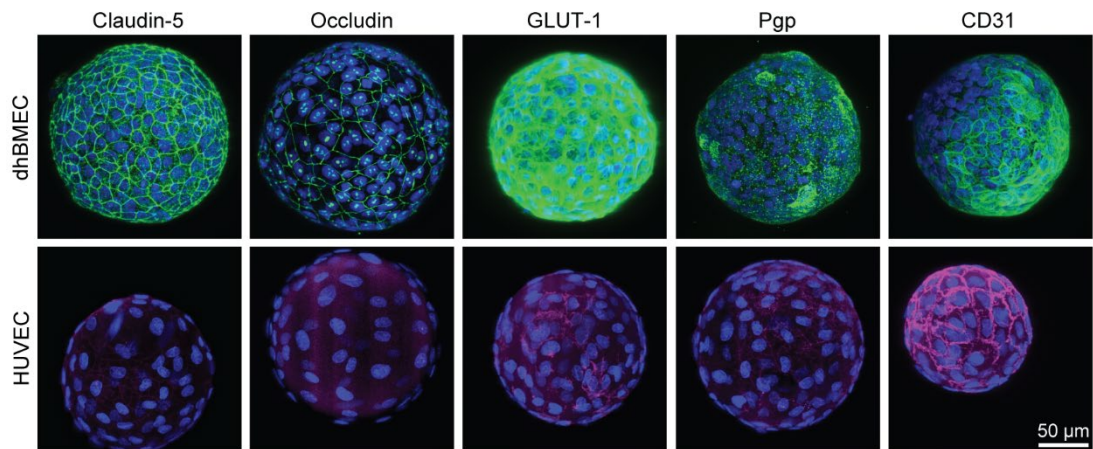
Figure 4-3. Comparison of protein expression between dhBMECs and HUVECs. Beads were coated with dhBMECs or HUVECs and stained for various BBB and endothelial markers. HUVEC beads share expression of CD31 with dhBMEC beads, but do not express other canonical BBB proteins.
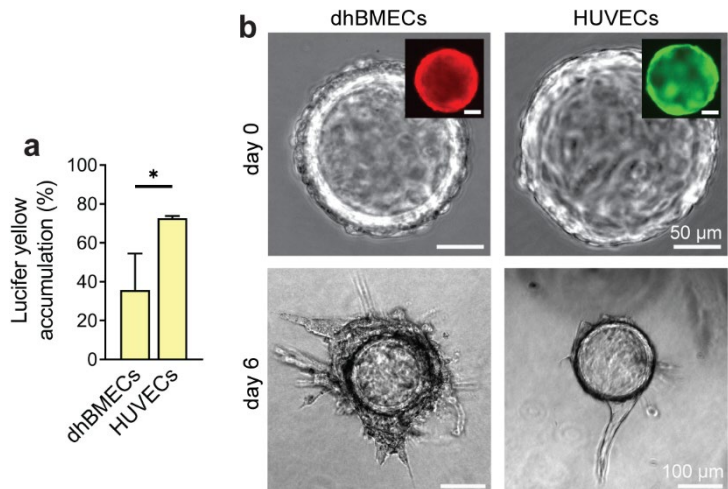
Figure 4-4. Comparison of phenotype and angiogenic behavior on beads with confluent monolayers of dhBMECs or HUVECs. (a) Percentage accumulation of Lucifer yellow within beads containing cell monolayers relative to beads without cell monolayers for both cell types. (b) Beads display identical appearances before embedding within hydrogel. After 6 days, HUVECs display lower sprout density but higher sprout length were embedded within 6 mg mL^{-1} collagen I hydrogels and supplemented with basal media + 20 ng mL^{-1} bFGF + 50 ng mL^{-1} VEGF + 50 ng mL^{-1} wnt7a.
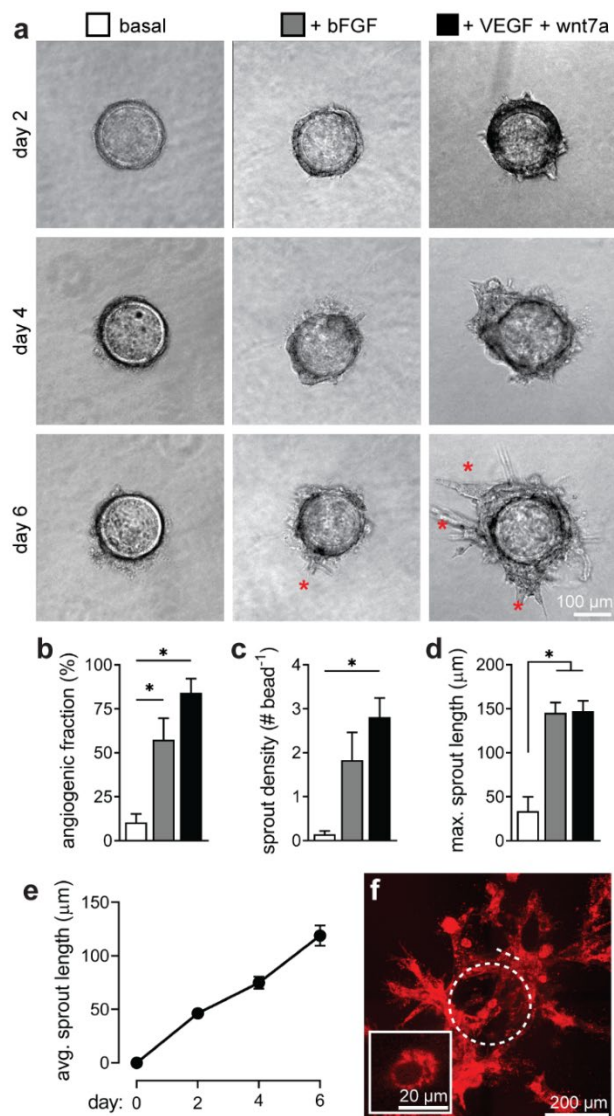
Figure 4-5. Influence of chemical factors on dhBMEC angiogenesis. Three media conditions were tested: (1) basal media, (2) basal media + 20 ng mL^{-1} bFGF, and (3) basal media + 20 ng mL^{-1} bFGF + 50 ng mL^{-1} VEGF + 50 ng mL^{-1} wnt7a. Across these conditions, dhBMEC beads were embedded within 6 mg mL^{-1} collagen I hydrogels. (a) Representative images of beads on day 2, 4 and 6 after embedding in hydrogels. Sprouts are marked with red asterisks. (b-d) Angiogenic fraction, sprout density and maximum sprout length quantified across conditions on day 6. (e) Plot of maximum sprout length over time for treatment with basal media + 20 ng mL^{-1} bFGF + 50 ng mL^{-1} VEGF + 50 ng mL^{-1} wnt7a. (f) Confocal image of angiogenic processes at day 6 in basal media + 20 ng mL^{-1} bFGF + 50 ng mL^{-1} VEGF + 50 ng mL^{-1} wnt7a. The image is a maximum intensity projection over a depth of 240 μm, with inset demonstrating a lumen-like structure. The dotted circle represents the border of the bead; the dotted line represents the location of the cross-section shown in the inset. Data obtained from N = 5 rounds of the bead assay from unique differentiations, with greater than 5 technical replicates per differentiation. * $p < 0.05$. ** $p < 0.01$.

104
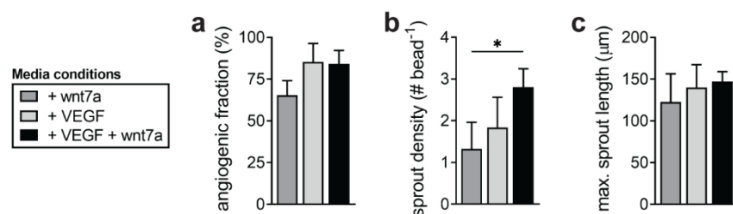
Figure 4-6. Individual contributions of VEGF and wnt7a to angiogenic behavior. For each condition dhBMEC beads were embedded within 6 mg mL^{-1} collagen I hydrogels and then exposed to basal media + 20 ng mL^{-1} bFGF with additional: (1) 50 ng mL^{-1} wnt7a, (2) 50 ng mL^{-1} VEGF, or (3) 50 ng mL^{-1} VEGF + 50 ng mL^{-1} wnt7a. (a-c) Angiogenic fraction, sprout density and maximum sprout length quantified across conditions on day 6. Data obtained from N = 5 rounds of the bead assay from unique differentiations, with greater than 5 technical replicates per differentiation. * p < 0.05.

Confocal imaging of BBB beads cultured in VEGF and wnt7a showed extensive networks of angiogenic sprouts and formation of lumen-like structures (Figure 4-5, F). Sprouts on the BBB beads appear predominately comprised of tip cells, while sprouts on HUVEC beads were longer (albeit less dense) and appeared to develop tip and stalk cell appearances (Figure 4-4, B). We also analyzed the individual contributions of VEGF and wnt7a compared to the combination of these two angiogenic factors (Figure 4-6). The predominant contributor to angiogenic behavior was VEGF, which displayed similar angiogenic fractions and maximum sprout lengths compared to the combination (p = 0.990 and 0.921, respectively). However, sprout density most widely varied between these conditions, with wnt7a and VEGF synergistically producing the highest sprout density compared to wnt7a alone (p = 0.030).

4.3.3. Influence of extracellular matrix components

To assess the role of matrix composition, we tested four ECM conditions: (1) 6 mg mL^{-1} collagen I, (2) 6 mg mL^{-1} collagen I + 1.5 mg mL^{-1} growth factor reduced Matrigel, (3) 6 mg mL^{-1} collagen I + fibronectin, and (4) 6 mg mL^{-1} collagen I + fibrin. Matrigel is predominately comprised of laminin, along with other ECM components [342]. Across these conditions, beads were exposed to basal media + 20 ng mL^{-1} bFGF + 50 ng mL^{-1} VEGF + 50 ng mL^{-1} wnt7a. Changing ECM

composition (without dramatically altering hydrogel biomechanics) had a less dramatic effect on angiogenic phenotype compared to soluble angiogenic factors: a similar sprouting morphology were observed across the conditions (Figure 4-7, A). The angiogenic fraction was similar across additions of ECM components and significant differences were not observed ($p > 0.05$ for all comparisons) (Figure 4-7, B). Matrigel supplementation led to increased sprout compared to fibronectin, suggesting that these two ECM conditions represent the most and least pro-angiogenic, respectively ($p = 0.03$) (Figure 4-7, C). Maximum sprout length was generally increased in response to the addition of ECM components, but was not significantly different ($p > 0.05$ for all comparisons) (Figure 4-7, D). For all subsequent experiments collagen I was supplemented with Matrigel to model angiogenic phenotype.
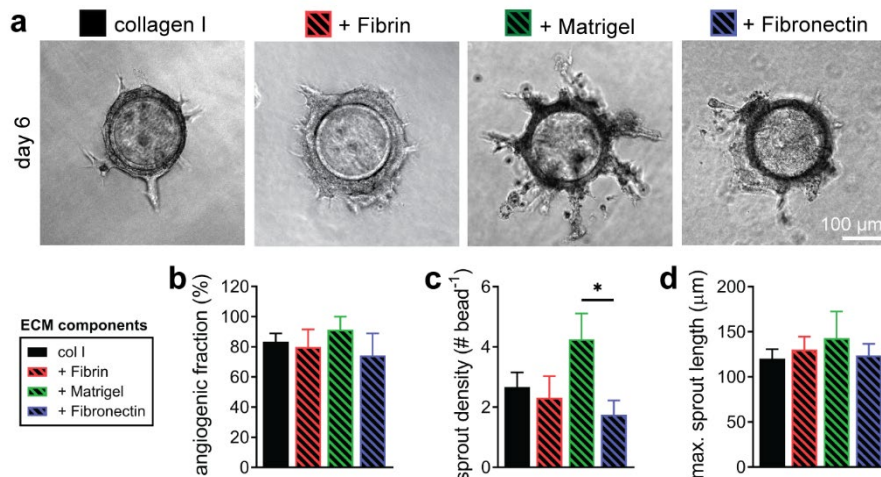
Figure 4-7. Influence of extracellular matrix components on dhBMEC angiogenesis. Four ECM conditions were tested: (1) 6 mg mL^{-1} collagen I, (2) 6 mg mL^{-1} collagen I + 1.5 mg mL^{-1} fibrin, (3) 6 mg mL^{-1} collagen I + 1.5 mg mL^{-1} Matrigel, (4) 6 mg mL^{-1} collagen I + 0.5 mg mL^{-1} fibronectin. Across these conditions, a combination of bFGF, VEGF and wnt7a were applied (media condition #3). (a) Representative images of dhBMEC beads on day 6 after embedding in hydrogels, across conditions. (b-d) Angiogenic fraction, sprout density, and maximum sprout length quantified across conditions on day 6. Data obtained from N = 5 rounds of the bead assay from unique differentiations, with greater than 5 technical replicates per differentiation. * $p < 0.05$.

4.3.4. Modeling pathological angiogenesis

To model pathological brain angiogenesis, we exposed the BBB beads to high and low concentrations of hydrogen peroxide (H_2O_2) in the absence of external growth factor stimuli. H_2O_2 induces production of reactive oxygen species (ROS), whose levels are elevated during neurodegenerative disease, brain cancer, and stroke [343]. After two days exposure to 10 μM H_2O_2, the formation of sprouts into the ECM highlights an increased angiogenic phenotype (Figure 4-8, A). The sprout density was significantly increased compared to vehicle treatment ($p = 0.047$) (Figure 4-8, B). Interestingly, the pro-angiogenic effects of 10 μM H_2O_2 were not maintained over time as by day 6 angiogenic behavior was lost, while vehicle treatment displays minor angiogenic behavior (Figure 4-8, C). This suggests that 10 μM H_2O_2 exerts a bimodal effect of angiogenic phenotype. Interestingly, the addition of 100-fold higher H_2O_2 (1 mM) abrogates angiogenic behavior on much shorter time scales (no sprouts are observed) (Figure 4-8, A-C). At this concentration cell fluorescence was gradually lost, suggesting progressive cell death, while at all other conditions fluorescence was maintained over six days (data not shown).
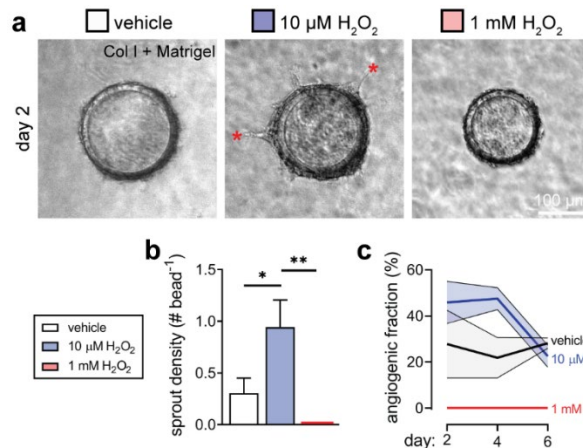
Figure 4-8. Influence of oxidative stress on dhBMEC angiogenesis. dhBMEC beads were exposed to vehicle (H_2O), 10 μM, and 1 mM hydrogen peroxide (H_2O_2) after embedding into collagen I + Matrigel hydrogels supplemented with basal media. (a) Phase contrast images of angiogenic behavior across conditions on day 2. Sprouts are marked with red asterisks. (b) Day 2

sprout density across conditions. (c) Time course of angiogenic fraction across conditions. Data obtained from N = 4 rounds of the bead assay from unique differentiations, with greater than 5 technical replicates per differentiation. * $p < 0.05$, ** $p < 0.01$.

4.3.5. Perfusable microvessel models of brain angiogenesis

Next, we tested the role of chemical cues for *in vitro* dhBMEC angiogenesis within a tissue-engineered perfusable microvessel model. These experiments mimic techniques previously demonstrated to study angiogenesis from an existing three-dimensional microvessel [340, 344, 345]. Microvessels were formed in 150 μm diameter channels within 6 mg mL^{-1} type I collagen supplemented with 1.5 mg mL^{-1} Matrigel (Figure 4-9, A-B). Channels were seeded with dhBMECs, which under continual ~2 dyne cm^{-2} perfusion, assembled into BBB microvessels, as previously reported [300]. After microvessel formation, we applied media conditions as tested in Figure 4-5 to observe angiogenic behavior (Figure 4-9, C).
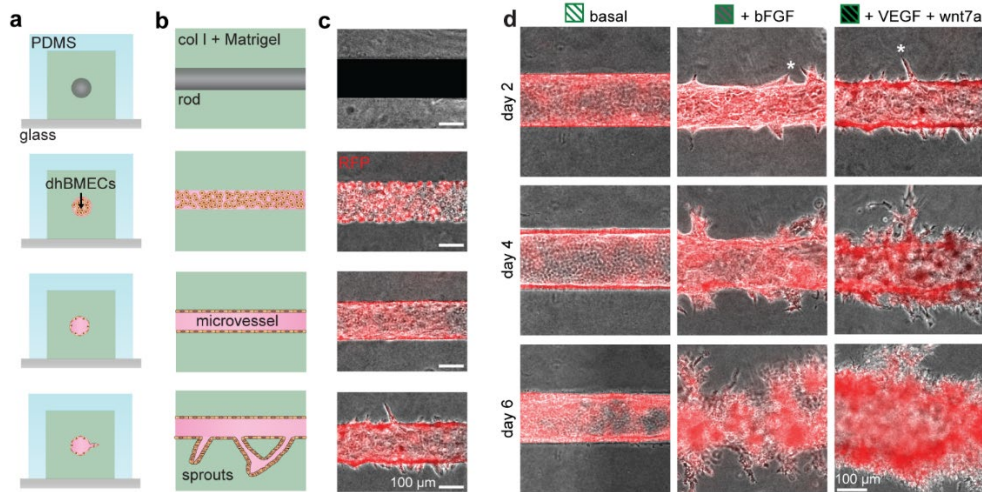
Figure 4-9. Modeling angiogenesis from tissue-engineered brain microvessels. (a-b) Schematic illustrations showing front and side views of model fabrication. Angiogenic factors are introduced after microvessel formation (one day after seeding BMECs) to promote sprouting. (c) Phase contrast and fluorescence image overlays of fabrication process. (d) Phase contrast and fluorescence image overlays of representative microvessels perfused with media conditions matching Figure 5. Early sprouts are marked with white asterisks.

Under perfusion with basal media, angiogenic behavior was not widely observed and the microvessel structure remained stable over six days (Figure 4-9, D). Supplementation with bFGF resulted in early sprouts within two days, which continued to grow in length and branching complexity (Figure 4-9, D). Supplementation with bFGF, VEGF, and wnt7a resulted in an increased density of sprouts along microvessels after two days, and chaotic sprouting behavior by six days (Figure 4-9, D). Both growth factor supplementation regimes were associated with loss of microvessel perfusion after 5 - 6 days due to overgrowth and constriction of microvessel lumens. Based on these results we chose to further explore bFGF supplementation over four days to promote formation of organized microvascular lumens.

4.3.6. Hierarchical model of the human blood-brain barrier

Lastly, we sought to engineer a hierarchical model of the human brain microvasculature by promoting sprouting between adjacent BBB microvessels. This technique has previously been demonstrated using HUVECs [340]. We patterned adjacent 150 μm diameter channels within 6 mg mL^{-1} type I collagen supplemented with 1.5 mg mL^{-1} Matrigel separated by $100 - 200$ μm (Figure 4-10, A-B). After microvessel formation, microvessels were perfused at ~2 dyne cm^{-2} with basal media + 20 ng mL^{-1} bFGF (Figure 4-10, C). Continual perfusion over three days resulted in linking of sprouts between microvessels (Figure 4-10, D).

While angiogenesis and BBB formation are simultaneous during development [73], during adulthood brain angiogenesis is typically associated with BBB breakdown [151, 346, 347]. Here, we observed that both microvessels and perfusable capillaries restricted transport of 500 kDa dextran, providing evidence that lumens formed between microvessels maintain barrier function (Figure 4-10, E). Perfusable lumens were typically $20 - 30$ μm in diameter, while smaller diameter connections between microvessels did not routinely display lumens (Figure 4-10, F). Further studies are required to optimize lumen formation and to fully characterize the barrier properties of
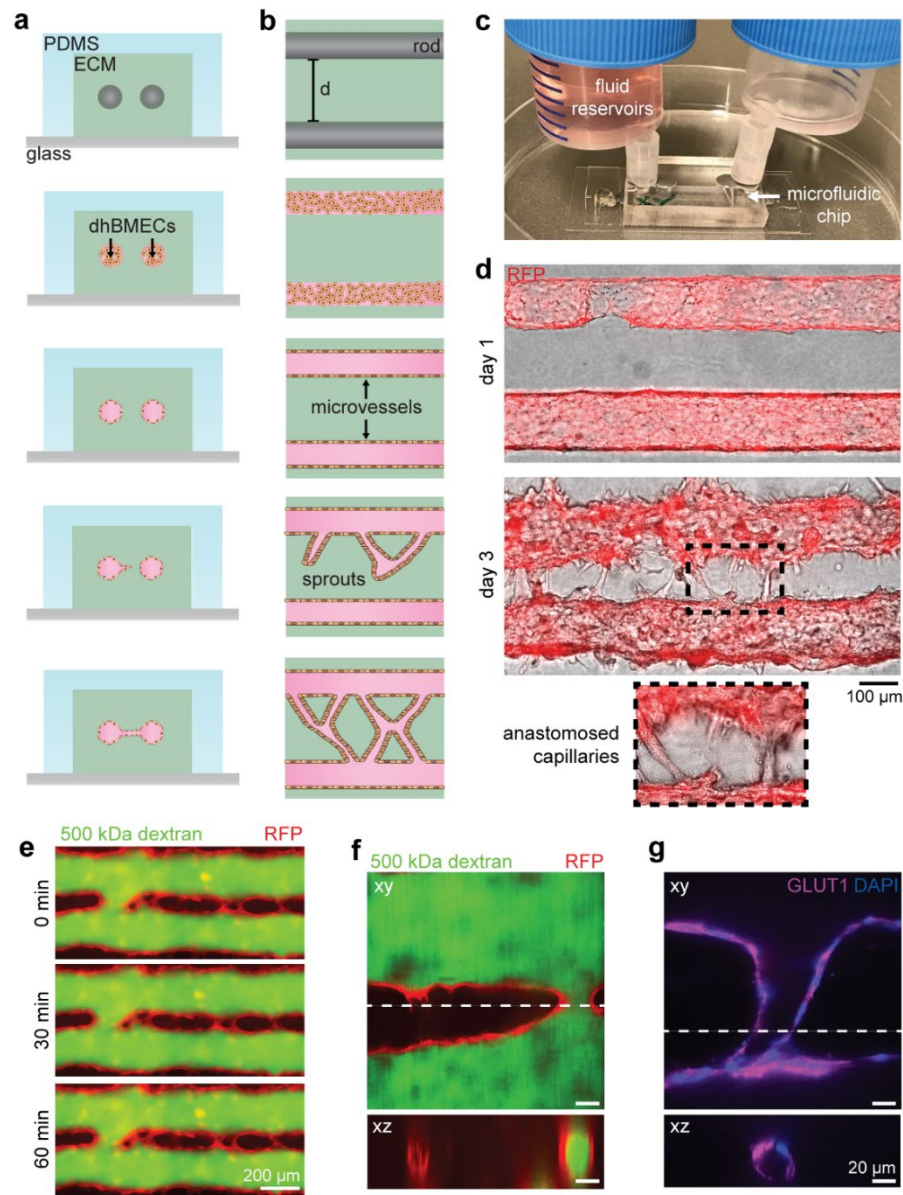
Figure 4-10. Hierarchical model of the BBB via angiogenesis between existing tissue-engineered brain microvessels. (a-b) Front and side view schematics of hierarchical model of brain angiogenesis. (c) Flow system under to control perfusion of hierarchal model. (d) Phase contrast and fluorescence image overlays of hierarchical capillary network formation. After formation in basal media, microvessels are perfused at 2 dyne cm^{-2} with 20 ng mL^{-1} bFGF to promote anastomosis of sprouts. Anastomosed capillaries are visible after 3 days. (e) Hierarchical model perfused with 500 kDa dextran for one hour. No leakage of dye was observed indicating that capillaries were intact and preserved barrier function. (f) Confocal imaging of capillary lumen perfused with 500 kDa dextran. (g) Confocal imaging of glucose transporter-1 (GLUT1) nutrient transporter. Confocal images are shown at a specific z-plane, with the xz cross-section denoted as a dotted while line.

this model. As BBB formation is induced via GLUT1 expression during development [71], we stained angiogenic processes to confirm robust expression of GLUT1 similar to that of parental microvessels (Figure 4-10, G).

4.4. Discussion

4.4.1. Factors that regulate in vitro brain angiogenesis

The formation of brain capillaries during development occurs through the convergence of multiple signaling pathways [6, 7, 348]. Vascular endothelial growth factor (VEGF) released by the developing neural tube initiates formation of the perineural vascular plexus (PNVP) via vasculogenesis. From the PNVP, BMECs invade the brain parenchyma via angiogenesis driven by chemical cues released by developing neurons (e.g. wnt7a/b) and mechanical interactions with the brain parenchyma [6, 7, 348]. The culmination of brain angiogenesis during development results in a hierarchical BBB with profound heterogeneity in structure and phenotype [230, 347, 349]. However, after development, angiogenesis is generally restricted to pathological conditions which alter BBB structure and phenotype [151, 346, 347]. Here we developed an *in vitro* model of brain angiogenesis using iPSC-derived BMECs (dhBMECs) to study brain angiogenesis. We explored multiple factors that alter angiogenic phenotype of brain microvascular endothelial cells, including growth factors, ECM composition, and oxidative stress.

Critical chemical cues implicated in developmental brain angiogenesis include vascular endothelial growth factor (VEGF) [70] and wnt7a/b (WNT) [71]. WNT signaling is specifically required for brain angiogenesis and is harnessed during differentiation of hiPSC-derived BMECs [194]. However, other growth factors, including basic fibroblast growth factor (bFGF), are also implicated in promoting brain angiogenesis [350, 351]. Here we found that all three growth factors are likely pro-angiogenic for dhBMECs. In previous studies of primary brain microvascular endothelial cells using a tube formation assay [326], hypoxia was found to increase VEGF expression but was

insufficient to promote formation of new vessels. In contrast, we found that angiogenic factors are sufficient to promote angiogenesis of dhBMECs within a 3D microenvironment, supporting the development of more physiological angiogenesis models.

Additionally, ECM composition and stiffness are key regulators of angiogenesis [352-355]. Numerous studies have shown that increased ECM stiffness reduces angiogenesis, likely by limiting cell proliferation and migration [354, 355]. Pro-angiogenic ECM proteins include collagen I, fibronectin, and laminin [352]. In studies specific to BMECs, fibronectin and laminin were shown to promote angiogenic and maturation phenotype, respectively [356]. The extracellular space in the brain is comprised of hyaluronic acid, lecticans, proteoglycan link proteins, and tenascins [357, 358]. However, as the human brain is highly cellular by volume, non-brain-specific ECM components are commonly used to mimic the physical properties of the brain *in vitro* [26, 359, 360]. For example, 3D BBB models commonly utilize non-brain ECM components including collagen I [186-189, 300, 361] and fibrin [180, 209, 336, 362]. We previously characterized and compared the stiffness of collagen I hydrogels to native mouse brain, and showed that 6 mg mL^{-1} collagen is a reasonable proxy for brain stiffness [328]. Additionally, materials with stiffnesses much lower than native brain were not conducive to the formation of stable BBB microvessels [328]. Thus, we chose to only explore ECM materials with sufficient stiffness to form perfusable microvessel models, despite their absence within the brain parenchyma. We found that addition of growth factor-reduced Matrigel (primarily composed of laminin) to a collagen I matrix increased angiogenic phenotype. Interestingly, fibronectin which plays a critical role *in vivo*, was not found to alter sprouting *in vitro*; this could result from differences in integrin expression on dhBMECs, use of suboptimal fibronectin concentrations, or differences in other microenvironmental variables. Higher concentrations of fibronectin were not tested as they required substantial alteration of bulk hydrogel mechanical properties.

Under homeostatic conditions angiogenesis is not prevalent in the adult brain, however, brain angiogenesis is associated with pathological conditions, including neurodegenerative disease, brain cancer, and stroke [347]. Production of reactive oxygen species (ROS) is associated with these conditions and may contribute to BBB disruption and pathological angiogenesis [343]. Reactive oxygen species promote angiogenesis via both VEGF-dependent and independent mechanisms [363]. Previous work utilizing primary rat BMECs found that H_2O_2 displays a concentration-dependent influence on angiogenic behavior: concentrations below 10 μM increased tube length in a Matrigel tube formation assay, while concentrations above 10 μM decreased tube length [325]. Here, the use of BBB beads provides spatial and temporal resolution to study the time-dependent effects of oxidative stress, which have previously been ignored. We found that H_2O_2 exerts a bimodal and concentration-dependent effect on brain angiogenesis.

4.4.2. Model advantages and limitations

2D models of brain angiogenesis (i.e. transwell assay or Matrigel tube forming assay) are unable to recapitulate the spatial dynamics of BMEC sprouting. Recently, 3D models of the brain microvasculature have been engineered via mimicry of vasculogenesis or angiogenesis using co-cultured primary ECs or BMECs, pericytes, and astrocytes [180, 209, 336]. Additionally, a microfluidic model of neurogenesis and angiogenesis was formed using co-cultured mesenchymal stem cells, primary BMECs, and neural stem cells, but was not tested for functional BBB properties [362]. While hiPSC-derived BMECs have been used to create microfluidic co-culture models of the BBB [332], this platform is not conducive for mimicking brain angiogenesis.

The bead assay incorporates a confluent monolayer of dhBMECs on a polymer bead which can be used in suspension or embedded in a matrix. Since there are no boundaries to the monolayer, this geometry avoids the perimeter effect associated with transwell assays. Furthermore, the bead assay uses 2000x less cells per technical replicate (i.e. one bead or transwell) and enables direct

visualization of the endothelium. This model supports controlled studies of microenvironmental cues and genetic mutations on angiogenesis, without confounding factors present *in vivo*. Additionally, previous models have utilized fibrin for creating brain microvascular networks via angiogenesis and vasculogenesis-like processes [180, 209, 336]. Although neither collagen I nor fibrin is found in native brain ECM, collagen I densities used in this study are similar to the mechanical stiffness of native brain.

There are two main limitations to our model. (1) Brain angiogenesis *in vivo* occurs in the presence of complex cell-cell interactions, which are neglected in our model: BMECs interact with neurons, neural progenitor cells, pericytes, and glial progenitors during brain angiogenesis. As previously discussed, neurons and neural progenitor cells release critical chemical stimuli including wnt ligands and VEGF, which we introduce to promote sprouting in our model. Pericytes are an important cellular component of the neurovascular unit as they physically support new capillaries and are required for the formation of the BBB during development [231, 364]. Astrocytes are not critically involved in angiogenesis, as they are not present during initial brain vascularization; however, postnatally, they release ligands that maintain BBB integrity [76]. Lastly, radial glial cells guide spatial patterning of angiogenesis as a physical scaffold for endothelial cell migration [7, 365]. Recent reports of an isogenic multicellular iPSC-based BBB transwell assay provide the foundations for building more complex angiogenesis models [366]. Additionally, we previously incorporated iPSC-derived pericytes into a 3D microvessel BBB model, showing that they do not significantly alter barrier properties [320]. Future work is required to examine how iPSC-derived pericytes and other cells of the BBB may alter angiogenesis *in vitro*. (2) The stability of angiogenic vessels is not addressed: the adult cerebrovasculature is highly stable, with limited angiogenesis [347]. For example, over 30 days changes in capillary length, diameter or branching were not observed in the adult mouse somatosensory and motor cortex [32]. Thus, models of the

cerebrovasculature should aim to mimic physiological structural and phenotypic stability. We previously explored the stability of BBB microvessels, finding that microvessels reach quiescence over several days (when rates of cell division match cell apoptosis) [300]. However, the stability of microvessels formed via angiogenesis has not been addressed. As growth factor expression can display unique temporal and spatial expression patterns [70], transient administration or removal of growth factors may aid in generating stable microvessels. Future work will explore how removal of growth factors after angiogenesis occurs alters the structural and phenotypic stability of tissue-engineered cerebrovascular models. Additionally, many other stimuli influence the morphology of microvasculature *in vitro*, including flow and shear stress [353, 367], which could be harnessed to promote stability.

4.4.3. Engineering BBB hierarchy

To promote sprouting and anastomosis of capillaries between adjacent tissue-engineered microvessels we applied angiogenic factors which maximized growth rates. In previous work, capillary growth rates of ~40 μm day^{-1} were sufficient to anastomose adjacent HUVEC microvessels [340]. Here we observed more modest growth rates for dhBMECs (~20 μm day^{-1}). Previously it has been found that iPSC-derived endothelial cells exhibit reduced angiogenic potential compared to primary ECs (HUVECs), likely due to differences in MMP production [368]. Due to limitations with primary and immortalized BMEC sources we did not explore cell source-dependent angiogenic differences. Importantly, our hierarchical model allows probing of how BBB phenotype changes across the vascular tree. Recently, we demonstrated use of BBB microvessels for studying hyperosmotic BBB disruption [282], but do not know if capillaries are more susceptibility to opening.

4.5.Conclusions

Existing *in vitro* models have generally failed to mimic brain angiogenesis or recapitulate physiological barrier function, hierarchy, and zonation of the human BBB. Here, we develop 3D *in vitro* stem cell-based models of brain angiogenesis, including a high-throughput BBB bead assay and perfusable microvessel model. These models have diverse applications in screening the influence of chemical, mechanical, cell genotype, and stress signals on brain angiogenesis.

Bibliography

1. Bogorad, M.I., et al., *Cerebrovascular plasticity: Processes that lead to changes in the architecture of brain microvessels.* J Cereb Blood Flow Metab, 2019: p. 271678X19855875.
2. Aiello, L.C. and P. Wheeler, *The Expensive-Tissue Hypothesis - the Brain and the Digestive-System in Human and Primate Evolution.* Current Anthropology, 1995. **36**(2): p. 199-221.
3. Wong, A.D., et al., *The blood-brain barrier: an engineering perspective.* Front Neuroeng, 2013. **6**: p. 7.
4. Zlokovic, B.V., *Neurovascular mechanisms of Alzheimer's neurodegeneration.* Trends Neurosci, 2005. **28**(4): p. 202-8.
5. Karbowski, J., *Scaling of Brain Metabolism and Blood Flow in Relation to Capillary and Neural Scaling.* PLoS One, 2011. **6**(10).
6. Zhao, Z., et al., *Establishment and Dysfunction of the Blood-Brain Barrier.* Cell, 2015. **163**(5): p. 1064-78.
7. Walchli, T., et al., *Wiring the Vascular Network with Neural Cues: A CNS Perspective.* Neuron, 2015. **87**(2): p. 271-96.
8. Saunders, N.R., et al., *The rights and wrongs of blood-brain barrier permeability studies: a walk through 100 years of history.* Front Neurosci, 2014. **8**: p. 404.
9. Chen, B.R., et al., *A critical role for the vascular endothelium in functional neurovascular coupling in the brain.* Journal of the American Heart Association, 2014. **3**(3): p. e000787.
10. Boero, J.A., et al., *Increased brain capillaries in chronic hypoxia.* J Appl Physiol (1985), 1999. **86**(4): p. 1211-9.
11. Obenaus, A., et al., *Traumatic brain injury results in acute rarefication of the vascular network.* Sci Rep, 2017. **7**(1): p. 239.
12. Keaney, J., et al., *Autoregulated paracellular clearance of amyloid-beta across the blood-brain barrier.* Sci Adv, 2015. **1**(8): p. e1500472.
13. Cipolla, M.J., in *The Cerebral Circulation*. 2009: San Rafael (CA).
14. Moore, K.L., A.F. Dalley, and A.M. Agur, *Clinically oriented anatomy*. 2013: Lippincott Williams & Wilkins.
15. Moody, D., M. Bell, and V. Challa, *Features of the cerebral vascular pattern that predict vulnerability to perfusion or oxygenation deficiency: an anatomic study.* American Journal of Neuroradiology, 1990. **11**(3): p. 431-439.
16. Shardlow, E. and A. Jackson, *Cerebral blood flow and intracranial pressure.* Anaesthesia and Intensive Care Medicine, 2008. **9**: p. 222-225.
17. Reina-De La Torre, F., A. Rodriguez-Baeza, and J. Sahuquillo-Barris, *Morphological characteristics and distribution pattern of the arterial vessels in human cerebral cortex: a scanning electron microscope study.* Anat Rec, 1998. **251**(1): p. 87-96.
18. Farkas, E. and P.G. Luiten, *Cerebral microvascular pathology in aging and Alzheimer's disease.* Prog Neurobiol, 2001. **64**(6): p. 575-611.
19. Paulson, O.B., S. Strandgaard, and L. Edvinsson, *Cerebral autoregulation.* Cerebrovasc Brain Metab Rev, 1990. **2**(2): p. 161-92.
20. Leenders, K.L., et al., *Cerebral blood flow, blood volume and oxygen utilization. Normal values and effect of age.* Brain, 1990. **113 (Pt 1)**: p. 27-47.

21. Ito, H., et al., *Changes in human cerebral blood flow and cerebral blood volume during hypercapnia and hypocapnia measured by positron emission tomography.* Journal of Cerebral Blood Flow & Metabolism, 2003. **23**(6): p. 665-670.

22. Cavaglia, M., et al., *Regional variation in brain capillary density and vascular response to ischemia.* Brain Res, 2001. **910**(1-2): p. 81-93.

23. Craige, E.H., *The architecture of the cerebral capillary bed.* Biological Reviews, 1945. **20**(4): p. 133-146.

24. Santisakultarm, T.P., et al., *In vivo two-photon excited fluorescence microscopy reveals cardiac-and respiration-dependent pulsatile blood flow in cortical blood vessels in mice.* American Journal of Physiology-Heart and Circulatory Physiology, 2012. **302**(7): p. H1367-H1377.

25. Hudetz, A.G., *Blood flow in the cerebral capillary network: a review emphasizing observations with intravital microscopy.* Microcirculation, 1997. **4**(2): p. 233-252.

26. DeStefano, J.G., et al., *Benchmarking in vitro tissue-engineered blood-brain barrier models.* Fluids Barriers CNS, 2018. **15**(1): p. 32.

27. Owens, T., I. Bechmann, and B. Engelhardt, *Perivascular Spaces and the Two Steps to Neuroinflammation.* Journal of Neuropathology and Experimental Neurology, 2008. **67**(12): p. 1113-1121.

28. Kienast, Y., et al., *Real-time imaging reveals the single steps of brain metastasis formation.* Nature Medicine, 2010. **16**(1): p. 116-122.

29. Masocha, W. and K. Kristensson, *Passage of parasites across the blood-brain barrier.* Virulence, 2012. **3**(2): p. 202-12.

30. Abbott, N.J., L. Ronnback, and E. Hansson, *Astrocyte-endothelial interactions at the blood-brain barrier.* Nature Reviews Neuroscience, 2006. **7**(1): p. 41-53.

31. Iadecola, C., *The neurovascular unit coming of age: a journey through neurovascular coupling in health and disease.* Neuron, 2017. **96**(1): p. 17-42.

32. Cudmore, R.H., S.E. Dougherty, and D.J. Linden, *Cerebral vascular structure in the motor cortex of adult mice is stable and is not altered by voluntary exercise (vol 37, pg 3725, 2017).* Journal of Cerebral Blood Flow and Metabolism, 2017. **37**(12): p. 3824-3824.

33. Harb, R., et al., *In vivo imaging of cerebral microvascular plasticity from birth to death.* J Cereb Blood Flow Metab, 2013. **33**(1): p. 146-56.

34. Schaffer, C.B., et al., *Two-photon imaging of cortical surface microvessels reveals a robust redistribution in blood flow after vascular occlusion.* PLoS Biol, 2006. **4**(2): p. e22.

35. Nishimura, N., et al., *Targeted insult to subsurface cortical blood vessels using ultrashort laser pulses: three models of stroke.* Nature Methods, 2006. **3**(2): p. 99-108.

36. Brown, W.R. and C.R. Thore, *Review: cerebral microvascular pathology in ageing and neurodegeneration.* Neuropathol Appl Neurobiol, 2011. **37**(1): p. 56-74.

37. Lange, C., et al., *Vascular endothelial growth factor: a neurovascular target in neurological diseases.* Nat Rev Neurol, 2016. **12**(8): p. 439-54.

38. Hill, J.M., et al., *Circulating endothelial progenitor cells, vascular function, and cardiovascular risk.* New England Journal of Medicine, 2003. **348**(7): p. 593-600.

39. Sobrino, T., et al., *The increase of circulating endothelial progenitor cells after acute ischemic stroke is associated with good outcome.* Stroke, 2007. **38**(10): p. 2759-2764.

40. Pires, P.W., et al., *The effects of hypertension on the cerebral circulation.* Am J Physiol Heart Circ Physiol, 2013. **304**(12): p. H1598-614.

41. Galvan, V. and K. Jin, *Neurogenesis in the aging brain.* Clin Interv Aging, 2007. **2**(4): p. 605-10.

42. Palmer, T.D., A.R. Willhoite, and F.H. Gage, *Vascular niche for adult hippocampal neurogenesis.* Journal of Comparative Neurology, 2000. **425**(4): p. 479-494.

43. Tavazoie, M., et al., *A specialized vascular niche for adult neural stem cells.* Cell stem cell, 2008. **3**(3): p. 279-288.

44. Kempermann, G., H. Song, and F.H. Gage, *Neurogenesis in the adult hippocampus.* Cold Spring Harbor perspectives in biology, 2015. **7**(9): p. a018812.

45. Cauli, B. and E. Hamel, *Revisiting the role of neurons in neurovascular coupling.* Frontiers in neuroenergetics, 2010. **2**.

46. Longden, T.A., et al., *Capillary K(+)-sensing initiates retrograde hyperpolarization to increase local cerebral blood flow.* Nat Neurosci, 2017. **20**(5): p. 717-726.

47. Hill, R.A., et al., *Regional blood flow in the normal and ischemic brain is controlled by arteriolar smooth muscle cell contractility and not by capillary pericytes.* Neuron, 2015. **87**(1): p. 95-110.

48. Kisler, K., et al., *Pericyte degeneration leads to neurovascular uncoupling and limits oxygen supply to brain.* Nat Neurosci, 2017. **20**(3): p. 406-416.

49. Cai, C., et al., *Stimulation-induced increases in cerebral blood flow and local capillary vasoconstriction depend on conducted vascular responses.* Proceedings of the National Academy of Sciences, 2018. **115**(25): p. E5796-E5804.

50. Kisler, K., et al., *Cerebral blood flow regulation and neurovascular dysfunction in Alzheimer disease.* Nat Rev Neurosci, 2017. **18**(7): p. 419-434.

51. Logothetis, N.K., et al., *Neurophysiological investigation of the basis of the fMRI signal.* Nature, 2001. **412**(6843): p. 150.

52. Blockley, N.P., et al., *A review of calibrated blood oxygenation level-dependent (BOLD) methods for the measurement of task-induced changes in brain oxygen metabolism.* NMR in Biomedicine, 2013. **26**(8): p. 987-1003.

53. Boynton, G.M., et al., *Linear systems analysis of functional magnetic resonance imaging in human V1.* J Neurosci, 1996. **16**(13): p. 4207-21.

54. Hoge, R.D., et al., *Investigation of BOLD signal dependence on cerebral blood flow and oxygen consumption: the deoxyhemoglobin dilution model.* Magnetic resonance in medicine, 1999. **42**(5): p. 849-863.

55. Ogawa, S., et al., *Brain magnetic resonance imaging with contrast dependent on blood oxygenation.* Proceedings of the National Academy of Sciences, 1990. **87**(24): p. 9868-9872.

56. Silva, A.C. and A.P. Koretsky, *Laminar specificity of functional MRI onset times during somatosensory stimulation in rat.* Proceedings of the National Academy of Sciences, 2002. **99**(23): p. 15182-15187.

57. Devor, A., et al., *Coupling of the cortical hemodynamic response to cortical and thalamic neuronal activity.* Proceedings of the National Academy of Sciences of the United States of America, 2005. **102**(10): p. 3822-3827.

58. Vigneau-Roy, N., et al., *Regional variations in vascular density correlate with resting-state and task-evoked blood oxygen level-dependent signal amplitude.* Human brain mapping, 2014. **35**(5): p. 1906-1920.

59. Black, J.E., A.M. Sirevaag, and W.T. Greenough, *Complex experience promotes capillary formation in young rat visual cortex.* Neuroscience letters, 1987. **83**(3): p. 351-355.

60. Sirevaag, A.M., et al., *Direct evidence that complex experience increases capillary branching and surface area in visual cortex of young rats.* Developmental Brain Research, 1988. **43**(2): p. 299-304.

61. Black, J.E., et al., *Learning causes synaptogenesis, whereas motor activity causes angiogenesis, in cerebellar cortex of adult rats.* Proceedings of the National Academy of Sciences, 1990. **87**(14): p. 5568-5572.

62. Wiesel, T.N. and D.H. Hubel, *Single-cell responses in striate cortex of kittens deprived of vision in one eye.* Journal of neurophysiology, 1963. **26**(6): p. 1003-1017.

63. Argandona, E. and J. Lafuente, *Effects of dark-rearing on the vascularization of the developmental rat visual cortex.* Brain research, 1996. **732**(1): p. 43-51.

64. Argandoña, E.G. and J.V. Lafuente, *Influence of visual experience deprivation on the postnatal development of the microvascular bed in layer IV of the rat visual cortex.* Brain research, 2000. **855**(1): p. 137-142.

65. Riddle, D.R., et al., *Differential metabolic and electrical activity in the somatic sensory cortex of juvenile and adult rats.* Journal of Neuroscience, 1993. **13**(10): p. 4193-4213.

66. Lacoste, B., et al., *Sensory-related neural activity regulates the structure of vascular networks in the cerebral cortex.* Neuron, 2014. **83**(5): p. 1117-1130.

67. LaManna, J.C., J.C. Chavez, and P. Pichiule, *Structural and functional adaptation to hypoxia in the rat brain.* J Exp Biol, 2004. **207**(Pt 18): p. 3163-9.

68. Park, H.Y., et al., *The effects of altitude/hypoxic training on oxygen delivery capacity of the blood and aerobic exercise capacity in elite athletes - a meta-analysis.* J Exerc Nutrition Biochem, 2016. **20**(1): p. 15-22.

69. Patt, S., et al., *Cerebral angiogenesis triggered by severe chronic hypoxia displays regional differences.* J Cereb Blood Flow Metab, 1997. **17**(7): p. 801-6.

70. Ogunshola, O.O., et al., *Neuronal VEGF expression correlates with angiogenesis in postnatal developing rat brain.* Brain Res Dev Brain Res, 2000. **119**(1): p. 139-53.

71. Daneman, R., et al., *Wnt/beta-catenin signaling is required for CNS, but not non-CNS, angiogenesis.* Proc Natl Acad Sci U S A, 2009. **106**(2): p. 641-6.

72. Saunders, N.R., et al., *Physiology and molecular biology of barrier mechanisms in the fetal and neonatal brain.* J Physiol, 2018.

73. Umans, R.A., et al., *CNS angiogenesis and barriergenesis occur simultaneously.* Dev Biol, 2017. **425**(2): p. 101-108.

74. Mollgard, K., et al., *Brain barriers and functional interfaces with sequential appearance of ABC efflux transporters during human development.* Sci Rep, 2017. **7**(1): p. 11603.

75. Daneman, R., et al., *Pericytes are required for blood-brain barrier integrity during embryogenesis.* Nature, 2010. **468**(7323): p. 562-6.

76. Alvarez, J.I., et al., *The Hedgehog pathway promotes blood-brain barrier integrity and CNS immune quiescence.* Science, 2011. **334**(6063): p. 1727-31.

77. Tsai, H.H., et al., *Oligodendrocyte precursors migrate along vasculature in the developing nervous system.* Science, 2016. **351**(6271): p. 379-84.

78. Sonntag, W.E., et al., *Regulation of Cerebrovascular Aging*, in *Brain Aging: Models, Methods, and Mechanisms*, D.R. Riddle, Editor. 2007: Boca Raton (FL).

79. Murugesan, N., et al., *Brain regional angiogenic potential at the neurovascular unit during normal aging.* Neurobiol Aging, 2012. **33**(5): p. 1004 e1-16.

80. Erdo, F., L. Denes, and E. de Lange, *Age-associated physiological and pathological changes at the blood-brain barrier: A review.* J Cereb Blood Flow Metab, 2017. **37**(1): p. 4-24.

81. Montagne, A., et al., *Blood-brain barrier breakdown in the aging human hippocampus.* Neuron, 2015. **85**(2): p. 296-302.

82. Goodall, E.F., et al., *Age-associated changes in the blood-brain barrier: comparative studies in human and mouse.* Neuropathol Appl Neurobiol, 2018. **44**(3): p. 328-340.

83. Lahteenvuo, J. and A. Rosenzweig, *Effects of aging on angiogenesis.* Circ Res, 2012. **110**(9): p. 1252-64.

84. Black, J.E., M. Polinsky, and W.T. Greenough, *Progressive failure of cerebral angiogenesis supporting neural plasticity in aging rats.* Neurobiol Aging, 1989. **10**(4): p. 353-8.

85. Gao, P., et al., *Attenuation of brain response to vascular endothelial growth factor-mediated angiogenesis and neurogenesis in aged mice.* Stroke, 2009. **40**(11): p. 3596-600.

86. Aanerud, J., et al., *Brain energy metabolism and blood flow differences in healthy aging.* J Cereb Blood Flow Metab, 2012. **32**(7): p. 1177-87.

87. Chen, J.J., H.D. Rosas, and D.H. Salat, *Age-associated reductions in cerebral blood flow are independent from regional atrophy.* Neuroimage, 2011. **55**(2): p. 468-78.

88. Parkes, L.M., et al., *Normal cerebral perfusion measurements using arterial spin labeling: reproducibility, stability, and age and gender effects.* Magn Reson Med, 2004. **51**(4): p. 736-43.

89. Sonntag, W.E., et al., *Decreases in cerebral microvasculature with age are associated with the decline in growth hormone and insulin-like growth factor 1.* Endocrinology, 1997. **138**(8): p. 3515-3520.

90. D'Esposito, M., et al., *The effect of normal aging on the coupling of neural activity to the bold hemodynamic response.* Neuroimage, 1999. **10**(1): p. 6-14.

91. Park, L., et al., *Nox2-derived reactive oxygen species mediate neurovascular dysregulation in the aging mouse brain.* J Cereb Blood Flow Metab, 2007. **27**(12): p. 1908-18.

92. Fabiani, M., et al., *Neurovascular coupling in normal aging: a combined optical, ERP and fMRI study.* Neuroimage, 2014. **85 Pt 1**: p. 592-607.

93. Tarantini, S., et al., *Impaired neurovascular coupling in aging and Alzheimer's disease: Contribution of astrocyte dysfunction and endothelial impairment to cognitive decline.* Exp Gerontol, 2017. **94**: p. 52-58.

94. Tarantini, S., et al., *Pharmacologically-induced neurovascular uncoupling is associated with cognitive impairment in mice.* J Cereb Blood Flow Metab, 2015. **35**(11): p. 1871-81.

95. D'Esposito, M., L.Y. Deouell, and A. Gazzaley, *Alterations in the BOLD fMRI signal with ageing and disease: a challenge for neuroimaging.* Nat Rev Neurosci, 2003. **4**(11): p. 863-72.

96. Grinband, J., et al., *BOLD neurovascular coupling does not change significantly with normal aging.* Hum Brain Mapp, 2017.

97. Ma, V.Y., L. Chan, and K.J. Carruthers, *Incidence, prevalence, costs, and impact on disability of common conditions requiring rehabilitation in the United States: stroke, spinal cord injury, traumatic brain injury, multiple sclerosis, osteoarthritis, rheumatoid arthritis, limb loss, and back pain.* Archives of physical medicine and rehabilitation, 2014. **95**(5): p. 986-995. e1.

98. Jiang, X., et al., *Blood-brain barrier dysfunction and recovery after ischemic stroke.* Prog Neurobiol, 2018. **163-164**: p. 144-171.

99. Kenney, K., et al., *Cerebral Vascular Injury in Traumatic Brain Injury.* Exp Neurol, 2016. **275 Pt 3**: p. 353-366.

100. Burke, J.F., et al., *Traumatic brain injury may be an independent risk factor for stroke.* Neurology, 2013. **81**(1): p. 33-9.

101. Gardner, R.C. and K. Yaffe, *Epidemiology of mild traumatic brain injury and neurodegenerative disease.* Mol Cell Neurosci, 2015. **66**(Pt B): p. 75-80.

102. Katan, M. and A. Luft, *Global Burden of Stroke.* Semin Neurol, 2018. **38**(2): p. 208-211.

103. Grau, A.J., et al., *Risk factors, outcome, and treatment in subtypes of ischemic stroke.* Stroke, 2001. **32**(11): p. 2559-2566.

104. Saver, J.L., *Time is brain--quantified.* Stroke, 2006. **37**(1): p. 263-6.

105. Lugo-Hernandez, E., et al., *3D visualization and quantification of microvessels in the whole ischemic mouse brain using solvent-based clearing and light sheet microscopy.* J Cereb Blood Flow Metab, 2017. **37**(10): p. 3355-3367.

106. Shih, A.Y., et al., *The smallest stroke: occlusion of one penetrating vessel leads to infarction and a cognitive deficit.* Nat Neurosci, 2013. **16**(1): p. 55-63.

107. Lai, T.W., S. Zhang, and Y.T. Wang, *Excitotoxicity and stroke: identifying novel targets for neuroprotection.* Prog Neurobiol, 2014. **115**: p. 157-88.

108. Croll, S.D. and S.J. Wiegand, *Vascular growth factors in cerebral ischemia.* Molecular neurobiology, 2001. **23**(2-3): p. 121-135.

109. Yang, Y. and G.A. Rosenberg, *Matrix metalloproteinases as therapeutic targets for stroke.* Brain Res, 2015. **1623**: p. 30-8.

110. Kontos, H.A., *Oxygen radicals in cerebral ischemia.* Stroke, 2001. **32**(11): p. 2712-2716.

111. Dávalos, A., et al., *Duration of glutamate release after acute ischemic stroke.* Stroke, 1997. **28**(4): p. 708-710.

112. Chen, Z.Q., et al., *The role of nitric oxide in stroke.* Med Gas Res, 2017. **7**(3): p. 194-203.

113. Tuttolomondo, A., et al., *Inflammatory cytokines in acute ischemic stroke.* Curr Pharm Des, 2008. **14**(33): p. 3574-89.

114. Brown, C.E., et al., *Extensive turnover of dendritic spines and vascular remodeling in cortical tissues recovering from stroke.* J Neurosci, 2007. **27**(15): p. 4101-9.

115. Yao, Y., *Basement membrane and stroke.* J Cereb Blood Flow Metab, 2018: p. 271678X18801467.

116. Gelderblom, M., et al., *Temporal and spatial dynamics of cerebral immune cell accumulation in stroke.* Stroke, 2009. **40**(5): p. 1849-57.

117. Hermann, D.M. and A. Zechariah, *Implications of vascular endothelial growth factor for postischemic neurovascular remodeling.* J Cereb Blood Flow Metab, 2009. **29**(10): p. 1620-43.

118. Adamczak, J. and M. Hoehn, *Poststroke angiogenesis, con: dark side of angiogenesis.* Stroke, 2015. **46**(5): p. e103-4.

119. Liu, J., et al., *Vascular remodeling after ischemic stroke: mechanisms and therapeutic potentials.* Progress in neurobiology, 2014. **115**: p. 138-156.

120. Yang, S., et al., *Diverse Functions and Mechanisms of Pericytes in Ischemic Stroke.* Curr Neuropharmacol, 2017. **15**(6): p. 892-905.

121. Okano, H., et al., *Regeneration of the central nervous system using endogenous repair mechanisms.* Journal of neurochemistry, 2007. **102**(5): p. 1459-1465.

122. Arai, K., et al., *Cellular mechanisms of neurovascular damage and repair after stroke.* Journal of child neurology, 2011. **26**(9): p. 1193-1198.

123. Salehi, A., J.H. Zhang, and A. Obenaus, *Response of the cerebral vasculature following traumatic brain injury.* J Cereb Blood Flow Metab, 2017. **37**(7): p. 2320-2339.

124. Shlosberg, D., et al., *Blood-brain barrier breakdown as a therapeutic target in traumatic brain injury.* Nat Rev Neurol, 2010. **6**(7): p. 393-403.

125. Park, E., et al., *An analysis of regional microvascular loss and recovery following two grades of fluid percussion trauma: a role for hypoxia-inducible factors in traumatic brain injury.* J Cereb Blood Flow Metab, 2009. **29**(3): p. 575-84.

126. Ostergaard, L., et al., *Capillary transit time heterogeneity and flow-metabolism coupling after traumatic brain injury.* J Cereb Blood Flow Metab, 2014. **34**(10): p. 1585-98.

127. Ho, K.M., et al., *Prognostic significance of blood-brain barrier disruption in patients with severe nonpenetrating traumatic brain injury requiring decompressive craniectomy.* J Neurosurg, 2014. **121**(3): p. 674-9.

128. Hay, J.R., et al., *Blood-Brain Barrier Disruption Is an Early Event That May Persist for Many Years After Traumatic Brain Injury in Humans.* J Neuropathol Exp Neurol, 2015. **74**(12): p. 1147-57.

129. Morgan, R., et al., *Neovascularization following traumatic brain injury: possible evidence for both angiogenesis and vasculogenesis.* Neurol Res, 2007. **29**(4): p. 375-81.

130. Zlokovic, B.V., *Neurovascular pathways to neurodegeneration in Alzheimer's disease and other disorders.* Nat Rev Neurosci, 2011. **12**(12): p. 723-38.

131. Sweeney, M.D., A.P. Sagare, and B.V. Zlokovic, *Blood-brain barrier breakdown in Alzheimer disease and other neurodegenerative disorders.* Nat Rev Neurol, 2018. **14**(3): p. 133-150.

132. Ujiie, M., et al., *Blood-brain barrier permeability precedes senile plaque formation in an Alzheimer disease model.* Microcirculation, 2003. **10**(6): p. 463-70.

133. Erickson, M.A. and W.A. Banks, *Blood-brain barrier dysfunction as a cause and consequence of Alzheimer's disease.* J Cereb Blood Flow Metab, 2013. **33**(10): p. 1500-13.

134. van de Haar, H.J., et al., *Blood-Brain Barrier Leakage in Patients with Early Alzheimer Disease.* Radiology, 2016. **281**(2): p. 527-535.

135. Suri, S., et al., *Reduced cerebrovascular reactivity in young adults carrying the APOE epsilon4 allele.* Alzheimers Dement, 2015. **11**(6): p. 648-57 e1.

136. Di Pardo, A., et al., *Impairment of blood-brain barrier is an early event in R6/2 mouse model of Huntington Disease.* Sci Rep, 2017. **7**: p. 41316.

137. Lim, R.G., et al., *Huntington's Disease iPSC-Derived Brain Microvascular Endothelial Cells Reveal WNT-Mediated Angiogenic and Blood-Brain Barrier Deficits.* Cell Rep, 2017. **19**(7): p. 1365-1377.

138. Chen, J.J., D.H. Salat, and H.D. Rosas, *Complex relationships between cerebral blood flow and brain atrophy in early Huntington's disease.* Neuroimage, 2012. **59**(2): p. 1043-51.

139. Cepeda-Prado, E., et al., *R6/2 Huntington's disease mice develop early and progressive abnormal brain metabolism and seizures.* J Neurosci, 2012. **32**(19): p. 6456-67.

140. Zhong, Z., et al., *ALS-causing SOD1 mutants generate vascular changes prior to motor neuron degeneration.* Nat Neurosci, 2008. **11**(4): p. 420-2.

141. Devos, D., et al., *Low levels of the vascular endothelial growth factor in CSF from early ALS patients.* Neurology, 2004. **62**(11): p. 2127-9.

142. Wyss-Coray, T., *Ageing, neurodegeneration and brain rejuvenation.* Nature, 2016. **539**(7628): p. 180-186.

143. Kaushik, S. and A.M. Cuervo, *Proteostasis and aging.* Nat Med, 2015. **21**(12): p. 1406-15.

144. Daulatzai, M.A., *Cerebral hypoperfusion and glucose hypometabolism: Key pathophysiological modulators promote neurodegeneration, cognitive impairment, and Alzheimer's disease.* J Neurosci Res, 2017. **95**(4): p. 943-972.

145. Yamada, M., *Cerebral amyloid angiopathy: emerging concepts.* J Stroke, 2015. **17**(1): p. 17-30.

146. Attems, J. and K.A. Jellinger, *The overlap between vascular disease and Alzheimer's disease--lessons from pathology.* BMC Med, 2014. **12**: p. 206.

147. Farkas, E., et al., *Pathological features of cerebral cortical capillaries are doubled in Alzheimer's disease and Parkinson's disease.* Acta Neuropathol, 2000. **100**(4): p. 395-402.

148. Thomas, T., S. Miners, and S. Love, *Post-mortem assessment of hypoperfusion of cerebral cortex in Alzheimer's disease and vascular dementia.* Brain, 2015. **138**(Pt 4): p. 1059-69.

149. Tarkowski, E., et al., *Increased intrathecal levels of the angiogenic factors VEGF and TGF-beta in Alzheimer's disease and vascular dementia.* Neurobiol Aging, 2002. **23**(2): p. 237-43.

150. Desai, B.S., et al., *Evidence of angiogenic vessels in Alzheimer's disease.* J Neural Transm (Vienna), 2009. **116**(5): p. 587-97.

151. Biron, K.E., et al., *Amyloid triggers extensive cerebral angiogenesis causing blood brain barrier permeability and hypervascularity in Alzheimer's disease.* PLoS One, 2011. **6**(8): p. e23789.

152. Paris, D., et al., *Inhibition of angiogenesis by Abeta peptides.* Angiogenesis, 2004. **7**(1): p. 75-85.

153. Boscolo, E., et al., *Beta amyloid angiogenic activity in vitro and in vivo.* Int J Mol Med, 2007. **19**(4): p. 581-7.

154. Austin, B.P., et al., *Effects of hypoperfusion in Alzheimer's disease.* J Alzheimers Dis, 2011. **26 Suppl 3**: p. 123-33.

155. Thambisetty, M., et al., *APOE epsilon4 genotype and longitudinal changes in cerebral blood flow in normal aging.* Arch Neurol, 2010. **67**(1): p. 93-8.

156. Cruz Hernandez, J.C., et al., *Neutrophil adhesion in brain capillaries reduces cortical blood flow and impairs memory function in Alzheimer's disease mouse models.* Nat Neurosci, 2019. **22**(3): p. 413-420.

157. Hunt, A., et al., *Reduced cerebral glucose metabolism in patients at risk for Alzheimer's disease.* Psychiatry Res, 2007. **155**(2): p. 147-54.

158. Tong, X.K., et al., *Age-dependent rescue by simvastatin of Alzheimer's disease cerebrovascular and memory deficits.* J Neurosci, 2012. **32**(14): p. 4705-15.

159. Love, S. and J.S. Miners, *Cerebral Hypoperfusion and the Energy Deficit in Alzheimer's Disease.* Brain Pathol, 2016. **26**(5): p. 607-17.

160. Tan, X.L., et al., *Partial eNOS deficiency causes spontaneous thrombotic cerebral infarction, amyloid angiopathy and cognitive impairment.* Mol Neurodegener, 2015. **10**: p. 24.

161. Poewe, W., et al., *Parkinson disease.* Nat Rev Dis Primers, 2017. **3**: p. 17013.

162. Guan, J., et al., *Vascular degeneration in Parkinson's disease.* Brain Pathol, 2013. **23**(2): p. 154-64.

163. Desai Bradaric, B., et al., *Evidence for angiogenesis in Parkinson's disease, incidental Lewy body disease, and progressive supranuclear palsy.* J Neural Transm (Vienna), 2012. **119**(1): p. 59-71.

164. Janelidze, S., et al., *Increased CSF biomarkers of angiogenesis in Parkinson disease.* Neurology, 2015. **85**(21): p. 1834-42.

165. Carvey, P.M., et al., *6-Hydroxydopamine-induced alterations in blood-brain barrier permeability.* Eur J Neurosci, 2005. **22**(5): p. 1158-68.

166. Gray, M.T. and J.M. Woulfe, *Striatal blood-brain barrier permeability in Parkinson's disease.* J Cereb Blood Flow Metab, 2015. **35**(5): p. 747-50.

167. Hsu, J.L., et al., *Regional CBF changes in Parkinson's disease: a correlation with motor dysfunction.* Eur J Nucl Med Mol Imaging, 2007. **34**(9): p. 1458-66.

168. Pienaar, I.S., et al., *Deep-brain stimulation associates with improved microvascular integrity in the subthalamic nucleus in Parkinson's disease.* Neurobiol Dis, 2015. **74**: p. 392-405.

169. Gondard, E., et al., *Rapid Modulation of Protein Expression in the Rat Hippocampus Following Deep Brain Stimulation of the Fornix.* Brain Stimul, 2015. **8**(6): p. 1058-64.

170. Zuccato, C., M. Valenza, and E. Cattaneo, *Molecular mechanisms and potential therapeutical targets in Huntington's disease.* Physiol Rev, 2010. **90**(3): p. 905-81.

171. Drouin-Ouellet, J., et al., *Cerebrovascular and blood-brain barrier impairments in Huntington's disease: Potential implications for its pathophysiology.* Ann Neurol, 2015. **78**(2): p. 160-77.

172. Lin, C.Y., et al., *Neurovascular abnormalities in humans and mice with Huntington's disease.* Exp Neurol, 2013. **250**: p. 20-30.

173. Hsiao, H.Y., et al., *Aberrant astrocytes impair vascular reactivity in Huntington disease.* Ann Neurol, 2015. **78**(2): p. 178-92.

174. Rodrigues, M.C., et al., *Neurovascular aspects of amyotrophic lateral sclerosis.* Int Rev Neurobiol, 2012. **102**: p. 91-106.

175. Oosthuyse, B., et al., *Deletion of the hypoxia-response element in the vascular endothelial growth factor promoter causes motor neuron degeneration.* Nat Genet, 2001. **28**(2): p. 131-8.

176. Lambrechts, D., et al., *VEGF is a modifier of amyotrophic lateral sclerosis in mice and humans and protects motoneurons against ischemic death.* Nat Genet, 2003. **34**(4): p. 383-94.

177. Kew, J.J., et al., *Cortical function in amyotrophic lateral sclerosis. A positron emission tomography study.* Brain, 1993. **116 (Pt 3)**: p. 655-80.

178. Robberecht, W. and T. Philips, *The changing scene of amyotrophic lateral sclerosis.* Nat Rev Neurosci, 2013. **14**(4): p. 248-64.

179. Ilieva, H., M. Polymenidou, and D.W. Cleveland, *Non-cell autonomous toxicity in neurodegenerative disorders: ALS and beyond.* J Cell Biol, 2009. **187**(6): p. 761-72.

180. Campisi, M., et al., *3D self-organized microvascular model of the human blood-brain barrier with endothelial cells, pericytes and astrocytes.* Biomaterials, 2018. **180**: p. 117-129.

181. Linville, R.M., et al., *Human iPSC-derived blood-brain barrier microvessels: validation of barrier function and endothelial cell behavior.* Biomaterials, 2018. **190-191**: p. 24-37.

182.   Pardridge, W.M., *Drug transport across the blood-brain barrier.* J Cereb Blood Flow Metab, 2012. **32**(11): p. 1959-72.

183.   Wong, A.D., et al., *The blood-brain barrier: an engineering perspective.* Frontiers in Neuroengineering, 2013. **6**.

184.   Abbott, N.J., et al., *Structure and function of the blood-brain barrier.* Neurobiol Dis, 2010. **37**(1): p. 13-25.

185.   Watase, K. and H.Y. Zoghbi, *Modelling brain diseases in mice: the challenges of design and analysis.* Nat Rev Genet, 2003. **4**(4): p. 296-307.

186.   Cho, H., et al., *Three-Dimensional Blood-Brain Barrier Model for in vitro Studies of Neurovascular Pathology.* Sci Rep, 2015. **5**: p. 15222.

187.   Herland, A., et al., *Distinct Contributions of Astrocytes and Pericytes to Neuroinflammation Identified in a 3D Human Blood-Brain Barrier on a Chip.* PLoS One, 2016. **11**(3): e0150360.

188.   Partyka, P.P., et al., *Mechanical stress regulates transport in a compliant 3D model of the blood-brain barrier.* Biomaterials, 2017. **115**: p. 30-39.

189.   Adriani, G., et al., *A 3D neurovascular microfluidic model consisting of neurons, astrocytes and cerebral endothelial cells as a blood-brain barrier.* Lab Chip, 2017. **17**(3): p. 448-459.

190.   Butt, A.M., H.C. Jones, and N.J. Abbott, *Electrical resistance across the blood-brain barrier in anaesthetized rats: a developmental study.* J Physiol, 1990. **429**: p. 47-62.

191.   Smith, Q.R. and S.I. Rapoport, *Cerebrovascular permeability coefficients to sodium, potassium, and chloride.* J Neurochem, 1986. **46**(6): p. 1732-42.

192.   Butt, A.M. and H.C. Jones, *Effect of histamine and antagonists on electrical resistance across the blood-brain barrier in rat brain-surface microvessels.* Brain Res, 1992. **569**(1): p. 100-5.

193.   Crone, C. and S.P. Olesen, *Electrical resistance of brain microvascular endothelium.* Brain Res, 1982. **241**(1): p. 49-55.

194.   Lippmann, E.S., et al., *Derivation of blood-brain barrier endothelial cells from human pluripotent stem cells.* Nat Biotechnol, 2012. **30**(8): p. 783-91.

195.   Lippmann, E.S., et al., *A retinoic acid-enhanced, multicellular human blood-brain barrier model derived from stem cell sources.* Sci Rep, 2014. **4**: p. 4160.

196.   Katt, M.E., et al., *Human Brain Microvascular Endothelial Cells Derived from the BC1 iPS Cell Line Exhibit a Blood-Brain Barrier Phenotype.* PLoS One, 2016. **11**(4): p. e0152105.

197.   Qian, T., et al., *Directed differentiation of human pluripotent stem cells to blood-brain barrier endothelial cells.* Sci Adv, 2017. **3**(11): p. e1701679.

198.   Katt, M.E., et al., *Functional brain-specific microvessels from iPSC-derived human brain microvascular endothelial cells: the role of matrix composition on monolayer formation.* Fluids Barriers CNS, 2018. **15**(1): p. 7.

199.   Turitto, V.T., *Blood viscosity, mass transport, and thrombogenesis.* Prog Hemost Thromb, 1982. **6**: p. 139-77.

200.   Kamiya, A., R. Bukhari, and T. Togawa, *Adaptive regulation of wall shear stress optimizing vascular tree function.* Bulletin of Mathematical Biology, 1984. **46**(1): p. 127-137.

201.   Koutsiaris, A.G., et al., *Volume flow and wall shear stress quantification in the human conjunctival capillaries and post-capillary venules in vivo.* Biorheology, 2007. **44**(5-6): p. 375-86.

202. Santisakultarm, T.P., et al., *In vivo two-photon excited fluorescence microscopy reveals cardiac- and respiration-dependent pulsatile blood flow in cortical blood vessels in mice.* Am J Physiol Heart Circ Physiol, 2012. **302**(7): p. H1367-77.

203. Takeshita, Y. and R.M. Ransohoff, *Inflammatory cell trafficking across the blood-brain barrier: chemokine regulation and in vitro models.* Immunological Reviews, 2012. **248**: p. 228-239.

204. Owens, T., I. Bechmann, and B. Engelhardt, *Perivascular spaces and the two steps to neuroinflammation.* J Neuropathol Exp Neurol, 2008. **67**(12): p. 1113-21.

205. Banks, W.A. and M.A. Erickson, *The blood-brain barrier and immune function and dysfunction.* Neurobiol Dis, 2010. **37**(1): p. 26-32.

206. Kristensson, K., et al., *African trypanosome infections of the nervous system: Parasite entry and effects on sleep and synaptic functions.* Progress in Neurobiology, 2010. **91**(2): p. 152-171.

207. Spindler, K.R. and T.H. Hsu, *Viral disruption of the blood brain barrier.* Trends in Microbiology, 2012. **20**(6): p. 282-290.

208. Dando, S.J., et al., *Pathogens Penetrating the Central Nervous System: Infection Pathways and the Cellular and Molecular Mechanisms of Invasion.* Clinical Microbiology Reviews, 2014. **27**(4): p. 691-726.

209. Bang, S., et al., *A Low Permeability Microfluidic Blood-Brain Barrier Platform with Direct Contact between Perfusable Vascular Network and Astrocytes.* Sci Rep, 2017. **7**(1): p. 8083.

210. Chou, B.K., et al., *Efficient human iPS cell derivation by a non-integrating plasmid from blood cells with unique epigenetic and gene expression signatures.* Cell Res, 2011. **21**(3): p. 518-29.

211. Mahairaki, V., et al., *Induced pluripotent stem cells from familial Alzheimer's disease patients differentiate into mature neurons with amyloidogenic properties.* Stem Cells Dev, 2014. **23**(24): p. 2996-3010.

212. Wilson, H.K., et al., *Cryopreservation of Brain Endothelial Cells Derived from Human Induced Pluripotent Stem Cells Is Enhanced by Rho-Associated Coiled Coil-Containing Kinase Inhibition.* Tissue Eng Part C Methods, 2016. **22**(12): p. 1085-1094.

213. Wong, K.H., J.G. Truslow, and J. Tien, *The role of cyclic AMP in normalizing the function of engineered human blood microvessels in microfluidic collagen gels.* Biomaterials, 2010. **31**(17): p. 4706-14.

214. Leung, A.D., K.H. Wong, and J. Tien, *Plasma expanders stabilize human microvessels in microfluidic scaffolds.* J Biomed Mater Res A, 2012. **100**(7): p. 1815-22.

215. Linville, R.M., et al., *Physical and Chemical Signals That Promote Vascularization of Capillary-Scale Channels.* Cell Mol Bioeng, 2016. **9**(1): p. 73-84.

216. Huxley, V.H., F.E. Curry, and R.H. Adamson, *Quantitative fluorescence microscopy on single capillaries: alpha-lactalbumin transport.* Am J Physiol, 1987. **252**(1 Pt 2): p. H188-97.

217. Chrobak, K.M., D.R. Potter, and J. Tien, *Formation of perfused, functional microvascular tubes in vitro.* Microvasc Res, 2006. **71**(3): p. 185-96.

218. Bogorad, M.I. and P.C. Searson, *Real-time imaging and quantitative analysis of doxorubicin transport in a perfusable microvessel platform.* Integr Biol (Camb), 2016. **8**(9): p. 976-84.

219. DeStefano, J.G., et al., *Real-time quantification of endothelial response to shear stress and vascular modulators.* Integr Biol (Camb), 2017. **9**(4): p. 362-374.

220. DeStefano, J.G., et al., *Effect of shear stress on iPSC-derived human brain microvascular endothelial cells (dhBMECs).* Fluids Barriers CNS, 2017. **14**(1): p. 20.

221. Reinitz, A., et al., *Human brain microvascular endothelial cells resist elongation due to shear stress.* Microvasc Res, 2015. **99**: p. 8-18.

222. Bogorad, M.I., et al., *Tissue-engineered 3D microvessel and capillary network models for the study of vascular phenomena.* Microcirculation, 2017. **24**(5): p. e12360.

223. Muskhelishvili, L., et al., *Evaluation of cell proliferation in rat tissues with BrdU, PCNA, Ki-67 (MIB-5) immunohistochemistry and in situ hybridization for histone mRNA.* Journal of Histochemistry & Cytochemistry, 2003. **51**(12): p. 1681-1688.

224. Cosolo, W.C., et al., *Blood-brain barrier disruption using mannitol: time course and electron microscopy studies.* Am J Physiol, 1989. **256**(2 Pt 2): p. R443-7.

225. Easton, A.S., M.H. Sarker, and P.A. Fraser, *Two components of blood-brain barrier disruption in the rat.* J Physiol, 1997. **503 (Pt 3)**: p. 613-23.

226. Saunders, N.R., et al., *The rights and wrongs of blood-brain barrier permeability studies: a walk through 100 years of history.* Frontiers in Neuroscience, 2014. **8**.

227. Olsson, Y., et al., *Fluorescein labelled dextrans as tracers for vascular permeability studies in the nervous system.* Acta Neuropathol, 1975. **33**(1): p. 45-50.

228. Yuan, W., et al., *Non-invasive measurement of solute permeability in cerebral microvessels of the rat.* Microvasc Res, 2009. **77**(2): p. 166-73.

229. Shi, L., et al., *Quantification of blood-brain barrier solute permeability and brain transport by multiphoton microscopy.* J Biomech Eng, 2014. **136**(3): p. 031005.

230. Noumbissi, M.E., B. Galasso, and M.F. Stins, *Brain vascular heterogeneity: implications for disease pathogenesis and design of in vitro blood-brain barrier models.* Fluids Barriers CNS, 2018. **15**(1): p. 12.

231. Daneman, R., et al., *Pericytes are required for blood-brain barrier integrity during embryogenesis.* Nature, 2010. **468**(7323): p. 562-566.

232. Nakagawa, S., et al., *A new blood-brain barrier model using primary rat brain endothelial cells, pericytes and astrocytes.* Neurochemistry International, 2009. **54**(3-4): p. 253-263.

233. Nakagawa, S., et al., *Pericytes from brain microvessels strengthen the barrier integrity in primary cultures of rat brain endothelial cells.* Cellular and Molecular Neurobiology, 2007. **27**(6): p. 687-694.

234. Siddharthan, V., et al., *Human astrocytes/astrocyte-conditioned medium and shear stress enhance the barrier properties of human brain microvascular endothelial cells.* Brain Research, 2007. **1147**: p. 39-50.

235. Thomsen, L.B., A. Burkhart, and T. Moos, *A Triple Culture Model of the Blood-Brain Barrier Using Porcine Brain Endothelial cells, Astrocytes and Pericytes.* Plos One, 2015. **10**(8).

236. Malina, K.C.K., I. Cooper, and V.I. Teichberg, *Closing the gap between the in-vivo and in-vitro blood-brain barrier tightness.* Brain Research, 2009. **1284**: p. 12-21.

237. Hatherell, K., et al., *Development of a three-dimensional, all-human in vitro model of the blood-brain barrier using mono-, co-, and tri-cultivation Transwell models.* Journal of Neuroscience Methods, 2011. **199**(2): p. 223-229.

238. Hobson, B. and J. Denekamp, *Endothelial proliferation in tumours and normal tissues: continuous labelling studies.* British journal of cancer, 1984. **49**(4): p. 405.

239. Harb, R., et al., *In vivo imaging of cerebral microvascular plasticity from birth to death.* Journal of Cerebral Blood Flow & Metabolism, 2013. **33**(1): p. 146-156.

240. Tannock, I.F. and S. Hayashi, *The proliferation of capillary endothelial cells.* Cancer research, 1972. **32**(1): p. 77-82.

241. Spaet, T. and I. Lejnieks, *Mitotic activity of rabbit blood vessels.* Proceedings of the Society for Experimental Biology and Medicine, 1967. **125**(4): p. 1197-1201.

242. Ye, M., et al., *Brain microvascular endothelial cells resist elongation due to curvature and shear stress.* Sci Rep, 2014. **4**: p. 4681.

243. Tilling, T., et al., *Expression and adhesive properties of basement membrane proteins in cerebral capillary endothelial cell cultures.* Cell Tissue Res, 2002. **310**(1): p. 19-29.

244. Tilling, T., et al., *Basement membrane proteins influence brain capillary endothelial barrier function in vitro.* J Neurochem, 1998. **71**(3): p. 1151-7.

245. International Transporter, C., et al., *Membrane transporters in drug development.* Nat Rev Drug Discov, 2010. **9**(3): p. 215-36.

246. Loscher, W. and H. Potschka, *Blood-brain barrier active efflux transporters: ATP-binding cassette gene family.* NeuroRx, 2005. **2**(1): p. 86-98.

247. Callaghan, R., F. Luk, and M. Bebawy, *Inhibition of the multidrug resistance P-glycoprotein: time for a change of strategy?* Drug Metab Dispos, 2014. **42**(4): p. 623-31.

248. Syvanen, S., et al., *Species differences in blood-brain barrier transport of three positron emission tomography radioligands with emphasis on P-glycoprotein transport.* Drug Metab Dispos, 2009. **37**(3): p. 635-43.

249. Warren, M.S., et al., *Comparative gene expression profiles of ABC transporters in brain microvessel endothelial cells and brain in five species including human.* Pharmacol Res, 2009. **59**(6): p. 404-13.

250. Bauer, M., et al., *Pgp-mediated interaction between (R)-[11C]verapamil and tariquidar at the human blood-brain barrier: a comparison with rat data.* Clin Pharmacol Ther, 2012. **91**(2): p. 227-33.

251. Bauer, M., et al., *Pharmacokinetics of single ascending doses of the P-glycoprotein inhibitor tariquidar in healthy subjects.* Pharmacology, 2013. **91**(1-2): p. 12-9.

252. Bauer, M., et al., *Approaching complete inhibition of P-glycoprotein at the human blood-brain barrier: an (R)-[11C]verapamil PET study.* J Cereb Blood Flow Metab, 2015. **35**(5): p. 743-6.

253. Kreisl, W.C., et al., *Increased permeability-glycoprotein inhibition at the human blood-brain barrier can be safely achieved by performing PET during peak plasma concentrations of tariquidar.* J Nucl Med, 2015. **56**(1): p. 82-7.

254. Ting, C.Y., et al., *Concurrent blood-brain barrier opening and local drug delivery using drug-carrying microbubbles and focused ultrasound for brain glioma treatment.* Biomaterials, 2012. **33**(2): p. 704-12.

255. Neuhaus, W., et al., *Reversible opening of the blood-brain barrier by claudin-5-binding variants of Clostridium perfringens enterotoxin's claudin-binding domain.* Biomaterials, 2018. **161**: p. 129-143.

256. Park, T.E., et al., *Enhanced BBB permeability of osmotically active poly(mannitol-co-PEI) modified with rabies virus glycoprotein via selective stimulation of caveolar endocytosis for RNAi therapeutics in Alzheimer's disease.* Biomaterials, 2015. **38**: p. 61-71.

257. Jia, G., et al., *NRP-1 targeted and cargo-loaded exosomes facilitate simultaneous imaging and therapy of glioma in vitro and in vivo.* Biomaterials, 2018. **178**: p. 302-316.

258. Diringer, M.N., *New trends in hyperosmolar therapy?* Curr Opin Crit Care, 2013. **19**(2): p. 77-82.

259. Rapoport, S.I., *Osmotic opening of the blood-brain barrier: principles, mechanism, and therapeutic applications.* Cell Mol Neurobiol, 2000. **20**(2): p. 217-30.

260. Gonzales-Portillo, G.S., et al., *Mannitol-enhanced delivery of stem cells and their growth factors across the blood-brain barrier.* Cell Transplant, 2014. **23**(4-5): p. 531-9.

261. Foley, C.P., et al., *Intra-arterial delivery of AAV vectors to the mouse brain after mannitol mediated blood brain barrier disruption.* J Control Release, 2014. **196**: p. 71-78.

262. Burkhardt, J.K., et al., *Intra-arterial delivery of bevacizumab after blood-brain barrier disruption for the treatment of recurrent glioblastoma: progression-free survival and overall survival.* World Neurosurg, 2012. **77**(1): p. 130-4.

263. Janowski, M., P. Walczak, and M.S. Pearl, *Predicting and optimizing the territory of blood-brain barrier opening by superselective intra-arterial cerebral infusion under dynamic susceptibility contrast MRI guidance.* J Cereb Blood Flow Metab, 2016. **36**(3): p. 569-75.

264. Zylber-Katz, E., et al., *Pharmacokinetics of methotrexate in cerebrospinal fluid and serum after osmotic blood-brain barrier disruption in patients with brain lymphoma.* Clin Pharmacol Ther, 2000. **67**(6): p. 631-41.

265. Joshi, S., et al., *Inconsistent blood brain barrier disruption by intraarterial mannitol in rabbits: implications for chemotherapy.* J Neurooncol, 2011. **104**(1): p. 11-9.

266. Janowski, M., P. Walczak, and M.S. Pearl, *Predicting and optimizing the territory of blood–brain barrier opening by superselective intra-arterial cerebral infusion under dynamic susceptibility contrast MRI guidance.* Journal of Cerebral Blood Flow & Metabolism, 2016. **36**(3): p. 569-575.

267. Cucullo, L., et al., *A dynamic in vitro BBB model for the study of immune cell trafficking into the central nervous system.* J Cereb Blood Flow Metab, 2011. **31**(2): p. 767-77.

268. Muldoon, L.L., et al., *Comparison of intracerebral inoculation and osmotic blood-brain barrier disruption for delivery of adenovirus, herpesvirus, and iron oxide particles to normal rat brain.* Am J Pathol, 1995. **147**(6): p. 1840-51.

269. Granath, K.A., *Solution properties of branched dextran.* Journal of Colloid Science, 1958. **31**: p. 308-328.

270. Coisne, C., R. Lyck, and B. Engelhardt, *Live cell imaging techniques to study T cell trafficking across the blood-brain barrier in vitro and in vivo.* Fluids Barriers CNS, 2013. **10**(1): p. 7.

271. Mahad, D., et al., *Modulating CCR2 and CCL2 at the blood-brain barrier: relevance for multiple sclerosis pathogenesis.* Brain, 2006. **129**(Pt 1): p. 212-23.

272. Irimia, D. and X. Wang, *Inflammation-on-a-Chip: Probing the Immune System Ex Vivo.* Trends Biotechnol, 2018.

273. Prinz, M. and J. Priller, *The role of peripheral immune cells in the CNS in steady state and disease.* Nat Neurosci, 2017. **20**(2): p. 136-144.

274. Ley, K., et al., *Getting to the site of inflammation: the leukocyte adhesion cascade updated.* Nat Rev Immunol, 2007. **7**(9): p. 678-89.

275. Steiner, O., et al., *Differential roles for endothelial ICAM-1, ICAM-2, and VCAM-1 in shear-resistant T cell arrest, polarization, and directed crawling on blood-brain barrier endothelium.* J Immunol, 2010. **185**(8): p. 4846-55.

276. Deli, M.A., et al., *Exposure of tumor necrosis factor-alpha to luminal membrane of bovine brain capillary endothelial cells cocultured with astrocytes induces a delayed increase of permeability and cytoplasmic stress fiber formation of actin.* J Neurosci Res, 1995. **41**(6): p. 717-26.

277. Capaldo, C.T. and A. Nusrat, *Cytokine regulation of tight junctions.* Biochim Biophys Acta, 2009. **1788**(4): p. 864-71.

278. Mark, K.S. and D.W. Miller, *Increased permeability of primary cultured brain microvessel endothelial cell monolayers following TNF-alpha exposure.* Life Sci, 1999. **64**(21): p. 1941-53.

279. Lopez-Ramirez, M.A., et al., *Role of caspases in cytokine-induced barrier breakdown in human brain endothelial cells.* J Immunol, 2012. **189**(6): p. 3130-9.

280. Mayhan, W.G., *Cellular mechanisms by which tumor necrosis factor-alpha produces disruption of the blood-brain barrier.* Brain Res, 2002. **927**(2): p. 144-52.

281. Varatharaj, A. and I. Galea, *The blood-brain barrier in systemic inflammation.* Brain Behav Immun, 2017. **60**: p. 1-12.

282. Linville, R.M., et al., *Modeling hyperosmotic blood-brain barrier opening within human tissue-engineered in vitro brain microvessels.* J Cereb Blood Flow Metab, 2019: p. 271678X19867980.

283. Pardridge, W.M., *The blood-brain barrier: bottleneck in brain drug development.* NeuroRx, 2005. **2**(1): p. 3-14.

284. Steed, E., M.S. Balda, and K. Matter, *Dynamics and functions of tight junctions.* Trends Cell Biol, 2010. **20**(3): p. 142-9.

285. Salama, N.N., N.D. Eddington, and A. Fasano, *Tight junction modulation and its relationship to drug delivery.* Adv Drug Deliv Rev, 2006. **58**(1): p. 15-28.

286. Joshi, S., P.M. Meyers, and E. Ornstein, *Intracarotid delivery of drugs: the potential and the pitfalls.* Anesthesiology, 2008. **109**(3): p. 543-64.

287. Rapoport, S.I., et al., *Quantitative aspects of reversible osmotic opening of the blood-brain barrier.* Am J Physiol, 1980. **238**(5): p. R421-31.

288. Rapoport, S.I., M. Hori, and I. Klatzo, *Reversible osmotic opening of the blood-brain barrier.* Science, 1971. **173**(4001): p. 1026-8.

289. Neuwelt, E.A. and S.I. Rapoport, *Modification of the blood-brain barrier in the chemotherapy of malignant brain tumors.* Fed Proc, 1984. **43**(2): p. 214-9.

290. Neuwelt, E.A., et al., *Therapeutic efficacy of multiagent chemotherapy with drug delivery enhancement by blood-brain barrier modification in glioblastoma.* Neurosurgery, 1986. **19**(4): p. 573-82.

291. Chakraborty, S., et al., *Superselective intraarterial cerebral infusion of cetuximab after osmotic blood/brain barrier disruption for recurrent malignant glioma: phase I study.* J Neurooncol, 2016. **128**(3): p. 405-15.

292. Lesniak, W.G., et al., *PET imaging of intra-arterial (89)Zr bevacizumab in mice with and without osmotic opening of the blood-brain barrier: distinct advantage of intra-arterial delivery.* J Nucl Med, 2018.

293. Choi, C., et al., *Additional increased effects of mannitol-temozolomide combined treatment on blood-brain barrier permeability.* Biochem Biophys Res Commun, 2018. **497**(2): p. 769-775.

294. Siegal, T., et al., *In vivo assessment of the window of barrier opening after osmotic blood-brain barrier disruption in humans.* J Neurosurg, 2000. **92**(4): p. 599-605.

295. Chu, C., et al., *Real-Time MRI Guidance for Reproducible Hyperosmolar Opening of the Blood-Brain Barrier in Mice.* Front Neurol, 2018. **9**: p. 921.

296. Zawadzki, M., et al., *Real-time MRI guidance for intra-arterial drug delivery in a patient with a brain tumor: technical note.* BMJ Case Rep, 2019. **12**(1).

297. Weed L.H., M.P.S., *Pressure changes in cerebrospinal fluid following injections of solutions of various concentrations.* Am J Physiol 1919. **48**: p. 512–530.

298. Linville, R.M., et al., *Long-Term Cryopreservation Preserves Blood-Brain Barrier Phenotype of iPSC-Derived Brain Microvascular Endothelial Cells and Three-Dimensional Microvessels.* Mol Pharm, 2020. **17**(9): p. 3425-3434.

299. Kreitzer, F.R., et al., *A robust method to derive functional neural crest cells from human pluripotent stem cells.* Am J Stem Cells, 2013. **2**(2): p. 119-31.

300. Linville, R.M., et al., *Human iPSC-derived blood-brain barrier microvessels: validation of barrier function and endothelial cell behavior.* Biomaterials, 2019. **190-191**: p. 24-37.

301. Cuenod, C.A. and D. Balvay, *Perfusion and vascular permeability: basic concepts and measurement in DCE-CT and DCE-MRI.* Diagn Interv Imaging, 2013. **94**(12): p. 1187-204.

302. Klumperman, J. and G. Raposo, *The complex ultrastructure of the endolysosomal system.* Cold Spring Harb Perspect Biol, 2014. **6**(10): p. a016857.

303. Chen, B., C. Co, and C.C. Ho, *Cell shape dependent regulation of nuclear morphology.* Biomaterials, 2015. **67**: p. 129-36.

304. Reinehr, R., et al., *Hyperosmolarity triggers CD95 membrane trafficking and sensitizes rat hepatocytes toward CD95L-induced apoptosis.* Hepatology, 2002. **36**(3): p. 602-14.

305. Luo, L., D.Q. Li, and S.C. Pflugfelder, *Hyperosmolarity-induced apoptosis in human corneal epithelial cells is mediated by cytochrome c and MAPK pathways.* Cornea, 2007. **26**(4): p. 452-60.

306. Pazgal, I., et al., *Expression of basic fibroblast growth factor is associated with poor outcome in non-Hodgkin's lymphoma.* Br J Cancer, 2002. **86**(11): p. 1770-5.

307. Song, B.W., et al., *Enhanced neuroprotective effects of basic fibroblast growth factor in regional brain ischemia after conjugation to a blood-brain barrier delivery vector.* J Pharmacol Exp Ther, 2002. **301**(2): p. 605-10.

308. Wang, Z.G., et al., *bFGF Protects Against Blood-Brain Barrier Damage Through Junction Protein Regulation via PI3K-Akt-Rac1 Pathway Following Traumatic Brain Injury.* Mol Neurobiol, 2016. **53**(10): p. 7298-7311.

309. Huang, B., et al., *Fibroblast growth factors preserve blood-brain barrier integrity through RhoA inhibition after intracerebral hemorrhage in mice.* Neurobiol Dis, 2012. **46**(1): p. 204-14.

310. Wu, F., et al., *Acid fibroblast growth factor preserves blood-brain barrier integrity by activating the PI3K-Akt-Rac1 pathway and inhibiting RhoA following traumatic brain injury.* Am J Transl Res, 2017. **9**(3): p. 910-925.

311. Klusmeier, N., H.J. Schnittler, and J. Seebach, *A Novel Microscopic Assay Reveals Heterogeneous Regulation of Local Endothelial Barrier Function.* Biophys J, 2019.

312. Krueger, M., et al., *Blood-brain barrier breakdown after embolic stroke in rats occurs without ultrastructural evidence for disrupting tight junctions.* PLoS One, 2013. **8**(2): p. e56419.

313. Krueger, M., et al., *Endothelial edema precedes blood-brain barrier breakdown in early time points after experimental focal cerebral ischemia.* Acta Neuropathol Commun, 2019. **7**(1): p. 17.

314. Wang, M., J. Etu, and S. Joshi, *Enhanced disruption of the blood brain barrier by intracarotid mannitol injection during transient cerebral hypoperfusion in rabbits.* J Neurosurg Anesthesiol, 2007. **19**(4): p. 249-56.

315. Shimizu, F., et al., *Peripheral nerve pericytes modify the blood-nerve barrier function and tight junctional molecules through the secretion of various soluble factors.* J Cell Physiol, 2011. **226**(1): p. 255-66.

316. Ikeshima-Kataoka, H. and M. Yasui, *Correlation between astrocyte activity and recovery from blood-brain barrier breakdown caused by brain injury.* Neuroreport, 2016. **27**(12): p. 894-900.

317. Jeong, J.Y., et al., *Functional and developmental analysis of the blood-brain barrier in zebrafish.* Brain Res Bull, 2008. **75**(5): p. 619-28.

318. Park, T.E., et al., *Hypoxia-enhanced Blood-Brain Barrier Chip recapitulates human barrier function and shuttling of drugs and antibodies.* Nat Commun, 2019. **10**(1): p. 2621.

319. Cucullo, L., et al., *A new dynamic in vitro modular capillaries-venules modular system: cerebrovascular physiology in a box.* BMC Neurosci, 2013. **14**: p. 18.

320. Jamieson, J.J., et al., *Role of iPSC-derived pericytes on barrier function of iPSC-derived brain microvascular endothelial cells in 2D and 3D.* Fluids Barriers CNS, 2019. **16**(1): p. 15.

321. Liu, Q., et al., *Experimental chronic cerebral hypoperfusion results in decreased pericyte coverage and increased blood-brain barrier permeability in the corpus callosum.* J Cereb Blood Flow Metab, 2017: p. 271678X17743670.

322. Watkins, S., et al., *Disruption of astrocyte-vascular coupling and the blood-brain barrier by invading glioma cells.* Nat Commun, 2014. **5**: p. 4196.

323. Linville, R.M., et al., *Three-dimensional induced pluripotent stem-cell models of human brain angiogenesis.* Microvasc Res, 2020. **132**: p. 104042.

324. Nowak-Sliwinska, P., et al., *Consensus guidelines for the use and interpretation of angiogenesis assays.* Angiogenesis, 2018. **21**(3): p. 425-532.

325. Anasooya Shaji, C., et al., *The Tri-phasic Role of Hydrogen Peroxide in Blood-Brain Barrier Endothelial cells.* Sci Rep, 2019. **9**(1): p. 133.

326. Luo, J., et al., *Hypoxia induces angiogenic factors in brain microvascular endothelial cells.* Microvasc Res, 2012. **83**(2): p. 138-45.

327. Nakatsu, M.N. and C.C. Hughes, *An optimized three-dimensional in vitro model for the analysis of angiogenesis.* Methods Enzymol, 2008. **443**: p. 65-82.

328. Grifno, G.N., et al., *Tissue-engineered blood-brain barrier models via directed differentiation of human induced pluripotent stem cells.* Sci Rep, 2019. **9**(1): p. 13957.

329. Thomsen, M.S., L.J. Routhe, and T. Moos, *The vascular basement membrane in the healthy and pathological brain.* J Cereb Blood Flow Metab, 2017. **37**(10): p. 3300-3317.

330. O'Brown, N.M., S.J. Pfau, and C. Gu, *Bridging barriers: a comparative look at the blood-brain barrier across organisms.* Genes Dev, 2018. **32**(7-8): p. 466-478.

331. Katt, M.E., et al., *The role of mutations associated with familial neurodegenerative disorders on blood-brain barrier function in an iPSC model.* Fluids Barriers CNS, 2019. **16**(1): p. 20.

332. Vatine, G.D., et al., *Human iPSC-Derived Blood-Brain Barrier Chips Enable Disease Modeling and Personalized Medicine Applications.* Cell Stem Cell, 2019. **24**(6): p. 995-1005 e6.

333. Workman, M.J. and C.N. Svendsen, *Recent advances in human iPSC-derived models of the blood-brain barrier.* Fluids Barriers CNS, 2020. **17**(1): p. 30.

334. Sabbagh, M.F. and J. Nathans, *A genome-wide view of the de-differentiation of central nervous system endothelial cells in culture.* Elife, 2020. **9**.

335. Helms, H.C., et al., *In vitro models of the blood-brain barrier: An overview of commonly used brain endothelial cell culture models and guidelines for their use.* J Cereb Blood Flow Metab, 2016. **36**(5): p. 862-90.

336. Lee, S., et al., *3D brain angiogenesis model to reconstitute functional human blood-brain barrier in vitro.* Biotechnol Bioeng, 2019.

337. Gold, K., A.K. Gaharwar, and A. Jain, *Emerging trends in multiscale modeling of vascular pathophysiology: Organ-on-a-chip and 3D printing.* Biomaterials, 2018.

338. Bogorad, M.I., et al., *Review: in vitro microvessel models.* Lab Chip, 2015. **15**(22): p. 4242-55.

339. Traore, M.A. and S.C. George, *Tissue Engineering the Vascular Tree.* Tissue Eng Part B Rev, 2017. **23**(6): p. 505-514.

340. Bogorad, M.I., et al., *Tissue-engineered 3D microvessel and capillary network models for the study of vascular phenomena.* Microcirculation, 2017. **24**(5).

341. Faley, S.L., et al., *iPSC-Derived Brain Endothelium Exhibits Stable, Long-Term Barrier Function in Perfused Hydrogel Scaffolds.* Stem Cell Reports, 2019. **12**(3): p. 474-487.

342. Hughes, C.S., L.M. Postovit, and G.A. Lajoie, *Matrigel: a complex protein mixture required for optimal growth of cell culture.* Proteomics, 2010. **10**(9): p. 1886-90.

343. Pun, P.B., J. Lu, and S. Moochhala, *Involvement of ROS in BBB dysfunction.* Free Radic Res, 2009. **43**(4): p. 348-64.

344. Nguyen, D.H., et al., *Biomimetic model to reconstitute angiogenic sprouting morphogenesis in vitro.* Proc Natl Acad Sci U S A, 2013. **110**(17): p. 6712-7.

345. Pauty, J., et al., *A Vascular Endothelial Growth Factor-Dependent Sprouting Angiogenesis Assay Based on an In Vitro Human Blood Vessel Model for the Study of Anti-Angiogenic Drugs.* EBioMedicine, 2018. **27**: p. 225-236.

346. Rigau, V., et al., *Angiogenesis is associated with blood-brain barrier permeability in temporal lobe epilepsy.* Brain, 2007. **130**(Pt 7): p. 1942-56.

347. Bogorad, M.I., et al., *Cerebrovascular plasticity: Processes that lead to changes in the architecture of brain microvessels.* J Cereb Blood Flow Metab, 2019. **39**(8): p. 1413-1432.

348. Saunders, N.R., S.A. Liddelow, and K.M. Dziegielewska, *Barrier mechanisms in the developing brain.* Front Pharmacol, 2012. **3**: p. 46.

349. Vanlandewijck, M., et al., *A molecular atlas of cell types and zonation in the brain vasculature.* Nature, 2018. **554**(7693): p. 475-480.

350. Chen, H.H., C.H. Chien, and H.M. Liu, *Correlation between angiogenesis and basic fibroblast growth factor expression in experimental brain infarct.* Stroke, 1994. **25**(8): p. 1651-7.

351. Yukawa, H., et al., *Adenoviral gene transfer of basic fibroblast growth factor promotes angiogenesis in rat brain.* Gene Ther, 2000. **7**(11): p. 942-9.

352. Mongiat, M., et al., *Extracellular Matrix, a Hard Player in Angiogenesis.* Int J Mol Sci, 2016. **17**(11).

353. Rao, R.R., et al., *Matrix composition regulates three-dimensional network formation by endothelial cells and mesenchymal stem cells in collagen/fibrin materials.* Angiogenesis, 2012. **15**(2): p. 253-64.

354. Feng, X., et al., *Fibrin and collagen differentially but synergistically regulate sprout angiogenesis of human dermal microvascular endothelial cells in 3-dimensional matrix.* Int J Cell Biol, 2013. **2013**: p. 231279.

355. Edgar, L.T., et al., *Extracellular matrix density regulates the rate of neovessel growth and branching in sprouting angiogenesis.* PLoS One, 2014. **9**(1): p. e85178.

356. Wang, J. and R. Milner, *Fibronectin promotes brain capillary endothelial cell survival and proliferation through alpha5beta1 and alphavbeta3 integrins via MAP kinase signalling.* J Neurochem, 2006. **96**(1): p. 148-59.

357. Zimmermann, D.R. and M.T. Dours-Zimmermann, *Extracellular matrix of the central nervous system: from neglect to challenge.* Histochemistry and Cell Biology, 2008. **130**(4): p. 635-653.

358. Yamaguchi, Y., *Lecticans: organizers of the brain extracellular matrix.* Cellular and Molecular Life Sciences, 2000. **57**(2): p. 276-289.

359. Sykova, E. and C. Nicholson, *Diffusion in brain extracellular space.* Physiological Reviews, 2008. **88**(4): p. 1277-1340.

360. Placone, A.L., et al., *Human astrocytes develop physiological morphology and remain quiescent in a novel 3D matrix.* Biomaterials, 2015. **42**: p. 134-43.

361. Wevers, N.R., et al., *A perfused human blood-brain barrier on-a-chip for high-throughput assessment of barrier function and antibody transport.* Fluids Barriers CNS, 2018. **15**(1): p. 23.

362. Uwamori, H., et al., *Integration of neurogenesis and angiogenesis models for constructing a neurovascular tissue.* Sci Rep, 2017. **7**(1): p. 17349.

363. Kim, Y.W. and T.V. Byzova, *Oxidative stress in angiogenesis and vascular disease.* Blood, 2014. **123**(5): p. 625-31.

364. Stapor, P.C., et al., *Pericyte dynamics during angiogenesis: new insights from new identities.* J Vasc Res, 2014. **51**(3): p. 163-74.

365. Gerhardt, H., et al., *Neuropilin-1 is required for endothelial tip cell guidance in the developing central nervous system.* Dev Dyn, 2004. **231**(3): p. 503-9.

366. Canfield, S.G., et al., *An isogenic neurovascular unit model comprised of human induced pluripotent stem cell-derived brain microvascular endothelial cells, pericytes, astrocytes, and neurons.* Fluids Barriers CNS, 2019. **16**(1): p. 25.

367. Whisler, J.A., M.B. Chen, and R.D. Kamm, *Control of perfusable microvascular network morphology using a multiculture microfluidic system.* Tissue Eng Part C Methods, 2014. **20**(7): p. 543-52.

368. Bezenah, J.R., Y.P. Kong, and A.J. Putnam, *Evaluating the potential of endothelial cells derived from human induced pluripotent stem cells to form microvascular networks in 3D cultures.* Sci Rep, 2018. **8**(1): p. 2671.

Curriculum Vitae

Raleigh M. Linville (raleigh@jhu.edu)

EDUCATION

2016 – present   Johns Hopkins University, Baltimore, MD
                         Ph.D. Candidate, Biomedical Engineering
                         Advisor: Prof. Peter Searson
2012 – 2016   Boston University, Boston, MA
                         B.S., Biomedical Engineering, m*agna cum laude*

RESEARCH POSITIONS

2016 - present   Ph.D. Candidate
Searson Group, Johns Hopkins Institute for Nanobiotechnology
Advisor: Prof. Peter Searson (searson@jhu.edu)
Research: Developing *in vitro* 3D models of the blood-brain barrier (BBB) to: (1) mimic human brain vascular physiology, (2) develop novel drug delivery approaches, and (3) elucidate mechanisms of neurodegenerative disease and brain cancer.

2014 – 2016   Undergraduate Researcher
Tien Group, Boston University
Department of Biomedical Engineering
Advisor: Prof. Joe Tien (jtien@bu.edu)
Research: Studied biomaterial vascularization. Developed a novel method to rapidly generate capillaries for applications towards vascularized tissue constructs.

Spring 2014   Undergraduate Researcher
Lim Laboratory, Universidad Autónoma de Madrid
Advisor: Prof. Filip Lim (filip.lim@uam.es)
Research: Studied molecular mechanisms of neuronal lesion and repair using gene therapy. Increased viral titer in preparation for clinical trials of viral vectors to deliver whole genes for spinal cord regeneration.

2011 – 2014   Technical Aide
The Johns Hopkins University School of Medicine, Division of Neuropathology
Advisor: Dr. Leyan Xu (lxu9@jhmi.edu)
Research: Studied traumatic brain injury using a mouse model. Characterized neuropathology of blast-induced neurotrauma with and without protective gear.

PUBLICATIONS (* denotes equal contribution)

13. **Linville, R.M**., DeStefano, J.G., Nerenberg, R., Grifno, G.N., Ye, R., Gallagher, E., Searson, P.C., "Long-term cryopreservation preserves blood-brain barrier phenotype of iPSC-derived brain microvascular endothelial cells and three-dimensional microvessels." *Molecular Pharmaceuticals* (online ahead of print) (2020).

12. **Linville, R.M.**, Arevalo, D., Maressa, J.C., Zhao, N., Searson, P.C., "Three-dimensional induced pluripotent stem-cell models of human brain angiogenesis." *Microvascular Research* (online ahead of print) (2020).

11. Silvestri, V.L., Henriet, E., **Linville, R.M.**, Wong, A.D., Searson, P.C., Ewald, A.J., "A tissue-engineered 3D microvessel model reveals the dynamics of mosaic vessel formation in breast cancer." *Cancer Research* (online ahead of print) (2020).

10. Chu, C., Jablonska, A., Lesniaka, W.G., Thomas, A.M., Lan, X., **Linville, R.M.**, Li, S., Searson, P.C., Liu, G., Pearl, M., Pomper, M.G., Janowski, M., Magnus, T., Walczak, P., "Optimization of osmotic blood-brain barrier opening to enable intravital microscopy studies on drug delivery in mouse cortex." *Journal of Controlled Release* 317, 312-321 (2020).

9. Grifno, G.*, Farrell, A.*, **Linville, R.M.***, Arevalo, D., Kim, J.H., Gu, L., Searson, P.C., "Three-dimensional in vitro blood-brain barrier microvessels via directed differentiation of fluorescently-tagged induced pluripotent stem cells." *Scientific Reports* 9 (1), 1-13 (2019).

8. Jamieson, J.J., **Linville, R.M.**, Yuan, Y., Searson, P.C., Gerecht S., "Role of iPSC-derived pericytes on barrier function of iPSC-derived brain microvascular endothelial cells in 2D and 3D." *Fluids and Barriers of the CNS* 16, 15 (2019).

7. **Linville, R.M.**, DeStefano J.G., Sklar, M.B., Chu, C., Walczak, P., Searson, P.C., "Modeling hyperosmotic blood-brain barrier opening within human tissue-engineered in vitro brain microvessels." *Journal of Cerebral Blood Flow & Metabolism* 40 (7), 1517-1532 (2019).

6. **Linville, R.M.**, DeStefano J.G., Sklar, M.B., Xu, Z., Farrell, A.M., Bogorad, M.I., Chu, C., Walczak, P., Cheng, L., Mahairaki, V., Whartenby, K.A., Calabresi, P.A., Searson, P.C., "Human iPSC-derived blood-brain barrier microvessels: validation of barrier function and endothelial cell behavior." *Biomaterials* 190, 24-37 (2019).

5. Bogorad, M.I.*, DeStefano J.*, **Linville, R.M.***, Wong, A.*, Searson, P.C., "Cerebrovascular plasticity: processes that lead to changes in the cerebrovascular architecture." *Journal of Cerebral Blood Flow & Metabolism* 39 (8), 1413-1432 (2019).

4. Katt, M., **Linville, R.M.**, Mayo, L.N., Xu, Z., Searson, P.C., "Functional brain-specific microvessels from iPSC-derived human brain microvascular endothelial cells: the role of matrix composition on monolayer formation." *Fluids and Barriers of the CNS* 15, 7 (2018).

3. DeStefano J.*, Jamieson, J.J.*, **Linville, R.M.***, Searson, P.C., "Benchmarking in vitro tissue-engineered blood–brain barrier models." *Fluids and Barriers of the CNS* 15, 32 (2018).

2. Xu, L., Schaefer M.L., **Linville, R.M.**, Aggarwal A., Mbuguiro W., Wester B.A., Koliatsos V.E., Neuroinflammation in primary blast neurotrauma: time course and prevention by torso shielding." *Experimental Neurology* 277, 268-274 (2016).

1. **Linville, R.M.**, Boland, N.F., Covarrubias, G., Price, G.M., Tien, J., "Physical and chemical signals that promote vascularization of capillary-scale channels." *Cellular and Molecular Bioengineering* 9, 73-84 (2016).

PRESENTATIONS

1. Linville, R.M., Boland, N.F., Covarrubias, G. & Tien, J., "Vascularization of capillary-scale channels in type I collagen gels" [talk], 41st Annual Northeast Bioengineering Conference (Troy, NY; 2015).

2. Linville, R.M., Boland, N.F., Covarrubias, G. & Tien, J., "Generation of capillaries in patterned type I collagen gels in vitro" [poster], Biomedical Engineering Society 2015 Annual Meeting (Tampa, FL; 2015).

3. Linville, R.M., Katt, M., Searson, P.C., "Tissue-engineering of iPSC-derived brain-specific microvessels" [poster], Biomedical Engineering Society 2017 Annual Meeting (Phoenix, AZ;

2017).

4. Linville, R.M., DeStefano J., Sklar, M., Farrell, A., Chu, C., Walczak, P., Searson, P.C., "Human iPSC-derived three dimensional microvessels for study of hyperosmolar blood-brain barrier opening" [poster], Johns Hopkins Department of Medicine Research Retreat (Baltimore, MD; 2018).

5. Linville, R.M., DeStefano, J., Chu, C., Walczak, P., Searson, P.C., "Human iPSC-derived three-dimensional microvessels for study of hyperosmolar blood-brain barrier opening" [poster], Barriers of the CNS Gordon Research Conference (New London, NH; 2018).

6. Linville, R.M., DeStefano, J., Komin, A., Chu, C., Hristova, K., Walczak, P., Searson, P.C., "Modeling hyperosmotic and peptide-induced blood-brain barrier opening within tissue-engineered in vitro human brain microvessels" [talk], 2nd meeting of the Society for Image Guided Neurointerventions (SIGN) (Baltimore, MD; 2019).

7. Linville, R.M., DeStefano, J., Komin, A., Chu, C., Hristova, K., Walczak, P., Searson, P.C., "Three-dimensional tissue-engineered iPSC-derived blood-brain barrier microvessels for studies of blood-brain barrier opening" [poster], Cerebral Vascular Biology Conference (Miami, FL; 2019).

8. Linville, R.M., Nerenberg, R.F., Grifno, G.N., Searson, P.C., "CAG-induced blood-brain barrier dysfunction in an isogenic iPSC model of juvenile-onset Huntington's disease" [poster], International Ataxia Research Conference (Washington, DC; 2019).

9. Linville, R.M., "Tissue-engineered models of blood-brain barrier tight junctions during health and disease" [talk], Columbia University's Trainee Symposium on Organoids & Organs-on-a-Chip (virtual; 2020).

GRADUATE LEADERSHIP AND ACTIVITIES

Activity	Years	Description
STEM Achievement in Baltimore Elementary Schools (SABES), Team Leader	2016 – 2021	Team Leader for SABES after-school STEM education program for three consecutive years, 75+ volunteer hours
Pathways in Technology Early College High School (P-TECH), Mentor	2016 – 2019	Mentor for P-TECH program providing career and life mentorship to Baltimore high school students pursuing careers in medicine
Searson Group, Lab Captain	2019 – 2021	Manage daily lab operations; promote strong communication and community among lab members; organized virtual journal club series during COVID19 pandemic
Manuscript reviewer	2020 – present	Independent reviewer for journal *Biomaterials, Acta Biomaterialia*
Summer Undergraduate Virtual Research Experience (SURVE), Organizer and Presenter	2020 – present	Founding organizer and presenter for SURVE program, a weekly engagement series for Hopkins undergraduate researchers during COVID19 pandemic sponsored by Hopkins Office for Undergraduate Research.

GRADUATE HONORS
• National Science Foundation Graduate Fellow (2018-2021)
• Johns Hopkins Department of Medicine Research Retreat – Whiting School of Engineering Basic Research Trainee Award finalist (2018)
• Society for Image Guided Neurointerventions (SIGN) – Third place Early Stage Investigator Award (2019)

TEACHING EXPERIENCE

Role	Semesters	Class and Instructors
Instructor	Intersession 2019, Intersession 2020, Intersession 2021	EN.580.137 (1 credit), Tissue Engineering Blood Vessels
Co-Instructor *(five-course module)*	Spring 2019, Spring 2020	EN.510.610 (3 credits), Fundamentals of Biomaterials (instructor: Prof. Peter Searson)
Teaching Assistant	Fall 2018	EN.580.442/642, Tissue Engineering (3 credits) (instructors: Prof. Warren Grayson and Prof. Jennifer Elisseeff)
Lab Instructor *(one-week module)*	Spring 2019	EN.510.430, Biomaterials Lab (instructor: Prof. Kalina Hristova)
Certificate of Completion	March 2020	Johns Hopkins University Teaching Academy